

Uniform Forward-Modeling Analysis of Ultracool Dwarfs. II. Atmospheric Properties of 55 Late-T Dwarfs

ZHOUIAN ZHANG (张周健),^{1,2} MICHAEL C. LIU,¹ MARK S. MARLEY,^{3,4} MICHAEL R. LINE,⁵ AND WILLIAM M. J. BEST⁶

¹*Institute for Astronomy, University of Hawaii at Manoa, Honolulu, HI 96822, USA*

²*Visiting Astronomer at the Infrared Telescope Facility, which is operated by the University of Hawaii under contract 80HQTR19D0030 with the National Aeronautics and Space Administration.*

³*NASA Ames Research Center, Mail Stop 245-3, Moffett Field, CA 94035, USA*

⁴*The University of Arizona, Tucson AZ 85721, USA*

⁵*School of Earth & Space Exploration, Arizona State University, Tempe AZ 85287, USA*

⁶*Department of Astronomy, University of Texas at Austin, Austin, Texas 78712, USA*

(Received August 8, 2020; Revised April 29, 2021; Accepted May 5, 2021)

Submitted to ApJ

ABSTRACT

We present a large uniform forward-modeling analysis for 55 late-T (T7–T9) dwarfs, using low-resolution ($R \approx 50 - 250$) near-infrared ($1.0 - 2.5 \mu\text{m}$) spectra and cloudless Sonora-Bobcat model atmospheres. We derive the objects’ effective temperatures, surface gravities, metallicities, radii, masses, and bolometric luminosities using our newly developed Bayesian framework, and use the resulting population properties to test the model atmospheres. We find (1) our objects’ fitted metallicities are $0.3 - 0.4$ dex lower than those of nearby stars; (2) their ages derived from spectroscopic parameters are implausibly young ($10 \text{ Myr} - 0.4 \text{ Gyr}$); (3) their fitted effective temperatures show a similar spread as empirical temperature scales at a given spectral type but are $\sim 50 - 200 \text{ K}$ hotter for $\geq T8$ dwarfs; and (4) their spectroscopically inferred masses are unphysically small (mostly $1 - 8 M_{\text{Jup}}$). These suggest the Sonora-Bobcat assumptions of cloudless and chemical-equilibrium atmospheres do not adequately reproduce late-T dwarf spectra. We also find a gravity- and a metallicity-dependence of effective temperatures as a function of spectral type. Combining the resulting parameter posteriors of our sample, we quantify the degeneracy between fitted surface gravity and metallicity such that an increase in Z combined with a $3.4\times$ increase in $\log g$ results in a spectrum that has similar fitted parameters. We note the systematic difference between late-T dwarf spectra and Sonora-Bobcat models is on average $\approx 2\% - 4\%$ of the objects’ peak J -band fluxes over the $1.0 - 2.5 \mu\text{m}$ range, implying modeling systematics will exceed measurement uncertainties when analyzing data with J -band $\text{S/N} \gtrsim 50$. Using our large, high-quality sample, we examine the spectral-fitting residuals as a function of wavelength and atmospheric properties to discern how to improve the model assumptions. Our work constitutes the largest analysis of brown dwarf spectra using multi-metallicity models and the most systematic examination of ultracool model atmospheres to date.

1. INTRODUCTION

Characterization of ultracool dwarf spectra is essential to understand the physical and chemical processes in the atmospheres of brown dwarfs and exoplanets. Such processes govern these objects’ appearance and evolution, and the emergent spectra encode signatures of their formation pathways (e.g., Burrows et al. 2001; Fortney et al. 2008; Marley & Robinson 2015). However, spectroscopic analysis of sub-stellar objects can be challenging given the numerous complex processes and interactions in ultracool atmospheres.

As brown dwarfs evolve to cooler effective temperatures, substantial changes in atmospheric chemistry drive the emergence and disappearance of various atomic and molecular spectral features. The transition from M to L spectral type is marked by the increasing strengths of alkali lines (e.g., Na and K) and metal hydride bands (e.g., FeH and CrH), and the disappearance of TiO and VO due to the formation of titanium-bearing condensates (e.g., CaTiO_3 ; Burrows & Sharp 1999; Lodders 2002). During the M/L transition, clouds of iron and silicate grains (e.g., MgSiO_3 and Mg_2SiO_4) form and cause the objects’ emergent spectra to

become redder toward later L subtypes (Burrows & Sharp 1999; Marley et al. 2002). The hallmark of the transition from L to T spectral type is the emergence of CH₄ absorption, along with the strengthening of H₂O bands. The cool temperatures of the L/T transition ($T_{\text{eff}} \approx 1200 - 1400$ K) apparently lead to cloud patchiness, condensation below the photosphere, and dissipation (e.g., Saumon & Marley 2008; Marley et al. 2010), resulting in brighter *J*-band emission and bluer *J* – *K* colors of early-T dwarfs as compared to late-L dwarfs (e.g., Knapp et al. 2004; Liu et al. 2006; Dupuy & Liu 2012). The transition from T to Y spectral type is defined by the emergence of NH₃ absorption in the near-infrared, along with the formation of new condensates (e.g., Na₂S, KCl, and H₂O) given the cold atmosphere temperature ($\lesssim 600$ K; Cushing et al. 2011; Morley et al. 2012). An alternative interpretation of the L-T-Y evolution does not rely on clouds but rather a thermo-chemical instability (e.g., Tremblin et al. 2015, 2016, 2017, 2019). Such an instability can trigger local compositional convection, drive chemical abundances (e.g., CO/CH₄ and N₂/NH₃) out of equilibrium, and reduce the vertical temperature gradient in the atmospheres.

Efforts have been devoted to describe the above complicated processes via models of ultracool atmospheres (e.g., Baraffe et al. 1998, 2003a; Chabrier et al. 2000; Burrows et al. 2002; Marley et al. 2002, 2010, 2017; Burrows et al. 2006; Saumon & Marley 2008; Allard et al. 2012; Morley et al. 2012; Tremblin et al. 2015, 2016; Mollière et al. 2019; Phillips et al. 2020). Characterization of brown dwarfs is commonly conducted by comparing grids of such pre-computed, forward models to observations. Synthetic model spectra have been quite successful in predicting the spectral morphology of brown dwarfs and giant planets, but inconsistencies between data and grid models have been long noticed (e.g., Cushing et al. 2008; Stephens et al. 2009; Leggett et al. 2017; Zhang et al. 2020a), indicating that the assumptions of these models (e.g., cloud properties, equilibrium chemistry, and radiative convective equilibrium) should be improved. Recently, we have conducted a forward-modeling analysis using cloudless Sonora-Bobcat models (Marley et al. 2017; Marley et al. submitted) for three benchmark late-T dwarfs, HD 3651B, GJ 570D, and Ross 458C (Zhang et al. 2020b; referred to as “Paper I” hereinafter). Comparing our spectral-fitting results to those derived from these objects’ bolometric luminosities, their primary stars’ ages and metallicities, and the Sonora-Bobcat evolutionary models, we identified potential shortcomings of model predictions of these three objects. However, such analysis is hampered by the small census of known benchmarks with high-quality spectroscopy, meaning an insufficient diversity in surface gravity and metallicity at a given effective temperature (especially for $\lesssim 1000$ K).

The atmospheric retrieval technique is an alternative approach for inferring brown dwarf properties, which is not

limited to the physical assumptions made by grid models and has the freedom to explore more physical (and unphysical) conditions of ultracool atmospheres by using many more free parameters (e.g., Line et al. 2015, 2017; Burningham et al. 2017; Zalesky et al. 2019; Gonzales et al. 2020). Aiming to find models that almost exactly explain the observed spectra, retrieval can robustly test whether the physical assumptions made within grid models are reasonable. However, when an object has a peculiar spectrum, this data-driven method might converge to atmospheric compositions and thermal structures that are not physically self-consistent (e.g., Zalesky et al. 2019).

Studying large samples of brown dwarfs can help surpass the aforementioned limitations of both forward modeling and retrieval methods, so that fundamental properties of the ultracool population can be robustly investigated. In addition, forward-modeling analysis of an ensemble of brown dwarfs can uncover the discrepancies between data and models, providing feedback about the strength and weakness of current modeling. Thanks to the wide coverage and depth of imaging sky surveys, including Pan-STARRS1 (PS1; Chambers et al. 2016), 2MASS (Skrutskie et al. 2006), the UKIRT Infrared Deep Sky Survey (UKIDSS; Lawrence et al. 2007), and the Wide-field Infrared Survey Explorer (WISE, Wright et al. 2010; CatWISE, Eisenhardt et al. 2020; Marocco et al. 2020), we now have a large census of brown dwarfs in the field and in young associations (e.g., Kirkpatrick et al. 1999, 2011; Luhman 2006; Luhman et al. 2009; Luhman & Mamajek 2012; Burningham et al. 2008, 2010a, 2013; Best et al. 2015, 2017, 2018; Best et al. 2020b; Lodieu et al. 2007; Lodieu 2013; Gagné et al. 2018; Zhang et al. 2018a; Meisner et al. 2020). Most notably, the sample of ultracool dwarfs with near-infrared spectra is abundant (≥ 20 objects in each spectral subtype from M6 to T8; e.g., Burgasser 2014; Filippazzo et al. 2016; Manjavacas et al. 2019), enabling ensemble analyses instead of the more common single-object studies.

In this paper, we apply our forward-modeling framework constructed and validated in Paper I to 55 T7–T9 dwarfs ($T_{\text{eff}} \approx 600 - 1200$ K). Late-T dwarfs likely lack optically thick clouds in their near-infrared photospheres (though optically thin, sulfide clouds might exist; e.g., Morley et al. 2012). Therefore, choosing late-T dwarfs helps simplify the model parameter space and can validate the cloud-free models, which serve as the starting point for the more complex cloudy models. We compare our objects’ low-resolution near-infrared spectra to cloudless Sonora-Bobcat models with both solar and non-solar metallicities. Our forward-modeling analysis uses the Bayesian framework Starfish (developed by Czekala et al. 2015 and updated by Gully-Santiago et al. 2017; see Paper I), which accounts for uncertainties from model interpolation, as well as correlated

(data–model) residuals due to instrumental effects and modeling systematics, thereby providing robust physical parameters and more realistic error estimates than the traditional (χ^2 -based) methods adopted in most previous work. Our work is the largest analysis of brown dwarf spectra using multi-metallicity models and altogether the most systematic test of any set of ultracool model atmospheres to date.

We aim to investigate the physical properties of late-T dwarfs and examine the model atmospheres through detailed comparisons between data and models. We start with a description of our sample (Section 2) and present our methodology and results of the forward-modeling analysis (Section 3). We identify known and candidate binaries in our sample and exclude them from our subsequent analysis (Section 4). We then study the inferred atmospheric properties of late-T dwarfs (Section 5) and use them to investigate the performance of the cloudless Sonora-Bobcat models (Section 6). Finally, we provide a summary and a brief discussion of further work (Section 7).

2. OBSERVATIONS

2.1. Sample of T7–T9 Dwarfs

We construct our sample of late-T dwarfs by using the catalog of ultracool dwarfs by Best et al. (2018) and selecting all T7–T9 objects with prism-mode ($R \approx 50 - 250$) spectra taken from the SpeX spectrograph (Rayner et al. 2003) mounted on the NASA Infrared Telescope Facility (IRTF). These low-resolution spectra are from our own observations (Section 2.2), the SpeX Prism Library (Burgasser 2014; Burgasser & Splat Development Team 2017), and the literature (e.g., Burgasser et al. 2004, 2006a, 2010a; Best et al. 2015), leading to a total of 55 late-T dwarfs. In this sample, 54 objects have parallaxes (van Leeuwen 2007; Burgasser et al. 2008b; Dupuy & Liu 2012; Leggett et al. 2012; Gaia Collaboration et al. 2016a,b, 2018; Kirkpatrick et al. 2019; Best et al. 2020a) and the only remaining object, WISE J024512.62–345047.8 (WISE 0245–3450, T8; Mace et al. 2013a), is part of our astrometric monitoring program. Four objects in our sample are co-moving companions to either stars or brown dwarfs: HD 3651B (T7.5; Mugrauer et al. 2006; Luhman et al. 2007), GJ 570D (T7.5; Burgasser et al. 2000), Ross 458C (T8; Goldman et al. 2010; Scholz 2010b), and ULAS J141623.94+134836.3 (ULAS 1416+1348; T7.5 Scholz 2010a; Burningham et al. 2010b), for which we adopt the parallaxes of their primary hosts from Gaia DR2 (Gaia Collaboration et al. 2016a, 2018). The first three benchmark objects have been analyzed in Paper I and here we simply keep them in our sample. Our sample contains 90% of the known T7–T9 dwarfs that have distances ≤ 25 pc, J -band magnitudes ≤ 17.5 mag, and declinations from -40°

to $+70^\circ$ ¹. Information about our sample’s spectroscopy, astrometry, and photometry is listed in Tables 1, 2, and 3, respectively.

2.2. IRTF/SpeX Spectroscopy

We obtained near-infrared spectra of 16 T7–T9 dwarfs in our sample using IRTF (Table 1). We used SpeX in prism mode with either the $0.5''$ slit ($R \approx 80 - 250$) or the $0.8''$ slit ($R \approx 50 - 160$). For each target, we took at least six exposures in a standard ABBA pattern and contemporaneously observed a nearby A0V standard star within 0.1 airmass for telluric correction. We reduced the data using version 4.1 of the Spextool software package (Cushing et al. 2004). Our resulting spectra are reported with vacuum wavelengths and have typical S/N ≈ 50 per pixel in J band.

Combining all available IRTF/SpeX spectra, we find 42 objects in our sample have spectra observed using the $0.5''$ slit and 15 objects using the $0.8''$ slit, with 2 objects having spectra observed using both slit widths. Therefore, we have in total 57 near-infrared spectra for 55 objects. We flux-calibrate all spectra using the objects’ H_{MKO} magnitudes, which are either observed (e.g., Knapp et al. 2004; Lawrence et al. 2012; Kirkpatrick et al. 2019) or synthesized from other bands by Best et al. (2021). The WFCAM H -band filter and the corresponding zero-point flux are from Hewett et al. (2006) and Lawrence et al. (2007), respectively.

3. FORWARD-MODELING ANALYSIS

3.1. Methodology

In Paper I, we constructed and validated a forward-modeling framework using the Bayesian inference tool Starfish (Czekala et al. 2015; Gully-Santiago et al. 2017) and the Sonora-Bobcat models (Marley et al. 2017; Marley et al. submitted), which assume cloudless and chemical-equilibrium atmospheres. Our framework is customized for the parameter space relevant to late-T dwarfs: [600, 1200] K in effective temperature T_{eff} , [3.25, 5.5] dex in logarithmic surface gravity $\log g$, and $[-0.5, +0.5]$ dex in bulk metallicity Z (before removal of any species by condensation), and for near-infrared ($0.8 - 2.5 \mu\text{m}$) spectra taken using the prism mode of IRTF/SpeX. Here we summarize our methods and refer readers to Paper I and Czekala et al. (2015) for more details.

We start our analysis by training Starfish’s spectral emulator to generate a probability distribution of model spectra for an arbitrary set of grid parameters. Starfish propagates the

¹ The five late-T dwarfs with such properties not included in our sample are: Gl 229B (T7; Nakajima et al. 1995), WISEPA J052844.51–330823.9 (T7; Kirkpatrick et al. 2011), WISE J214706.78–102924.0 (T7.5; Mace et al. 2013a), WISEPA J085716.25+560407.6 (T8; Kirkpatrick et al. 2011), and WISEPA J143602.19–181421.8 (T8; Kirkpatrick et al. 2011).

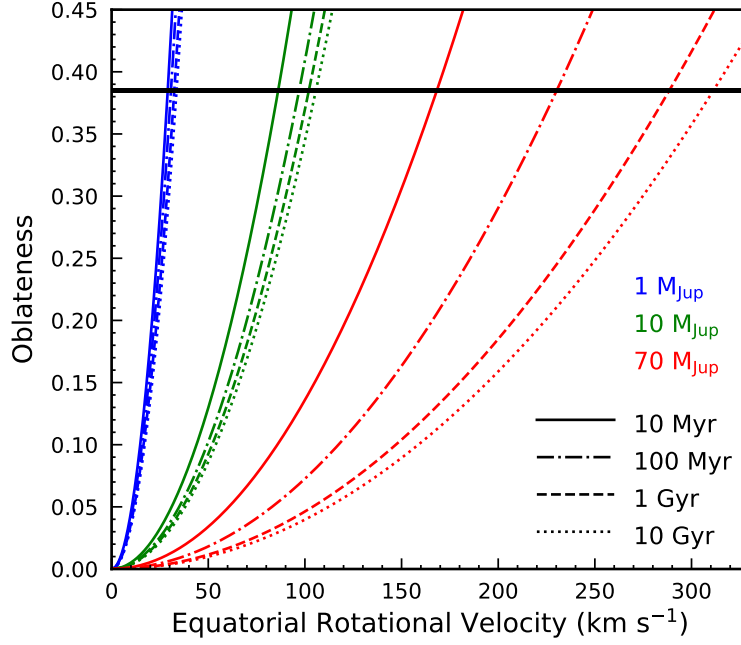


Figure 1. Rotation-induced oblateness as a function of equatorial rotational velocity v_{rot} with different ages and masses, based on the solar-metallicity cloudless Sonora-Bobcat evolutionary models. We compute oblateness as $f = 2Cv_{\text{rot}}^2/3gR$ (e.g., Barnes & Fortney 2003), where $\{g, R\}$ are derived from the evolutionary models and $C = 0.9669$ corresponds to the $n = 1.5$ polytrope representative of fully convective brown dwarfs (e.g., Burrows & Liebert 1993). We use the black horizontal line to mark the critical oblateness ($f_{\text{crit}} = 0.385$) below which objects are rotationally stable and have $v_{\text{rot}} \leq 300 \text{ km s}^{-1}$. These theoretical relations are only slightly changed using the Sonora-Bobcat models with non-solar metallicities (i.e., $Z = -0.5$ and $+0.5$). A 10 Gyr-old $70 M_{\text{Jup}}$ object can induce the same oblateness if it has a 0.5 dex lower metallicity but $\approx 20 \text{ km s}^{-1}$ higher v_{rot} . Such an effect due to non-solar metallicity diminishes with younger ages and lower masses.

resulting interpolation uncertainties into the inferred posteriors and is thereby fundamentally different from linear interpolation adopted by traditional (χ^2 -based) forward-modeling analyses (e.g., Rice et al. 2010; Zhang et al. 2020a). We first trim the cloudless Sonora-Bobcat models over the aforementioned grid parameter space and wavelength range, and then downgrade their spectral resolution using two different Gaussian kernels, which correspond to the $0.5''$ slit and the $0.8''$ slit of SpeX. The convolution also accounts for the wavelength-dependent spectral resolution of the SpeX prism mode (Rayner et al. 2003). We conduct principal component analysis and train Gaussian processes on these processed models, leading to spectral emulators tailored for spectra obtained with the $0.5''$ and $0.8''$ slits.

We determine six physical parameters: effective temperature T_{eff} , logarithmic surface gravity $\log g$, metallicity Z , radial velocity v_r , projected rotational velocity $v \sin i$, and logarithmic solid angle $\log \Omega = \log (R/d)^2$, where i , R , and d is the inclination of the rotation axis, the radius, and the distance, respectively. As in Paper I, we assume uniform priors of $[600, 1200] \text{ K}$ in T_{eff} , $[3.25, 5.5]$ dex in $\log g$, $[-0.5, +0.5]$ dex in Z , $(-\infty, +\infty)$ for both v_r and $\log \Omega$, and $[0, v_{\text{max}}]$ for $v \sin i$. We determine v_{max} using the objects' distances and fitted $\{\log g, \log \Omega\}$ in each step of the spectral-

fitting process by assuming the rotationally induced oblateness is within the stability limit. For the only object in our sample (WISE 0245 – 3450) without a parallax, we use the theoretical relation between the oblateness and the equatorial rotational velocity based on the cloudless Sonora-Bobcat models (see Figure 1) and adopt $v_{\text{max}} = 300 \text{ km s}^{-1}$.

We also determine three hyper-parameters $\{a_N, a_G, \ell\}$ as part of our spectral-fitting process. These characterize the final covariance matrix which contains both diagonal and off-diagonal components. The latter accounts for correlated data–model residuals due to instrumental effects and modeling systematics, leading to more realistic error estimates than a covariance matrix with only diagonal components. We adopt the same hyper-parameter priors as in Paper I, but we assume a uniform prior of $[425, 1115 \times 5] \text{ km s}^{-1}$ in ℓ for the $0.8''$ spectra in our sample. This is slightly different from the $[820, 1840 \times 5] \text{ km s}^{-1}$ we use for $0.5''$ spectra, given the different instrumental line spread functions for these two slit widths (see Appendix of Paper I).

We use *emcee* (Foreman-Mackey et al. 2013) to fit our objects' $1.0 - 2.5 \mu\text{m}$ spectra with 48 walkers. We terminate the MCMC fitting process after 10^5 iterations, since such number of iterations exceeds 50 times the autocorrelation length of all the fitted parameters. To complete our forward-modeling

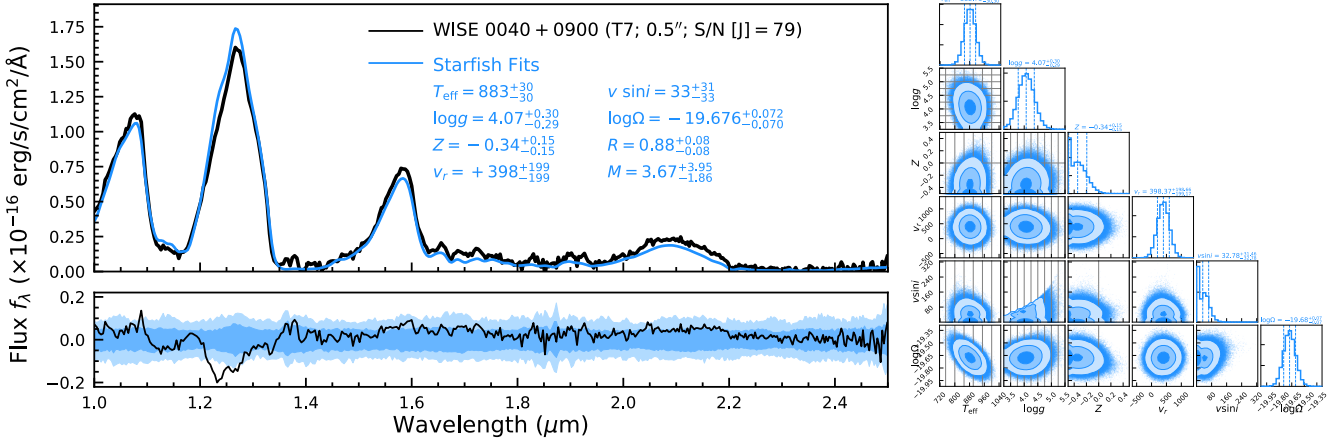


Figure 2. Starfish-based forward-modeling results of our late-T dwarf sample. Left: The upper panel shows the observed spectrum (black) of each object and the median Sonora-Bobcat model spectra of those interpolated at parameters drawn from the MCMC chains (blue). The object’s name, spectral type, the slit width and J -band S/N (median S/N in 1.2 – 1.3 μ m) of its spectrum, and inferred physical parameters are in the upper right corner. The lower panel shows the residual (data–model; black), with the blue shadows being 1 σ and 2 σ dispersions of 5×10^4 draws from the Starfish’s full covariance matrix. Right: Posteriors of the six physical parameters $\{T_{\text{eff}}, \log g, Z, v_r, v \sin i, \log \Omega\}$ derived from the Starfish-based forward-modeling analysis. We use grey vertical and horizontal lines to mark the $\{T_{\text{eff}}, \log g, Z\}$ grids points of the cloudless Sonora-Bobcat models. Figures of spectral-fitting results for our entire sample (55 late-T dwarfs with 57 spectra) are accessible online.

analysis, we add the following systematic uncertainties into the resulting parameter posteriors: 20 K in T_{eff} , 0.2 dex in $\log g$, 0.12 dex in Z , 180 km s^{−1} in v_r , 40 km s^{−1} in $v \sin i$, and $[0.05^2 + (0.4\sigma_{H_{\text{MKO}}})^2]^{1/2}$ dex in $\log \Omega$, where $\sigma_{H_{\text{MKO}}}$ is the H -band magnitude uncertainty. These systematic errors were determined in Paper I by (1) fitting the original Sonora-Bobcat model atmospheres themselves using our forward-modeling framework to quantify the uncertainties introduced by Starfish’s spectral emulator, (2) incorporating the uncertainty in the wavelength calibration of the SpeX prism data into the systematics of v_r , and (3) incorporating the uncertainty in the flux calibration of spectra (due to H -band magnitude errors) into the systematics of $\log \Omega$. We note all these added uncertainties are smaller than or comparable to the formal fitting errors of physical parameters (see Table 6).

In addition, we flux-calibrate the objects’ spectra using H -band magnitudes in this work, and conducting this process using photometry in different bands will alter our resulting $\log \Omega$ posteriors (e.g., Figure 8 of Line et al. 2015). Each late-T dwarf in our sample has similar photometric uncertainties among J , H , and K bands. Therefore, the objects’ $\log \Omega$ posteriors, derived using spectra calibrated by J_{MKO} or K_{MKO} , will have different median values but similar uncertainties compared to those inferred in this work using H_{MKO} . As a reference, Table 4 lists the shifts ($\Delta \log \Omega$) that our fitted $\log \Omega$ values would be changed by if our objects’ spectra were instead flux-calibrated using J or K band. Our derived spectroscopic radii, masses, and bolometric luminosities (see Section 3.2) would be accordingly increased by $0.5\Delta \log \Omega$, $\Delta \log \Omega$, and $\Delta \log \Omega$ in the logarithmic scale, respectively.

We do not incorporate these small shifts (which are mostly smaller than the uncertainties from the spectral fitting) into the systematic errors, so our spectroscopically inferred properties are all tied to the objects’ H -band photometry.

3.2. Results

Figure 2 presents the resulting parameter posteriors of our late-T dwarfs and compares the observed data with Sonora-Bobcat model spectra interpolated at the physical parameters drawn from the MCMC samples. These observed data and fitted model spectra of our entire sample are summarized in Figure 3. We list the fitted physical parameters and uncertainties in Table 4.² We further use the objects’ parallaxes and their fitted $\log g$ and $\log \Omega$ to derive their radii (R) and masses (M). We also compute the bolometric luminosity (L_{bol}) of each object by integrating its observed 1.0 – 2.5 μ m SpeX spectrum combined with the fitted model spectra at shorter and longer wavelengths spanning 0.4 – 50 μ m. We have incorporated uncertainties in observed spectral fluxes, parallaxes, and fitted physical parameters into our resulting L_{bol} values in a Monte Carlo fashion. Such computed L_{bol} ’s are not necessarily equal to those derived from the objects’ T_{eff} and R posteriors via the Stefan-Boltzmann law, given the mismatch between observed spectra and fitted models in

² The spectroscopically inferred radial velocities and projected rotational velocities in our analysis cannot be well constrained due to the low spectral resolution of the data. These physical parameters (v_r and $v \sin i$) are in fact coupled with the model systematics but have no correlations with, and thereby no impact on, the other physical parameters (Figure 5; also see Section 4.2 of Paper I).

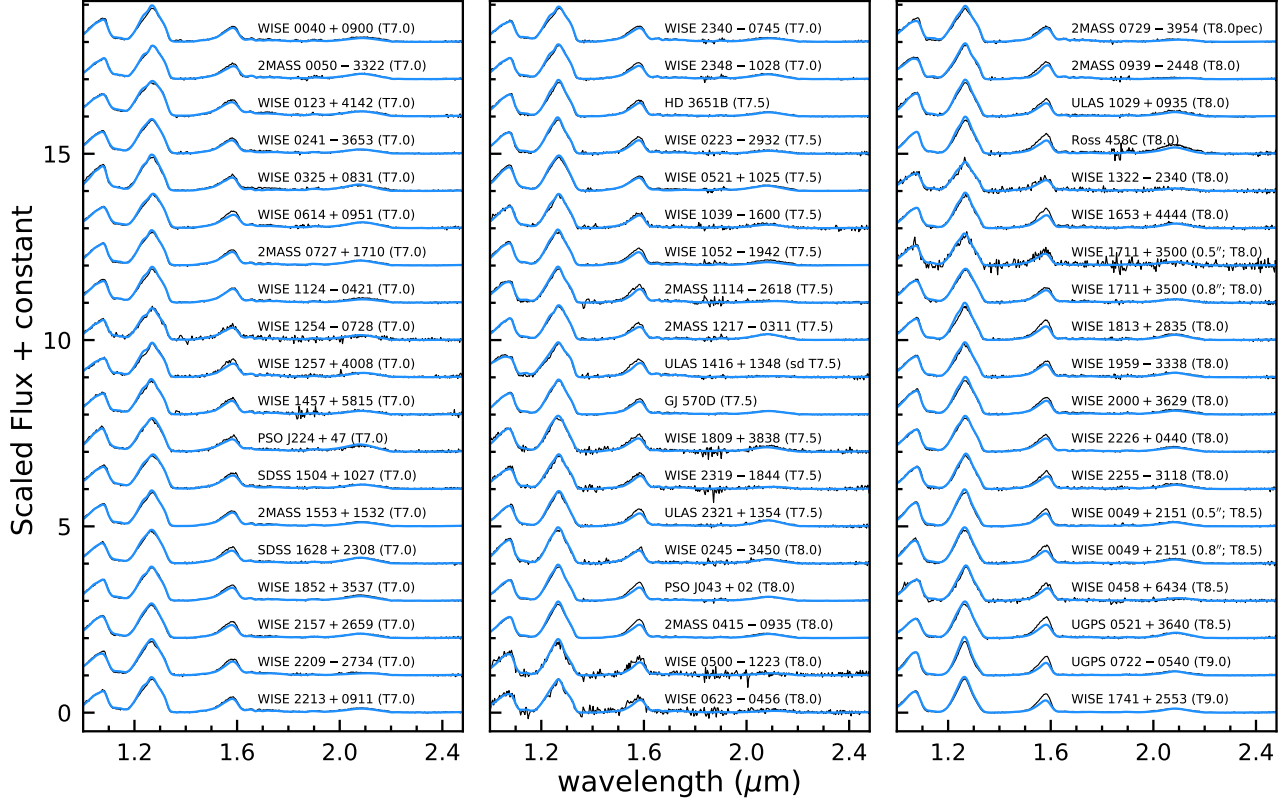


Figure 3. Observed spectra (black) of our entire late-T dwarf sample and the median Sonora-Bobcat model spectra interpolated at parameters drawn from the MCMC chains (blue).

1.0 – 2.5 μm wavelengths. We confirm our objects’ bolometric luminosities computed from these two approaches are all consistent within uncertainties. For HD 3651B, GJ 570D, and Ross 458C, we adopt the more accurate L_{bol} derived in our Paper I using their primary stars’ ages and metallicities and the Sonora-Bobcat evolutionary models. We compare our computed L_{bol} with literature in Appendix A and calculate bolometric corrections for T7–T9 dwarfs in Appendix B. The derived physical properties (R , M , L_{bol}) of our objects are summarized in Table 5.

We summarize the typical parameter uncertainties in Table 6 and find the resulting $\{T_{\text{eff}}, \log g, Z\}$ uncertainties of our sample are about $1/3 - 1/2$ of the Sonora-Bobcat model grid spacing, the same as our finding in Paper I for the three late-T benchmarks, HD 3651B, GJ 570D, and Ross 458C. The fitted models generally match well the observed spectra, and we discuss the data-model comparison in Section 6.

Some of our spectroscopically inferred physical parameters of late-T dwarfs can be under- or over-estimated relative to their true values, given that our set of models assume cloudless and chemical-equilibrium atmospheres. In Paper I, we analyzed three late-T benchmarks and compared the fitted parameters to those derived from their bolometric luminosities, their primary stars’ metallicities and ages,

and the Sonora-Bobcat evolutionary models. Assuming the evolutionary-based parameters are more robust, we found the accuracy of our forward-modeling results exhibited two outcomes. For HD 3651B and GJ 570D, our spectral fits produced reliable T_{eff} and R , but underestimated $\log g$ and Z by $\approx 1.1 - 1.3$ dex and $\approx 0.3 - 0.4$ dex, respectively. For Ross 458C, our spectral fit produced reliable $\log g$ and Z , but overestimated T_{eff} by ≈ 120 K and underestimated R by $\approx 0.4 R_{\text{Jup}}$ (or a factor of ≈ 1.6). Underestimation of the spectroscopically inferred $\log g$ and/or R further led to unphysically small masses of these objects. The late-T dwarfs in our sample might have their fitted parameters biased by similar amount as these benchmarks, and in Sections 5 and 6, we demonstrate that the spectroscopically inferred parameters of this ensemble of late-T dwarfs are useful to assess the model atmospheres.

We also conducted a forward-modeling analysis following the traditional approach, where we use linear interpolation to generate the model spectrum in between grid points and adopt a diagonal covariance matrix (defined by observed flux uncertainties) to evaluate free parameters. We describe details in Appendix C and present results in Figure 20 and Table 9. Our Starfish analysis produces generally consistent physical parameters but with more realistic error esti-

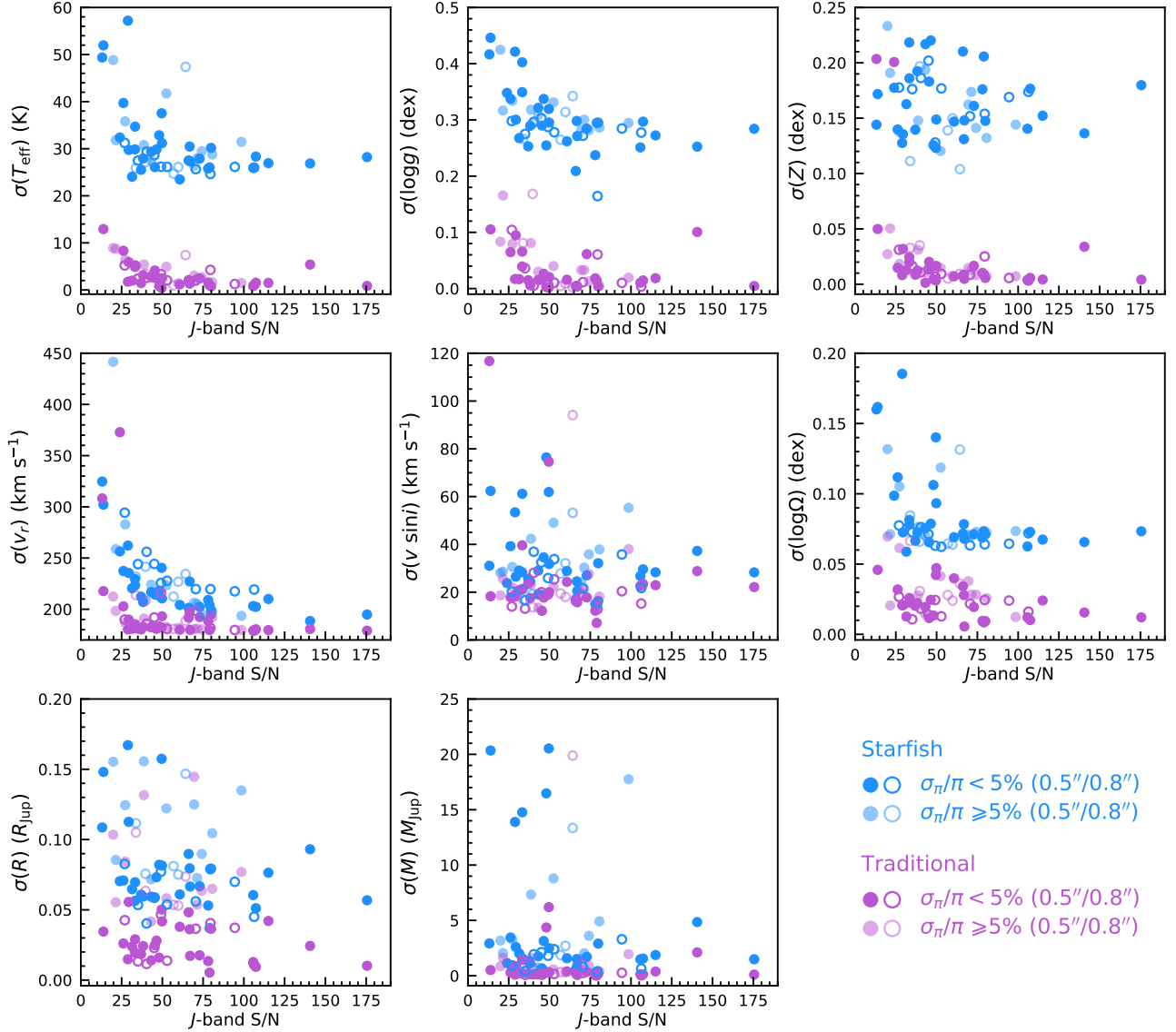


Figure 4. Parameter uncertainties from Starfish (blue) and traditional (purple; Appendix C) forward-modeling analysis as a function of the J -band S/N, i.e., the median S/N in $1.2 - 1.3 \mu\text{m}$. We use solid circles for results using spectra taken with the $0.5''$ slit and open circles for the $0.8''$ slit. The uncertainties of $\{T_{\text{eff}}, \log g, Z, v_r, v \sin i, \log \Omega\}$ have a significant spread at low S/N, but then shrink to lower values at $\text{S/N} \gtrsim 50$. Such trends also hold for R and M uncertainties of the objects with high-precision parallaxes (e.g., $\sigma_{\pi}/\pi < 5\%$). The v_r uncertainties derived from the lower-resolution spectra ($0.8''$ slit) are systematically larger than those from the higher-resolution ones as expected. Also, the v_r uncertainties from both Starfish and traditional spectral-fitting methods are larger than the 180 km s^{-1} uncertainty in the wavelength calibration of the SpeX prism data.

mates than the traditional approach. We therefore adopt the Starfish-based properties as final results of our atmospheric model analysis and use them for subsequent discussions.

In the rest of this section, we study the impact of the data S/N and spectral resolution on our forward-modeling analysis (Section 3.2.1) and investigate the correlations among the inferred physical parameters (Section 3.2.2).

3.2.1. Impact of S/N and Spectral Resolution

Our near-infrared spectra span a wide range in J -band S/N³ from 15 – 180 (Table 1), and here we examine the impact of the S/N on the precision of our fitting results. Figure 4 plots uncertainties of the eight physical parameters $\{T_{\text{eff}}, \log g, Z, v_r, v \sin i, \log \Omega, R, M\}$ as a function of J -band S/N. The uncertainties of the first six parameters have a

³ The median S/N around the J -band peak, i.e., $1.2 - 1.3 \mu\text{m}$, of the object's spectra.

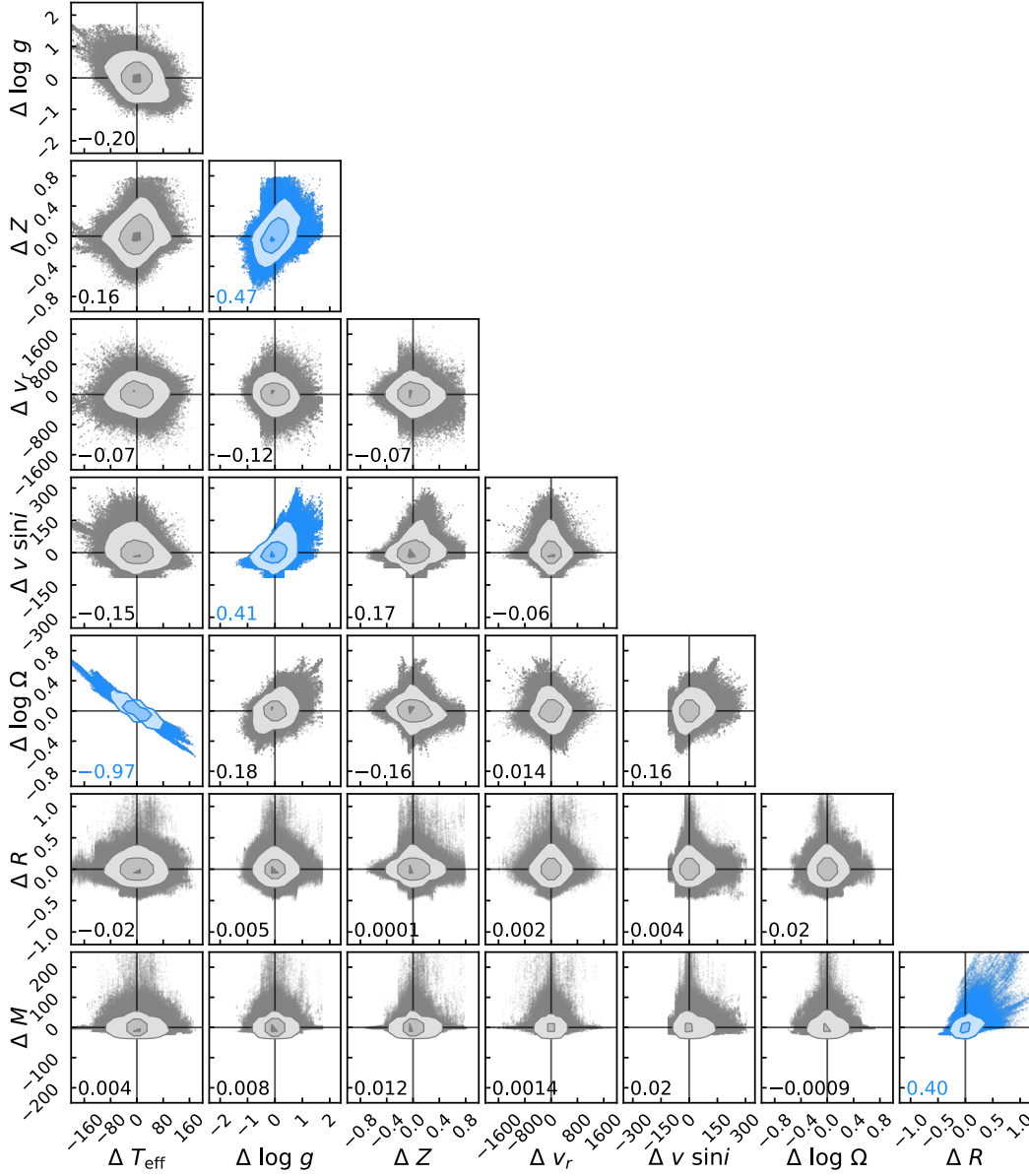


Figure 5. Stacked posteriors of the eight physical parameters $\{T_{\text{eff}}, \log g, Z, v_r, v \sin i, \log \Omega, R, M\}$ from all the MCMC chains of our late-T dwarf sample. These chains have been subtracted by their medians, so they represent the deviations of parameter posteriors from median values, which we denote as $\Delta T_{\text{eff}}, \Delta \log g, \Delta Z$, etc. We stack all the modified chains, generate stacked posteriors, and compute the Pearson correlation coefficients between each pair of parameters and give the coefficient values in the lower left corner of each panel. Most parameter pairs have very weak correlations (grey) with the absolute values of their coefficients below 0.2. We find four parameter pairs (blue) with large correlation coefficients (absolute values above 0.4): $(\Delta T_{\text{eff}}, \Delta \log \Omega)$, $(\Delta R, \Delta M)$, $(\Delta \log g, \Delta v \sin i)$, and $(\Delta \log g, \Delta Z)$. The strong correlations within the first three pairs are as expected, while the fourth one suggests a $\log g - Z$ degeneracy (Equation 1) in our forward-modeling analysis.

significant spread at low S/N, but then shrink to small value at $S/N \gtrsim 50$. We note the Starfish-derived parameter errors at high S/N ($\gtrsim 50$) are in fact dominated by modeling systematics (instead of measurement uncertainties), which constitute $\approx 2\% - 4\%$ of the peak J -band flux of late-T dwarf spectra (see Section 6.1) and cause the parameter precision to be independent of the data S/N in this regime. The precision of R and M depends not only on the S/N of spectra but also on

the parallax uncertainties. The R and M uncertainties of the objects with higher-precision parallaxes (e.g., relative uncertainties $\lesssim 5\%$) have the same dependence on S/N as the first six physical parameters.

We also investigate the impact of spectral resolution, since our sample contains spectra observed with both the $0.5''$ ($R \approx 80 - 250$) and $0.8''$ ($R \approx 50 - 160$) slits. As shown in Figure 4, the radial velocity uncertainties derived from the

lower-resolution spectra are systematically larger than those from the higher-resolution ones, as expected, but such distinction between the two resolutions is not seen for the other parameters.

Two objects in our sample, WISEPA J171104.60 + 350036.8 (WISE 1711 + 3500; Kirkpatrick et al. 2011) and WISE J004945.61 + 215120.0 (WISE 0049 + 2151; Mace et al. 2013a), have spectra taken with both slits. Comparing results from each object with the two resolutions, we find almost all parameters are consistent within 0.6σ . The only exception is the radial velocity of WISE 1711 + 3500, where the inferred values between the two slits differ by 2.1σ . WISE 1711 + 3500 is a resolved $0.78''$ T8+T/Y binary (Liu et al. 2012; also see Section 4), so the two slits will exclude different amounts of the integrated light from the system and may cause the discrepant radial velocities. Also, the J -band S/N of this object's $0.5''$ spectrum is quite low (≈ 20) compared to the $0.8''$ spectrum ($S/N \approx 35$), so the radial velocity inferred from the $0.5''$ spectrum might be less accurate.⁴

3.2.2. Parameter Correlations via Stacked Posteriors

We now investigate the correlations between the physical parameters $\{T_{\text{eff}}, \log g, Z, v_r, v \sin i, \log \Omega, R, M\}$. The correlations can shed light on how parameters change when one is under- or over-estimated. This information is useful when we examine the results from previous forward-modeling analyses (e.g., Cushing et al. 2008; Stephens et al. 2009), which relied on only solar-metallicity model atmospheres to analyze ultracool dwarfs which might have sub-solar or super-solar metallicities.

To investigate the parameter correlations, we stack the parameter posteriors of all our late-T dwarfs which are directly from the formal spectral fitting and have no systematic errors incorporated.⁵ For each object's chain, we first subtract the median of each posterior so that the chain then represents the deviations of the posteriors from the median values, which we denote as $\Delta T_{\text{eff}}, \Delta \log g, \Delta Z$, etc. Then we concatenate all the modified chains to generate the stacked parameter posteriors (Figure 5). We use these stacked posteriors to compute the Pearson correlation coefficients between all pairs of parameters. We find that four pairs exhibit significant correlations: $(\Delta T_{\text{eff}}, \Delta \log \Omega)$, $(\Delta R, \Delta M)$, $(\Delta \log g, \Delta v \sin i)$, and $(\Delta \log g, \Delta Z)$. The correlations within the first three pairs are expected: (1) effective temperature and solid angle

are naturally correlated due to the Stefan-Boltzmann law; (2) the mass is computed from radii and surface gravity and has a stronger dependence on radii; and (3) the inferred $v \sin i$ value of each object is primarily constrained by the prior, which is determined by surface gravity, solid angle, and distance (Section 3.1 and Equation 2 of Paper I).

The fourth correlation between $\log g$ and Z is interesting. Conducting an orthogonal distance regression to the modified chains of $\Delta \log g$ and ΔZ using a straight line across the origin, we derive the following relation:

$$\Delta \log g = 3.42 \times \Delta Z \quad (1)$$

The qualitative form of such $\log g - Z$ relation has been noted from previous spectroscopic analyses using other model atmospheres (e.g., Burgasser et al. 2006a; Leggett et al. 2007; Liu et al. 2007; Burningham et al. 2009). The cause of this degeneracy is that these two parameters have similar effect on the spectral morphology of cloudless model atmospheres, as either a high (low) $\log g$ or a low (high) Z leads to the same suppressed (enhanced) K -band flux in late-T dwarf spectra. In addition, we find that Z has the noticeable correlation only with the $\log g$ parameter in our analysis, suggesting that applying the solar-metallicity cloudless Sonora-Bobcat models to late-T dwarfs whose true metallicities are non-solar can bias $\log g$ but not the other parameters.

4. BINARY SYSTEMS

Now we examine binary systems in our sample, for which our derived atmospheric model properties will be not reliable. This is because some of the integrated light from these systems might be missing from our prism spectra (depending on their angular separations relative to the $0.5''$ and $0.8''$ slit widths), and our spectral-fitting process assumes all objects are single. We first discuss known resolved binaries (Section 4.1) and then identify candidate binaries based on their spectrophotometric properties (Section 4.2). In the end, we exclude six known or likely binaries from our subsequent discussions.

4.1. Resolved Binaries

Three late-T dwarfs in our sample are known to be resolved binaries: 2MASS J1553022 + 153236 (2MASS 1553 + 1532), WISE 1711 + 3500, and WISEPA J045853.89 + 643452.9 (WISE 0458 + 6434). 2MASS 1553 + 1532 (T7) is a resolved $0.35''$ T6.5+T7 binary (Burgasser et al. 2006c), with a bolometric luminosity ratio of 0.31 ± 0.12 mag and a mass ratio of 0.90 ± 0.02 ⁶. Our fitted model spectra

⁴ The J -band S/N of WISE 0049 + 2151 (which does not show the discrepant atmospheric parameters between two slits) is ≈ 80 for its $0.5''$ spectrum and ≈ 35 for its $0.8''$ spectrum.

⁵ We note the parameter correlation involves the change of parameters' median values (due to the intrinsic parameter degeneracy). The systematic errors incorporated to our results only slightly inflate the parameter uncertainties (instead of their median values; Section 3.1) and thus have no impact to the parameter correlations that we investigate here.

⁶ Burgasser et al. (2006c) estimated the bolometric luminosity of binary components using their HST/NICMOS resolved photometry and a bolometric correction, which they derived as a function of near-infrared colors using

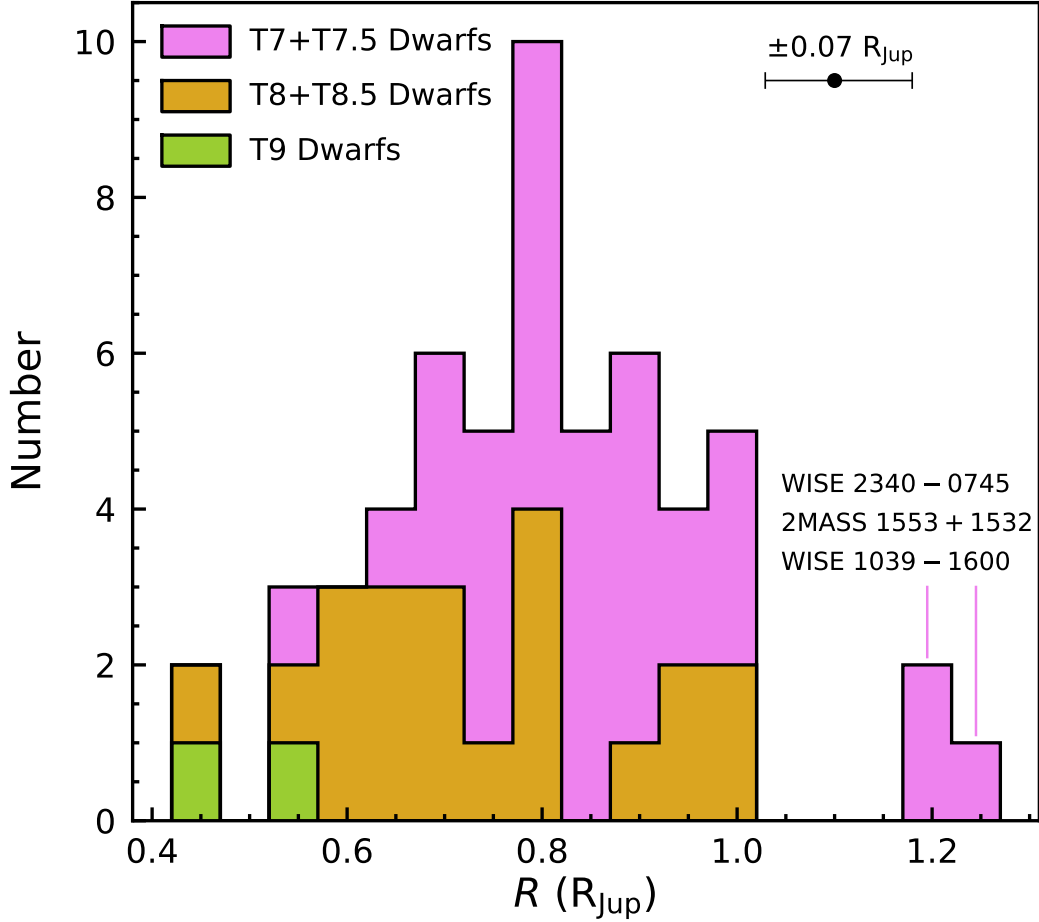


Figure 6. Distribution of our derived atmospheric radii for late-T dwarfs (violet for T7 and T7.5, orange for T8 and T8.5, and green for T9). We label the three objects whose radii stand out with large values, among which 2MASS 1553 + 1532 is a resolved binary and the other two are candidate binaries (Section 4).

of this object match the observed spectrum, but the fitted $R = 1.21^{+0.10}_{-0.09} R_{\text{Jup}}$ stands out from our sample (Figure 6) and is larger than the evolutionary model predictions ($\approx 0.75 - 1.20 R_{\text{Jup}}$; e.g., Burrows et al. 1997; Saumon & Marley 2008; Marley et al. submitted), as well as the directly measured radii of transiting brown dwarfs, e.g., KELT-1b ($1.116^{+0.038}_{-0.029} R_{\text{Jup}}$; Siverd et al. 2012), KOI-205b ($0.81 \pm 0.02 R_{\text{Jup}}$; Díaz et al. 2013), and LHS 6343 C ($0.783 \pm 0.011 R_{\text{Jup}}$; Montet et al. 2015). The large radii of 2MASS 1553 + 1532 is in accord with its nearly equal-brightness binarity. A similar large spectroscopic radii ($R = 1.59^{+0.14}_{-0.09} R_{\text{Jup}}$) was inferred by Line et al. (2017) based

the photometry of unresolved T dwarfs in their sample and the K -band bolometric correction from Golimowski et al. (2004). Burgasser et al. estimated the mass of the binary components using the objects’ effective temperatures based on the Golimowski et al. (2004) T_{eff} -SpT relation, an assumed age of 0.5 – 5.0 Gyr, and the Burrows et al. (1997) evolutionary models.

on their retrieval analysis which also did not account for binarity.

WISE 1711 + 3500 (T8) is a resolved $0.78''$ T8+T/Y binary (Liu et al. 2012). The binary has near-infrared ($YJHK$ bands) flux ratios of 2.6 – 3.1 mag, indicating the integrated-light spectra of this system is dominated by the T8 primary. This might explain why its fitted radii $R = 0.93^{+0.16}_{-0.12} R_{\text{Jup}}$ is not as large as the nearly equal-brightness binary 2MASS 1553 + 1532.

WISE 0458 + 6434 (T8.5) is a resolved $0.51''$ T8.5+T9 binary (Gelino et al. 2011; Burgasser et al. 2012; Leggett et al. 2019) with near-infrared (JHK bands) flux ratios of 1.0 – 1.1 mag. The fitted model spectra from our analysis do not match the observed spectrum and predict too faint H -band fluxes. Also, this object’s parameter posteriors are bimodal based on the traditional method (Appendix C), with one peak consistent with the Starfish results and the other peak being 160 K cooler in T_{eff} , 1.5 dex higher in $\log g$, and 0.2 dex higher in Z . While the bimodal posteriors might

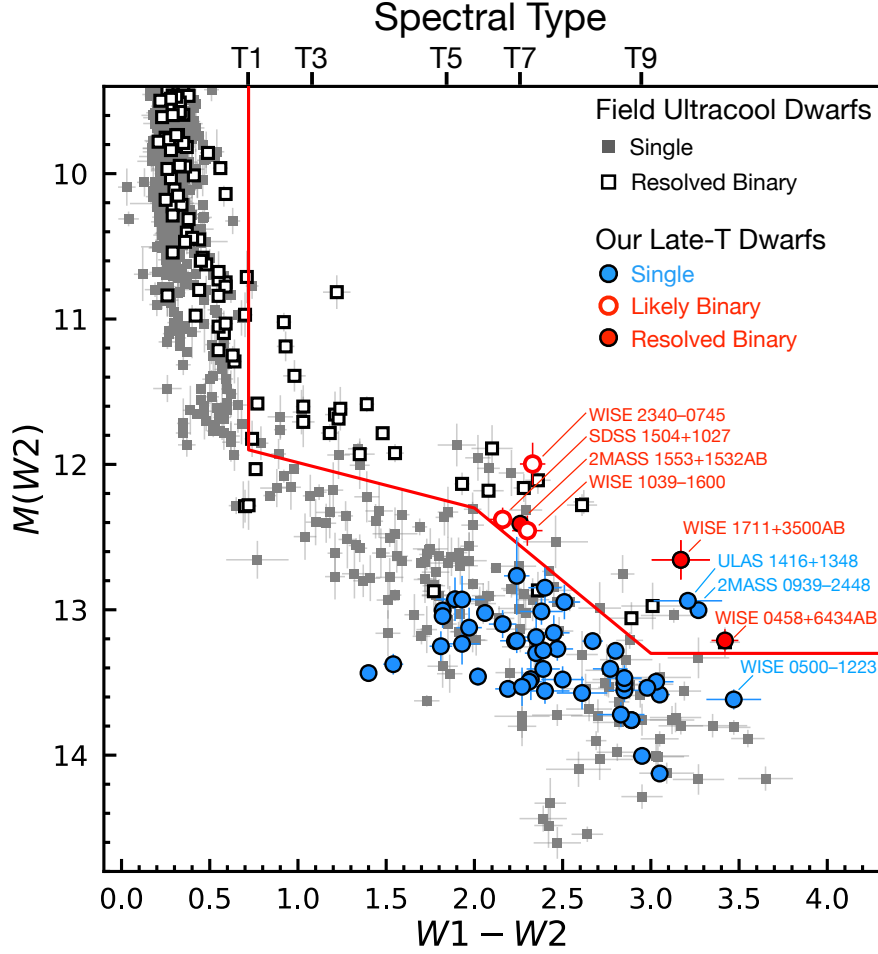


Figure 7. $W2$ -band absolute magnitudes as a function of $W1 - W2$ colors for our late-T dwarfs and field ultracool dwarfs (Best et al. 2020b) whose absolute magnitudes and colors both have $S/N > 5$. We use red solid circles for resolved late-T binaries in our sample (Section 4.1), red open circles for likely binaries (Section 4.2), and blue solid circles for the remaining. For the field objects, we use white squares for resolved ultracool binaries and solid squares for those which are single or have unknown binarity. The upper x-axis shows corresponding T spectral types based on median $W1 - W2$ colors of field dwarfs from Best et al. (2018). We draw a line in the diagram to help distinguish the T-type resolved binaries from the others, with the boundary defined by points of $(W1 - W2, M(W2)) = (0.72, 9.4), (0.72, 11.9), (2, 12.3), (3, 13.3), (4.5, 13.3)$. T-type binaries tend to have brighter magnitudes and redder colors than such boundary in this diagram, but we caution that low-metallicity, high-gravity single objects might occupy the same area as the resolved binaries (Section 4.2).

be due to the object’s binarity, they are likely caused by the low J -band $S/N = 24$ of the data, which prevents the spectral-fitting process from converging on a unique set of solutions.

We exclude all these three known binaries from our subsequent analysis (Sections 5 and 6).

4.2. Candidate Binaries

Here we choose three criteria to identify candidate binaries in our sample based on their fitted model parameters and observed photometry:

- (1) The fitted R are outliers in the derived radii distribution of our sample (Figure 6) with very large values (e.g., $\gtrsim 1.2 R_{\text{Jup}}$),

- (2) The parameter posteriors derived from either Starfish or traditional forward-modeling analysis are bimodal, or
- (3) The AllWISE photometry is brighter and redder than most other objects in our sample, with critical values shown in Figure 7.

Figure 7 compares the integrated-light photometry of our late-T dwarfs to known field dwarfs from Best et al. (2020a), which shows that T-type resolved binaries have distinctly brighter $W2$ -band absolute magnitudes and redder $W1 - W2$ colors than the majority of field dwarfs which are single (or not known to be binaries). We draw a line in Figure 7 to help distinguish the resolved binaries from the others. We caution that this line can also select single objects with

high-gravity, metal-poor atmospheres, as demonstrated by 2MASS 0939 – 2448 and ULAS 1416 + 1348 (discussed further below). Either high gravity or low metallicity can cause the objects’ photospheres to reside at higher pressures, favoring the formation of CH₄ (with strong absorption in *W1*) over CO (with strong absorption in *W2*; e.g., Liebert & Burgasser 2007; Zahnle & Marley 2014; Leggett et al. 2017). This leads to redder *W1* – *W2* colors and might make such objects have similar AllWISE photometry as binaries.

We select candidate binaries whose properties satisfy at least one of our criteria and end up with six objects: WISE J103907.73 – 160002.9 (WISE 1039 – 1600), WISEPC J234026.62 – 074507.2 (WISE 2340 – 0745), WISEPA J050003.05 – 122343.2 (WISE 0500 – 1223), 2MASS J09393548 – 2448279 (2MASS 0939 – 2448), ULAS 1416 + 1348, and SDSS J150411.63 + 102718.4 (SDSS 1504 + 1027). Based on the recent near-infrared adaptive optics imaging (M. Liu, private communication), all these candidates are unresolved down to 0.1″, making their potential binarity intriguing.

WISE 1039 – 1600 (T7.5) and WISE 2340 – 0745 (T7) are selected by both the first and third criteria, with their spectroscopically inferred radii among the largest in our sample (Figure 6) and their AllWISE photometry being anomalous (Figure 7). The fitted model spectra of these two objects match the observed spectra, so their large radii are unlikely caused by poorly fitted models. Also, their kinematics do not support membership in any young associations (based on BANYAN Σ [Gagné et al. 2018] or LACEwING [Riedel et al. 2017]; see Zhang et al. 2021) and their fitted $\log g$ are consistent with the other late-T dwarfs in our sample. Therefore, we find no evidence of youth that would lead to their large radii (e.g., Burrows et al. 2001; Kirkpatrick et al. 2008; Allers & Liu 2013). In addition, their near-infrared spectra do not exhibit any peculiarities that might result from high-gravity, metal-poor atmospheres. Therefore, we conclude their large atmospheric radii and atypical AllWISE photometry are likely caused by binarity.

WISE 0500 – 1223 (T7) is selected by the second criterion, i.e., bimodal posteriors from atmospheric model analysis. Similar to WISE 0458 + 6434, the parameter posteriors of this object based on the traditional forward-modeling analysis have two peaks, with one consistent with the Starfish results, and the other being 120 K cooler in T_{eff} , 1.5 dex higher in $\log g$, and 0.4 dex higher in Z . Its *W2*-band absolute magnitude is fainter than our critical line in Figure 7, although this line is not well-established around the *W1* – *W2* = 3.47 ± 0.16 mag of WISE 0500 – 1223, given that there are too few known binaries with such red colors. While the bimodal posteriors of this object could be caused by binarity, we note the low *J*-band S/N ≈ 13 of data might

also cause this anomaly. We thus suggest a re-analysis of this system using higher-quality data.

The remaining three candidates are all selected by the third criterion, i.e., anomalous AllWISE photometry. 2MASS 0939 – 2448 (T8) has a metal-poor atmosphere given its broad *Y*-band and faint *K*-band spectra. We derive a low metallicity, $Z = -0.41^{+0.15}_{-0.09}$ dex, which is consistent with the past forward-modeling (Burgasser et al. 2006a, 2008b; Leggett et al. 2009) and retrieval analyses (Line et al. 2017). Combining near-infrared and mid-infrared spectra, both Burgasser et al. (2008b) and Leggett et al. (2009) have suggested 2MASS 0939 – 2448 is an unresolved binary, primarily due to its uncommon brightness in the mid-infrared. However, Dupuy & Liu (2012) suggested that 2MASS 0939 – 2448 might be a single object with a very red *W1* – *W2* color due to its low metallicity and/or high gravity, given that its near-infrared absolute magnitudes are not brighter than field dwarfs with similar spectral types.

ULAS 1416 + 1348 (T7.5) is a 9″ (85 au) companion (Burningham et al. 2010b; Scholz 2010a) to a L6 dwarf SDSS J141624.08+134826.7 (Bowler et al. 2010a; Schmidt et al. 2010).⁷ Burningham et al. (2010b) noted the unusually red *H* – *W2* and *W1* – *W2* colors of this object and connected these properties to its metal-poor atmosphere. The very blue *Y* – *K* color of this companion suggests high gravity and low metallicity, in accord with our derived $\log g = 5.21^{+0.26}_{-0.25}$ dex and $Z = -0.39^{+0.14}_{-0.11}$ dex, which are consistent with past spectral analyses (Burgasser et al. 2010b; Line et al. 2017; Gonzales et al. 2020).⁸ Kirkpatrick et al. (2019) suggested ULAS 1416 + 1348 is an unresolved binary, given that three known late-T subdwarfs (BD +01° 2920B [Pinfield et al. 2012], Wolf 1130C [Mace et al. 2013b], and WISE J083337.82+005214.1 [Pinfield et al. 2014]) have similar positions as field dwarfs in the M_H vs. *H* – *W2* diagram whereas ULAS 1416 + 1348 is an apparent outlier.

SDSS 1504 + 1027 (T7) has a normal near-infrared spectrum given its spectral type, and our fitted model spectra match the data (*J*-band S/N of 50 per pixel). Aberasturi et al. (2014) obtained high spatial-resolution images using HST/WFC3 and did not resolve this object down to a

⁷ The primary has weak TiO and CaH absorption features in optical, an unusually blue *J* – *K* color, enhanced FeH 0.99 μm absorption, deep H₂O absorption features, and thin-disk kinematics (e.g., Bowler et al. 2010a; Schmidt et al. 2010). Bowler et al. (2010a) suggested these features are caused by the object’s low metallicity and its less-opaque condensate clouds than the majority of L6 dwarfs (similar to the blue L4.5 dwarf 2MASS J11263991 – 5003550 as discussed by Burgasser et al. 2008a). The metallicity and age of the system are not well constrained as compared to the three benchmark companions (HD 3651B, GJ 570D, and Ross 458C) studied in Paper I.

⁸ The best-fit parameters derived by Burgasser et al. (2010b) using the Saumon & Marley (2008) spectral models also favors a weak-mixing atmosphere with the vertical diffusion coefficients of $K_{zz} = 10^4 \text{ cm}^2 \text{ s}^{-1}$.

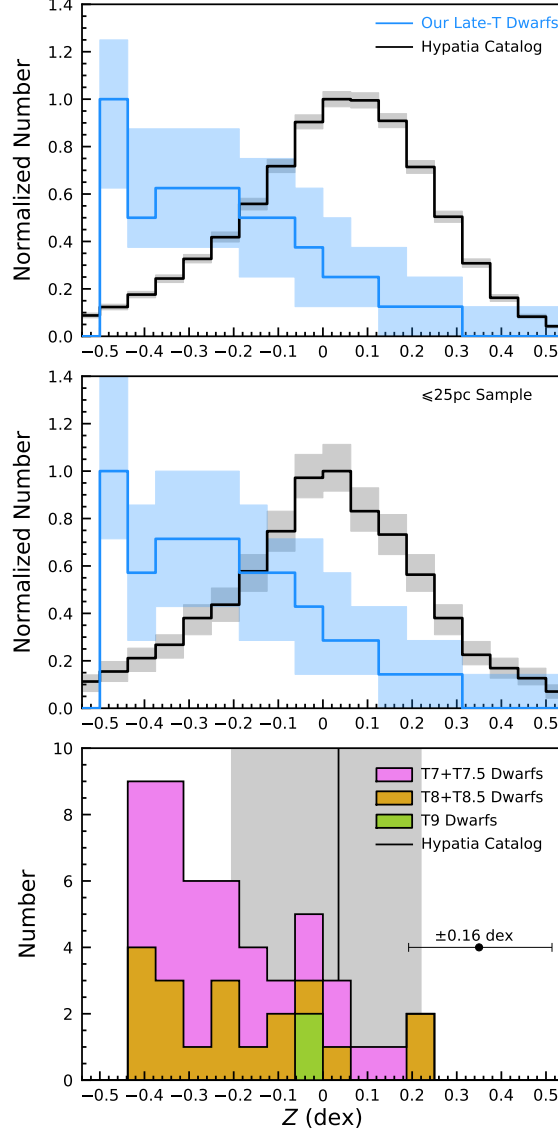


Figure 8. Top: Metallicity distributions for late-T dwarfs (binaries removed) from our atmospheric model analysis and for thin-disk stars from the Hypatia catalog (Hinkel et al. 2014, 2016, 2017). For our late-T dwarfs, we generate 10^4 metallicity distributions with each constructed by a random draw from each object’s Z posterior. We then plot the median and the 1σ confidence interval of these distributions using the blue line and shadow, respectively. Distributions for Hypatia stars (black) are produced in the same approach except that we assume the metallicity of each star follows a Gaussian distribution. We normalize these two types of distributions so that their peaks correspond to one. Middle: Similar format as the top but with late-T and stellar samples constrained to ≤ 25 pc. Bottom: The distribution of our late-T dwarfs, with the violet color for T7 and T7.5, orange for T8 and T8.5, and green for T9. Our typical Z uncertainty is shown as the black error bar. We use the vertical black line and grey shadow to mark the median (0.04 dex) and the 1σ spread (-0.21 to 0.22 dex) of the Hypatia stars.

resolution of $0.096'' - 0.142''$ and a magnitude contrast of $1.5 - 2.0$ mag.

To conclude, we flag WISE 1039 – 1600, WISE 2340 – 0745, and SDSS 1504 + 1027 as likely binaries, and exclude them from our subsequent analysis (Sections 5 and 6) along with the three known binaries discussed in Section 4.1. For the remaining candidates, WISE 0500 – 1223, 2MASS 0939 – 2448, and ULAS 1416 + 1348, we keep them in our analysis, given that their anomalous spectrophotom-

etry is likely caused by low-S/N data or abnormal atmospheres. However, we do not rule out the possibility that these objects are tight unresolved binaries.

5. ATMOSPHERIC PROPERTIES OF LATE-T DWARFS

Here we examine our forward-modeling results on the distributions of metallicities (Section 5.1) and ages (Section 5.2) of late-T dwarfs, as well as their effective temperature–spectral type relation (Section 5.3). We demonstrate spectral-

fitting results for an ensemble of objects can provide useful diagnostics about the physical assumptions made within model atmospheres, by virtue of having a large sample of spectra over a focused spectral type range (as opposed to a smaller sample of objects spanning a wide spectral type range).

5.1. Metallicity Distribution

We investigate the metallicity of 49 late-T dwarfs⁹ in our sample (with the other 6 objects excluded due to their known or likely binarity; Section 4) and compare them to metallicities of nearby stars. This analysis can in principle assess whether these two populations have similar formation histories but can also shed light on the accuracy of our fitted atmospheric properties.

Spectroscopic analysis of stellar metallicities and elemental abundances involves (1) measuring equivalent widths of individual absorption lines and then converting them into abundances using the curve of growth and theoretical line lists (e.g., [Edvardsson et al. 1993](#); [Santos et al. 2004](#); [Bond et al. 2006](#); [Ramírez et al. 2013](#); [Soto & Jenkins 2018](#)), or (2) fitting the entire observed spectra using stellar model atmospheres with a range of abundances (e.g., [Valenti & Fischer 2005](#); [Jenkins et al. 2008](#); [Petigura & Marcy 2011](#); [Brewer et al. 2016](#)). The abundances of several thousands of nearby ($\lesssim 100$ pc) stars have been studied via high-resolution spectroscopy ($R \gtrsim 3 \times 10^4$). The vast majority of these stars have similar iron content ($[\text{Fe}/\text{H}]$) as our Sun (e.g., Figure 4 of [Hinkel et al. 2014](#)). While it has been known that different methods, line lists, and spectral resolutions can lead to notable spreads in the derived metallicities and elemental abundances (e.g., [Torres et al. 2012](#); [Smiljanic et al. 2014](#); [Hinkel et al. 2016](#); [Ivanyuk et al. 2017](#)), much effort has been made to construct large, homogeneous stellar abundance catalogs (e.g., [Hinkel et al. 2014, 2017](#); [Brewer et al. 2016](#)).

In contrast, systematic metallicity analysis of substellar objects has been lacking in most previous spectroscopic studies. For late-type ultracool dwarfs, direct metallicity measurements from atomic/molecular absorption features are particularly challenging, given that (1) the spectral continuum required for computing absorption depths is hard to determine due to the presence of very broad molecular bands (e.g., H_2O and CH_4) and (2) elemental abundances cannot be entirely tracked by the observed absorption features, as some portions of species might have been perturbed by vertical mixing and/or sequestered into condensates and thereby sinking to below the photosphere (e.g., [Fegley & Lodders 1994](#); [Line](#)

[et al. 2017](#)). Metallicity estimates are viable using model atmosphere analyses. While there has been previous such studies for one to a few objects (e.g., [Saumon et al. 2007](#); [Bowler et al. 2010b](#); [Leggett et al. 2017](#)), many analyses have used models with only the solar metallicity (e.g., [Cushing et al. 2008](#); [Stephens et al. 2009](#); [Del Burgo et al. 2009](#); [Liu et al. 2011a](#); [Schneider et al. 2015](#); [Deacon et al. 2017](#)).

Recently, some studies have begun characterizing metallicities for large samples of ultracool dwarfs. [Zhang et al. \(2017; 2018b\)](#) studied 28 M7–L7 subdwarfs with thick-disk or halo membership. They determined the objects’ physical properties by visually comparing their optical and near-infrared spectra to BT-Settl model atmospheres ([Allard et al. 2011](#); [Allard 2014](#)) and found low $[\text{Fe}/\text{H}]$ values, spanning -2.5 to -0.5 dex. [Leggett et al. \(2017\)](#) visually compared near-infrared spectra of 20 Y dwarfs to the [Tremblin et al. \(2015\)](#) models, which assume cloudless atmospheres with dis-equilibrium chemistry and reduced vertical temperature gradient, and found solar-like metallicities with a spread of ± 0.3 dex. [Line et al. \(2017\)](#) conducted a retrieval analysis for 11 late-T dwarfs and found notably lower metallicities (spanning -0.4 to 0.1 dex) and higher carbon-to-oxygen ratios (C/O) than nearby FGK stars. These results are likely related to the sequestration of oxygen into condensates in late-T atmospheres, which then rain out of the photosphere (e.g., [Fegley & Lodders 1994](#); [Marley & Robinson 2015](#)), resulting in retrieved metallicities and C/O that are systematically too low and high, respectively. Applying the [Line et al. \(2017\)](#) methodology to 14 late-T and Y dwarfs, [Zalesky et al. \(2019\)](#) derived metallicities that span -0.2 to 0.6 dex, which are consistent with (if not slightly higher than) those of nearby stars.

Our work analyzes 49 late-T dwarfs and thus constitutes the largest homogeneous analysis of brown dwarf metallicities to date. Figure 8 compares the derived metallicities of our late-T dwarfs to those of F0–M4 stars from the Hypatia catalog¹⁰ ([Hinkel et al. 2014, 2016, 2017](#)). The latest version of this catalog (as of June 2019, compiling nearly 200 literature studies) contains 6196 stars within 150 pc that have spectroscopically determined $[\text{Fe}/\text{H}]$ and at least one other element. This compilation of stellar abundance is homogeneous in a sense that [Hinkel et al.](#) carefully examined the results reported by different studies for the same element within the same star and normalized all abundances to the same solar scale by [Lodders et al. \(2009\)](#). We only include thin-disk Hypatia stars (5021 objects) in our analysis and find these objects have a median metallicity of $Z = 0.04$ dex with a 1σ confidence interval (i.e., 16th-to-84th percentiles) of -0.21 to 0.22 dex. In comparison, our 49 late-T dwarfs have much

⁹ Among these objects, WISE 0049 + 2151 has two sets of atmospheric model parameters, derived from $0.5''$ and $0.8''$ spectra (Section 3.2.1). These results are consistent, and we use those determined from the higher-S/N $0.5''$ spectrum.

¹⁰ <https://www.hypatiacatalog.com/hypatia>.

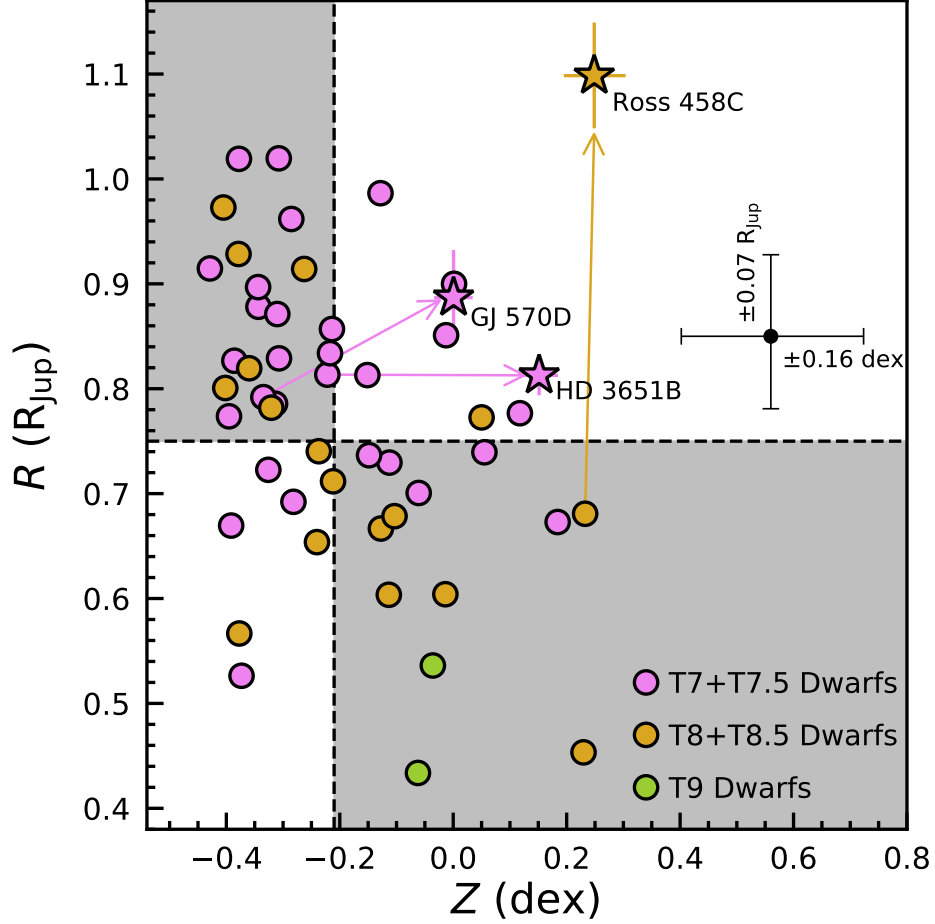


Figure 9. Our spectroscopically inferred R and Z for late-T dwarfs (binaries removed; violet for T7 and T7.5, orange for T8 and T8.5, and green for T9), with typical uncertainties shown as black error bars. We use two dashed lines for $Z = -0.21$ dex and $R = 0.75 R_{\text{Jup}}$ to divide the space into four parts. Objects located in the upper left area (i.e., $Z < -0.21$ dex and $R \geq 0.75 R_{\text{Jup}}$) have metallicities that are $> 1\sigma$ lower than Hypatia stars but their radii appear reasonable. They might be in similar situations as GJ 570D and HD 3651B, whose fitted Z are underestimated by ≈ 0.35 dex but their R are reliable, as noted in Paper I. Objects located in the lower right area (i.e., $Z \geq -0.21$ dex and $R < 0.75 R_{\text{Jup}}$) have solar-like metallicities but unphysically small radii. Some of them might be in a similar situation as Ross 458C whose fitted Z is reliable but R is underestimated by a factor of ≈ 1.6 . The evolutionary model parameters of three benchmark companions (derived from Paper I) are shown as stars and connected to their spectroscopically inferred parameters by arrows.

lower metallicities, spanning -0.43 to 0.23 dex and with a median and mode of -0.24 dex and -0.40 dex, respectively. We run the Kolmogorov-Smirnov (K-S) test for metallicities of Hypatia stars and our late-T dwarfs in a Monte Carlo fashion¹¹ and obtain p -values that are all smaller than 2×10^{-3} , thereby indicating they are not drawn from the same distribution. These two samples' metallicity distributions are largely

unchanged when we limit our comparison to ≤ 25 pc for our late-T dwarfs (47 objects) and the Hypatia stars (590 objects; Figure 8), with the K-S test providing similarly small p -values of < 0.02 (with a median of 2×10^{-7}).

To examine whether the metallicity discrepancy between late-T and stellar populations is physical, we first analyze the accuracy of our derived Z values. As shown in Figure 9, 30 late-T dwarfs have Z of -0.43 to -0.21 dex and are thus $> 1\sigma$ lower than the Hypatia stellar metallicity. Most of these objects have $R = 0.75 - 1.2 R_{\text{Jup}}$ from our atmospheric modeling, consistent with the evolutionary model predictions and directly measured radii of transiting brown dwarfs (see Section 4.1). The remaining 19 ($= 49 - 30$) late-T dwarfs have higher Z of -0.15 to 0.23 dex that are consistent with those

¹¹ We generate 10^4 distributions of Hypatia stellar metallicities, with each distribution constructed by a random draw from each object's measured Z and errors by assuming a Gaussian distribution. We generate 10^4 distributions of our late-T dwarfs' metallicities in a same approach except that we draw each object's metallicities from its atmospheric-based Z posterior. We then run the K-S test for each pair of Hypatia and late-T distributions and compute the corresponding p -values.

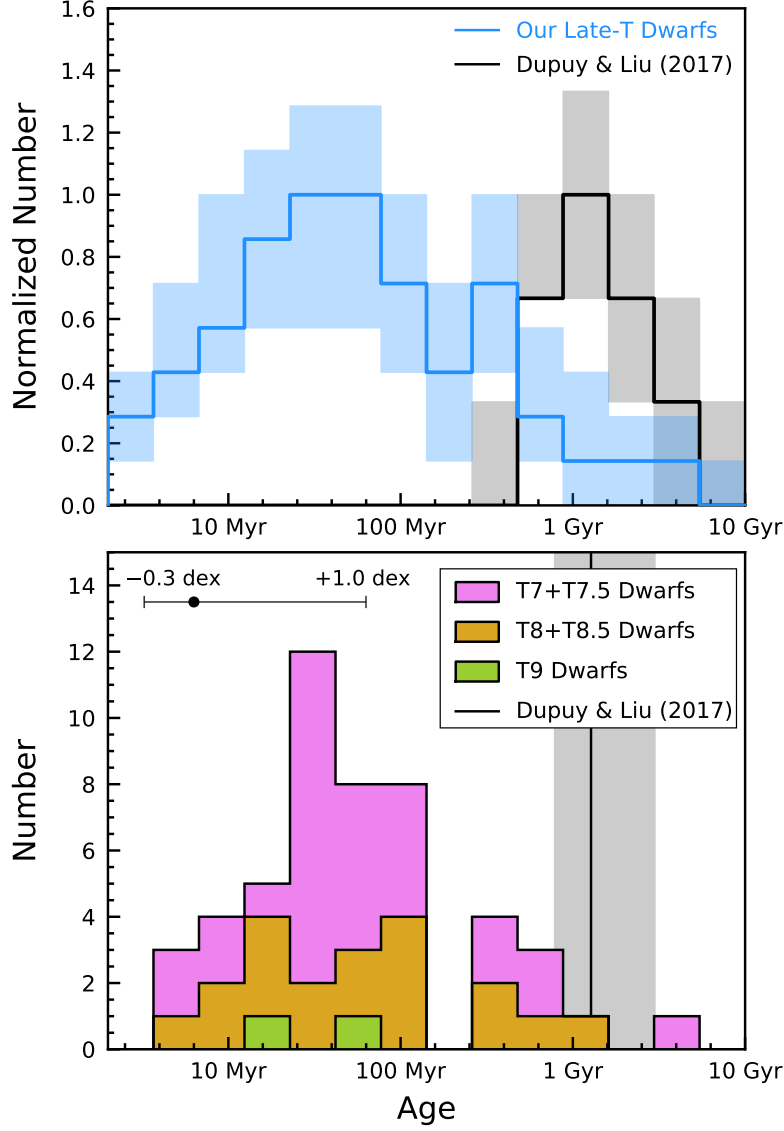


Figure 10. Top: Age distributions for our late-T dwarfs (binaries removed) and for benchmark binaries with dynamical masses from Dupuy & Liu (2017). We compute age posteriors for our late-T dwarfs using the spectroscopically inferred $\{T_{\text{eff}}, \log g, Z\}$ values at each step of the MCMC chains and the interpolated Sonora-Bobcat evolutionary models. We then generate 10^4 distributions with each constructed by a random draw from each object’s age posterior. We plot the median and the 1σ confidence interval of these distributions using the blue line and shadow. Distributions for the Dupuy & Liu (2017) sample are produced in the same approach using the age posteriors of the mass benchmarks (T. Dupuy, private communication). We normalize these two types of distributions so that their peaks correspond to one. Bottom: The distribution of our late-T dwarfs, with the violet color for T7 and T7.5, orange for T8 and T8.5, and green for T9. Our typical logarithmic age uncertainty is shown as the black error bar. We use the vertical black line and shadow to mark the median (1.3 Gyr) and the 1σ spread (0.8 to 3.0 Gyr) of the Dupuy & Liu (2017) age distribution.

of Hyppatia stars, but most of these objects have unphysically small radii of $< 0.75 R_{\text{Jup}}$. Overall, we find a correlation between Z and R , where the objects with higher Z in our sample tend to have smaller R from our atmospheric model analysis.

This $Z - R$ correlation is in contradiction to the cloudless Sonora-Bobcat evolutionary models, which predict that objects with higher metallicities should have increased atmospheric opacity, slower cooling, and thereby larger radii at a

given mass and age (also see Burrows et al. 2011). Also, this correlation is not found in stacked posteriors of atmospheric parameters (Figure 5). Therefore, it is likely not due to the parameter degeneracy within the Sonora-Bobcat models or our spectral-fitting machinery.

This $Z - R$ trend might be because the spectroscopically inferred Z or R of our late-T dwarfs are underestimated. As shown in Paper I, the fitted metallicities of the two bench-

mark companions, HD 3651B and GJ 570D, are underestimated by ≈ 0.35 dex but their fitted radii are reliable, when compared to the radii derived from the Sonora-Bobcat evolutionary models (using these companions’ bolometric luminosities and their primary stars’ ages and metallicities). For another benchmark, Ross 458C, its fitted metallicity is consistent with evolutionary-based results but its fitted radii is underestimated by a factor of ≈ 1.6 . Among our sample, some objects with fitted $Z < -0.21$ dex and $R \geq 0.75 R_{\text{Jup}}$ might be in similar situations as HD 3651B and GJ 570D, while those with fitted $Z \geq -0.21$ dex and $R < 0.75 R_{\text{Jup}}$ might be in a similar situation as Ross 458C. Altogether, correcting the inaccurate atmospheric parameters of these late-T dwarfs would be the equivalent of shifting their Z toward higher values and/or their R toward larger values, which would alter the $Z - R$ correlation seen in Figure 9. The underestimation of these fitted parameters in our sample suggests the model assumptions of cloudless and chemical-equilibrium atmospheres are not adequate to fully interpret late-T dwarf spectra and should be further improved.

To conclude, many of our late-T dwarfs with low atmospheric Z might have values underestimated by as large as 0.3 – 0.4 dex, and this can explain the discrepant metallicity distributions between late-T dwarfs and Hyppatia stars. Thus, we cannot say more about whether the metallicities of nearby late-T dwarfs and stars are similar. More comprehensive understanding of substellar metallicities would benefit from the continuing discoveries of brown dwarfs as companions to stars or members of nearby associations. These objects can provide independent metallicities from their hosts and are thus “metallicity benchmarks” for calibrating forward-modeling analyses and improving our understanding of ultracool atmospheres.

5.2. Age Distribution

We proceed to study ages of our late-T dwarfs. The age distribution of field brown dwarfs is essential to constrain their formation history and initial mass function (e.g., Kirkpatrick et al. 2012; Day-Jones et al. 2013). However, it is challenging to age-date individual field brown dwarfs, given that their ages and masses are degenerate and thus the former cannot be well-constrained unless the latter is known independently. Previous work has estimated low-precision ages for large groups of ultracool dwarfs based on their kinematics. Such analysis is conducted in a statistical fashion and assumes the objects’ space motions exhibit a larger spread with time due to dynamical evolution (e.g., Wielen 1977). Comparing tangential or three-dimensional space velocities of late-M, L, and early-T dwarfs to those of earlier-type main-sequence stars, several studies have found that local ultracool dwarfs have slightly smaller velocity dispersions and perhaps younger ages (0.5 – 4 Gyr; e.g., Dahn et al. 2002;

Schmidt et al. 2007; Zapatero Osorio et al. 2007). However, based on tangential velocities of a large, volume-limited sample of M7–T8 objects within 20 pc, Faherty et al. (2009) suggested the kinematic age of ultracool dwarfs (3 – 8 Gyr) is indistinguishable from earlier-type stars, although the former indeed becomes younger (2 – 4 Gyr) after excluding thick-disk or halo-like objects with high tangential velocities ($> 100 \text{ km s}^{-1}$; also see Schmidt et al. 2007).

Thanks to the long-term astrometric monitoring, many brown dwarf binaries now have measured dynamical masses. These “mass benchmarks” (e.g., Liu et al. 2008) can disentangle the age-mass degeneracy of substellar objects and thus yield some of the most robust ages. Recently, Dupuy & Liu (2017; DL17) studied the largest sample of such benchmark binaries to date (31 systems) and derived ages from their measured dynamical masses and the Saumon & Marley (2008) evolutionary models. They derived a substellar age distribution from a high-quality subset of 10 systems (M8–T5 within 30 pc) and found a median and mean of 1.3 Gyr and 2.3 Gyr, respectively. This distribution is systematically younger than the past population synthesis analyses of Burgasser (2004) and Allen et al. (2005), which found that mid-L to early-T dwarfs have ages of $\approx 2 - 3$ Gyr (although the modeled age distribution at a given spectral type has a large spread, e.g., see Figure 8 of Burgasser 2004). The DL17 age distribution is in accord with Galactic dynamic heating preferentially scattering older substellar objects out of the immediate region ($\lesssim 50$ pc) around the Earth, which has been the main focus of brown dwarf searches.

Here we compare the DL17 age distribution to that of our late-T dwarf sample, for which we compute ages using the fitted $\{T_{\text{eff}}, \log g, Z\}$ values at each step of the MCMC chains and the interpolated cloudless Sonora-Bobcat evolutionary models (Table 5). Both our analysis and that of DL17 are subject to any systematics of the evolutionary models (e.g., Dupuy et al. 2009, 2014; Beatty et al. 2018; Bowler et al. 2018; Dieterich et al. 2018; Brandt et al. 2020), but ours are also impacted by those of the atmospheric models, which are likely more uncertain. Therefore, our derived ages are expected to be less accurate than the DL17 results.

The age distribution of our late-T dwarfs is shown in Figure 10, with a median of 50 Myr and 16th-to-84th percentiles spanning 10 Myr to 0.4 Gyr. This distribution is significantly younger than DL17 (with a median of 1.3 Gyr and 16th-to-84th percentiles spanning 0.8 to 3.0 Gyr) and past kinematic studies. Such a young distribution is implausible, especially since the majority of our sample are not associated to any stars or clusters with such young age.¹² The same ef-

¹² Based on the available astrometry and radial velocities of 694 T and Y dwarfs, Zhang et al. (2021) recently identified a number of T dwarfs as candidate members of nearby young moving groups, with their final

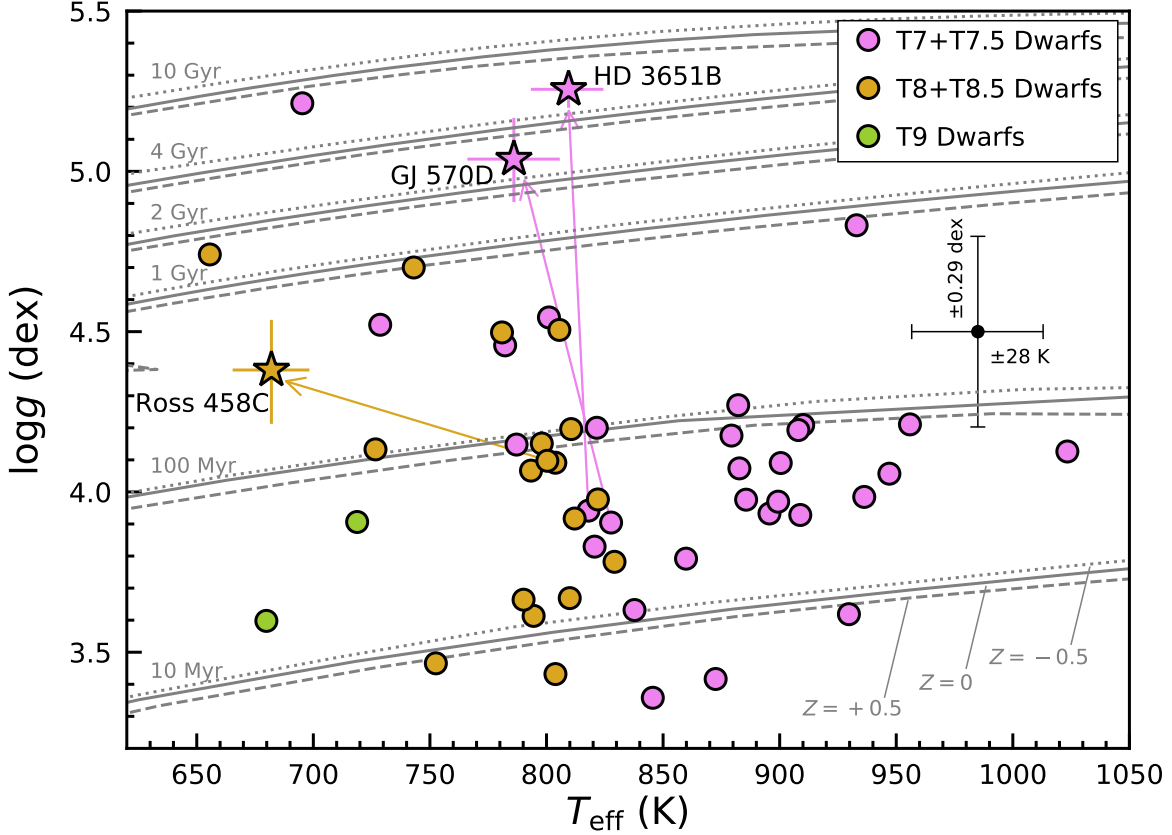


Figure 11. Spectroscopically inferred T_{eff} and $\log g$ of our late-T dwarfs (binaries removed; violet for T7 and T7.5, orange for T8 and T8.5, and green for T9) and the cloudless Sonora-Bobcat isochrones (grey lines) with different ages (10 Myr, 100 Myr, 1 Gyr, 2 Gyr, 4 Gyr, 10 Gyr) and metallicities (-0.5 dex, 0 dex, $+0.5$ dex). Typical uncertainties for our fitted T_{eff} and $\log g$ are shown as black error bars. The evolutionary model parameters of the three benchmark companions (derived from Paper I) are shown as stars and connected to their spectroscopically inferred parameters by arrows. Our forward-modeling analysis underestimates these benchmarks’ $\log g$ and Z or overestimates their T_{eff} , likely due to systematics of the cloudless Sonora-Bobcat models, and consequently, their ages derived from atmospheric model parameters are implausibly younger than the ages of their primary stars. Many of our late-T dwarfs might be in similar situations as these three companions, and thus their true ages should be systematically older.

fect is seen for the 3 benchmarks, HD 3651B, GJ 570D, and Ross 458C, whose primary stars have ages of 4.5 – 8.3 Gyr, 1.4 – 5.2 Gyr, and 0.15 – 0.8 Gyr determined by various age-dating techniques (as summarized in Paper I). In contrast, our spectroscopically inferred ages of these objects are much younger, $0.038^{+0.077}_{-0.025}$ Gyr, $0.031^{+0.052}_{-0.020}$ Gyr, and $0.077^{+0.314}_{-0.056}$ Gyr, respectively (Figure 11 and Table 5).

Our implausibly young age estimates represent another illustration that the assumptions made within our model atmospheres should be further improved. To derive more reliable ages of late-T dwarfs from near-infrared spectra, we could in-

troduce more atmospheric processes into models, e.g., clouds and/or dis-equilibrium chemistry (see Section 6).

5.3. Effective Temperature vs. Spectral Type

Now we study the relation between the atmospheric-based, spectroscopically inferred T_{eff} and the spectral types of late-T dwarfs. First, we briefly review empirical T_{eff} –SpT relations that have been established using evolutionary models. Similar to earlier work by Leggett et al. (2002), Golimowski et al. (2004) compiled parallaxes and infrared spectrophotometry of 51 M1–T9 dwarfs. They measured bolometric luminosities from the objects’ spectral energy distributions (SEDs) and then converted these into T_{eff} assuming an age range of 0.1 – 10 Gyr and using evolutionary models (Burrows et al. 1997; Baraffe et al. 1998; Chabrier et al. 2000). Looper et al. (2008) and Stephens et al. (2009) later modified this sample by removing binaries and/or adding companions discovered since the Golimowski et al. (2004) work and obtained

membership assessment awaiting radial velocity measurements. Only 3 objects in our sample here are candidate young moving group members: WISE J024124.73 – 365328.0 (T7; Argus; 40 – 50 Myr, Zuckerman 2019), 2MASS 1553 + 1532 (T7; Carina-Near; 200 ± 50 Myr, Zuckerman et al. 2006), and WISEPC J225540.74 – 311841.8 (T8; β Pictoris; 24 ± 3 Myr, Bell et al. 2015).

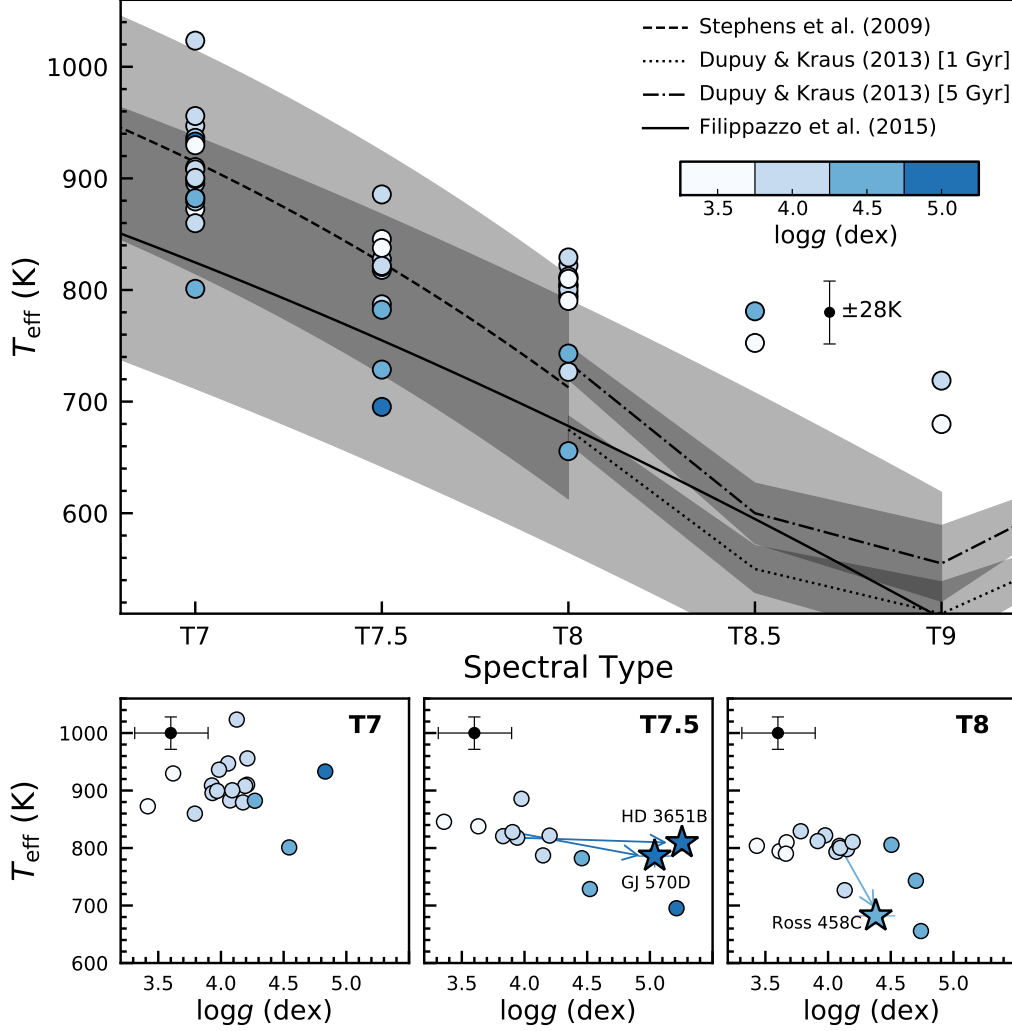


Figure 12. Top plot: T_{eff} –SpT relation of our late-T dwarfs (binaries removed), with spectroscopically inferred $\log g$ encoded with blue shading. The median T_{eff} uncertainty is shown as the black error bar. We overlay evolutionary-based effective temperature scales from Stephens et al. (2009; dashed) and Filippazzo et al. (2015; solid). We also plot the Dupuy & Kraus (2013) T_{eff} –SpT relations corresponding to assumed ages of 1 Gyr (dotted) and 5 Gyr (dash-dotted). The gray shadow shows the rms of each empirical T_{eff} –SpT relation. Bottom plots: T_{eff} of our T7, T7.5, and T8 dwarfs as a function of $\log g$. Median T_{eff} and $\log g$ uncertainties are shown as black error bars. The evolutionary model parameters of three benchmarks (derived from Paper I) are shown as stars and connected to their spectroscopically inferred parameters by arrows.

tighter temperature scales as a function of spectral types. Focusing on the coolest substellar objects, Dupuy & Kraus (2013) computed L_{bol} for 21 T8–Y0 field dwarfs using parallaxes, broadband photometry, and bolometric corrections, and then derived T_{eff} using the Baraffe et al. (2003b) evolutionary models with age assumptions of 1 Gyr and 5 Gyr. The most recent T_{eff} –SpT relation has been derived by Filippazzo et al. (2015) using a much larger sample of nearly 200 M6–T9 dwarfs. They measured L_{bol} based on a homogeneous SED analysis and then estimated T_{eff} using the Saumon & Marley (2008) hybrid models with an assumed age of 0.5–10 Gyr for most objects and narrower ranges for association members and companions. The Filippazzo et al.

(2015) temperature scale of field dwarfs is consistent with results of Stephens et al. (2009) and Dupuy & Kraus (2013).

Figures 12 and 13 compare our atmospheric-based T_{eff} of T7–T9 dwarfs to the evolutionary-based temperature scales from Stephens et al. (2009), Dupuy & Kraus (2013), and Filippazzo et al. (2015). At a given spectral type, our spectroscopically inferred T_{eff} show a spread of ± 100 K, similar to the empirical relations. Our results are consistent with empirical ones for T7 and T7.5 dwarfs, but appear 50–200 K hotter at later types, likely because our derived T_{eff} for T8–T9 dwarfs are less reliable than those of T7 dwarfs. As found in Paper I and summarized in Section 3.2 in this work, our spectral fits of Ross 458C (T8) predict ≈ 120 K higher T_{eff}

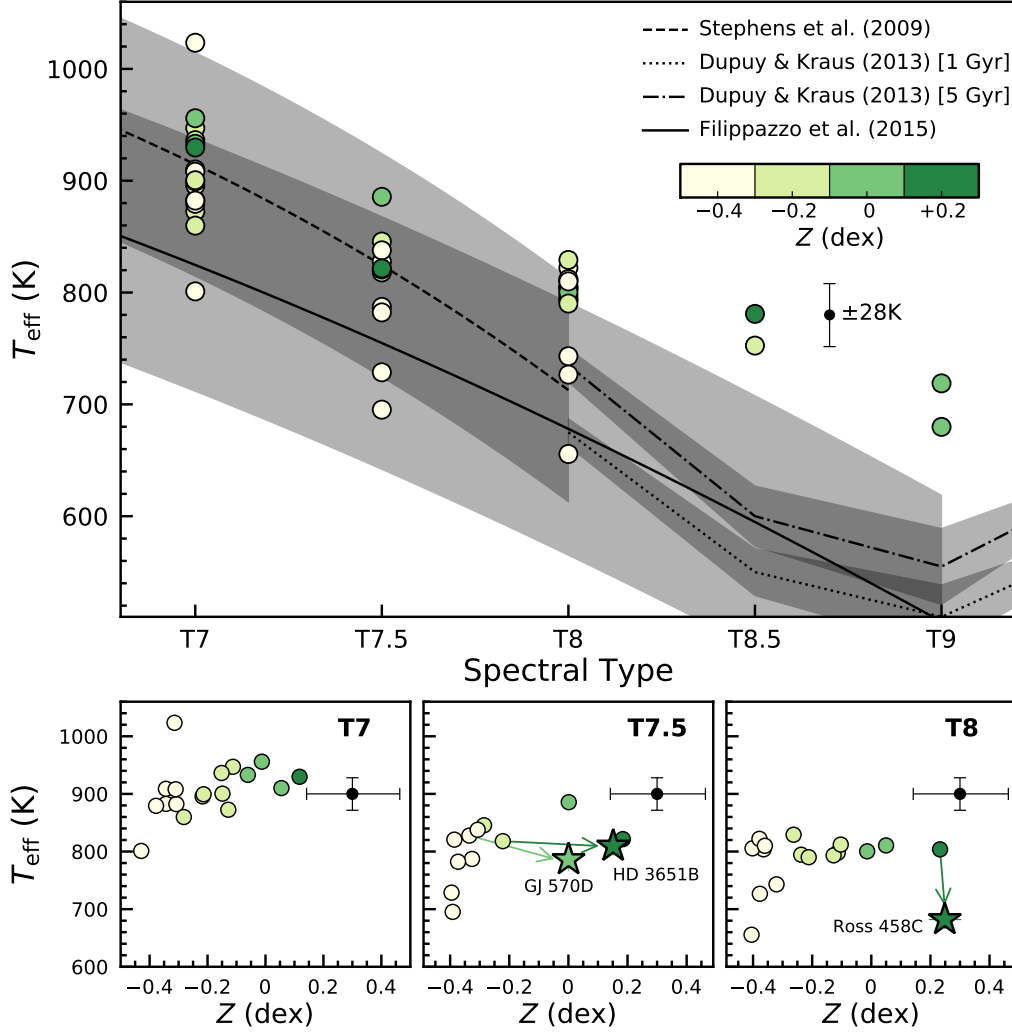


Figure 13. The effect of metallicity on the T_{eff} –SpT relation of our late-T dwarfs (binaries removed), with the same format as Figure 12. Spectroscopically inferred Z are encoded with green shading. Bottom plots show the objects’ T_{eff} as a function of Z .

than evolutionary model analysis, while the two T7.5 benchmarks (HD 3651B and GJ 570D) have no such significant discrepancy.

Figure 12 explores whether the derived T_{eff} –SpT relation of our sample is gravity-dependent. We focus on the T7, T7.5, and T8 objects in our sample, since we have only four T8.5 and T9 dwarfs. Studying the objects’ T_{eff} as a function of $\log g$, we find lower-gravity T7.5 and T8 dwarfs have on-average hotter effective temperatures at a given spectral type. Intriguingly, this phenomenon is not found in earlier T dwarfs. Based on a sample of 25 young (≤ 300 Myr) and old (> 300 Myr) T0–T6 benchmarks, Zhang et al. (2020a) demonstrated that lower-gravity objects tend to have ≈ 100 K cooler T_{eff} than their high-gravity counterparts at same spectral types (also see Metchev & Hillenbrand 2006; Filippazzo et al. 2015; Faherty et al. 2016; Liu et al. 2016), which is opposite of the $T_{\text{eff}} - \log g$ relation for late-T dwarfs seen in

Figure 12. For T7–T9 spectral types, there is only one low-gravity benchmark with direct spectroscopy, i.e., Ross 458C, for which our evolutionary model analysis derives $T_{\text{eff}} = 682^{+16}_{-17}$ K (Paper I). This temperature is consistent with those of higher-gravity field T8 dwarfs (678 ± 113 K based on the T_{eff} –SpT relation of Filippazzo et al. 2015) and thus not in accord with the $T_{\text{eff}} - \log g$ relation from our results, which predicts its T_{eff} to be much hotter. More discoveries of such young, late-type benchmarks will help investigate the gravity dependence of late-T dwarfs’ effective temperatures.

In fact, the possible relation between the fitted T_{eff} and $\log g$ of our sample is likely because these parameters are over- and/or under-estimated. Some of the T7.5 dwarfs in our sample might be similar to HD 3651B and GJ 570D, whose fitted T_{eff} are reliable but $\log g$ are underestimated by ≈ 1.2 dex when compared to the more robust evolutionary model predictions. Also, some of the T8 dwarfs might be similar to

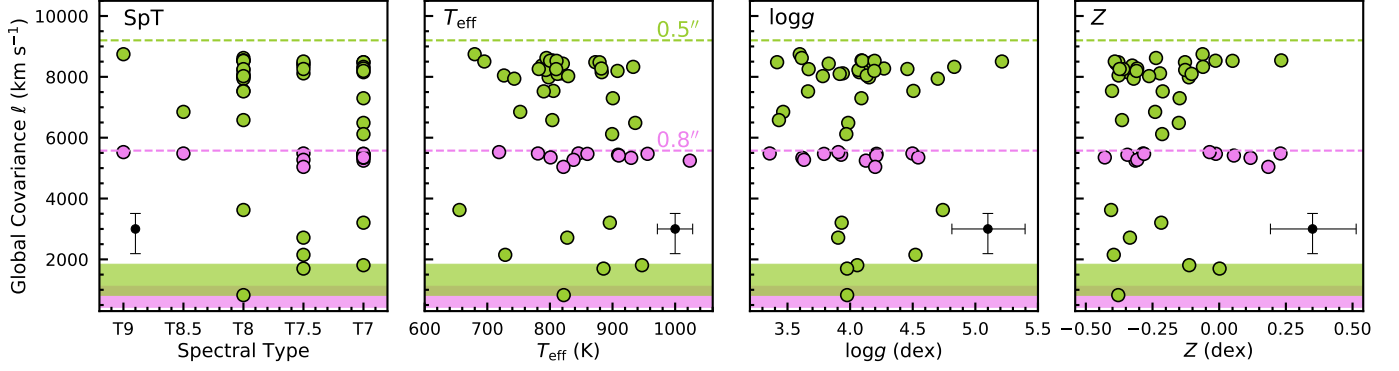


Figure 14. The covariance hyper-parameter ℓ of our 49 late-T dwarfs (binaries removed) as a function of spectral type and fitted $\{T_{\text{eff}}, \log g, Z\}$, with median uncertainties shown as black error bars. We use green and violet for ℓ inferred from spectra taken from the 0.5'' and 0.8'' slits, respectively. For a given slit, we use the shaded area to mark the ℓ range expected by the instrumental line spread function (820 – 1840 km s⁻¹ for the 0.5'' slit and 425 – 1115 km s⁻¹ for the 0.8'' slit) and use dashed lines to mark upper boundaries of our adopted ℓ prior.

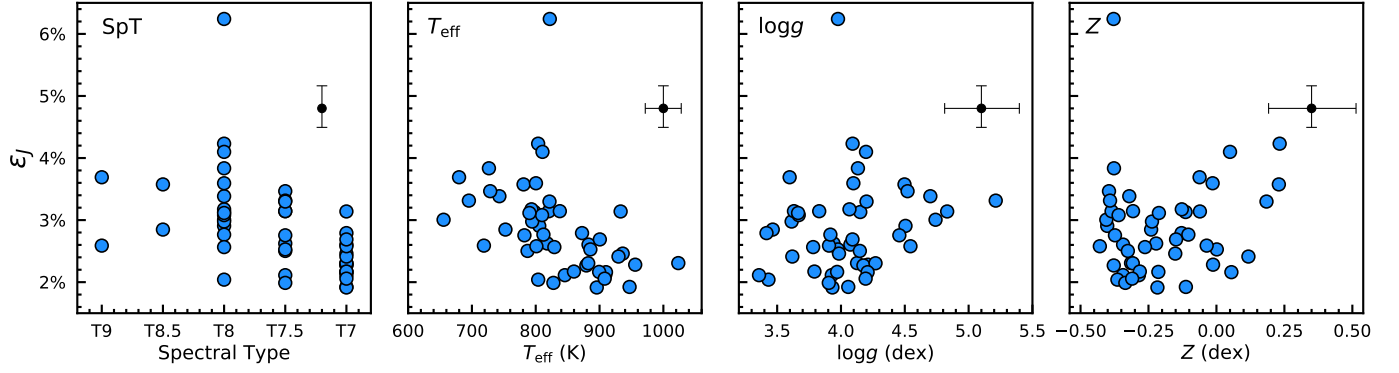


Figure 15. The ϵ_J values of our 49 late-T dwarfs (binaries removed) computed from their covariance hyper-parameters a_G and a_N and the observed spectra (Section 6.1). The ϵ_J describes the fraction that model uncertainties (i.e., systematic flux difference between the cloudless Sonora-Bobcat models and late-T dwarf spectra) comprise of the objects' observed peak J -band fluxes. Median uncertainties are shown as black error bars. The object with the highest ϵ_J among our sample is WISE 1322 – 2340. The ϵ_J values, namely model systematics, tend to become larger at later spectral types, cooler spectroscopically inferred T_{eff} , and possibly higher $\log g$ and Z .

Ross 458C, whose fitted $\log g$ is reliable but T_{eff} is overestimated by ≈ 120 K. Correcting their inaccurate atmospheric-based parameters would be the equivalent of shifting their $\log g$ toward higher values and/or their T_{eff} toward cooler values, which could alter the $T_{\text{eff}} - \log g$ relation in Figure 12.

Figure 13 explores whether the derived $T_{\text{eff}} - \text{SpT}$ relation of our sample is metallicity-dependent. Studying the objects' T_{eff} as a function of Z , we find lower-metallicity T7, T7.5, and T8 dwarfs have on-average cooler effective temperatures at a given spectral type. The validity of this metallicity dependence is uncertain. For the two late-T subdwarf benchmarks, BD +01° 2920B (T8; $Z = -0.38 \pm 0.06$ dex by Valenti & Fischer 2005) and Wolf 1130C (T8; $Z = -0.70 \pm 0.12$ by Mace et al. 2018), previous work found their effective temperatures are similar to those of the field population, which has on average higher metallicities (Pinfield et al. 2012; Mace et al. 2013b), and thus not in accord with the $T_{\text{eff}} - Z$ relation

seen in our results. Similar to the aforementioned $T_{\text{eff}} - \log g$ trend, this $T_{\text{eff}} - Z$ relation for late-T dwarfs in Figure 13 might be related to modeling systematics. To further validate this potential metallicity dependence for late-T dwarfs, we need models with modified physical assumptions and more benchmarks over a wide range of metallicities.

6. DISCUSSION OF THE CLOUDLESS SONORA-BOBCAT MODELS

Our forward-modeling analysis shows the cloudless Sonora-Bobcat models match the general spectroscopic appearance of late-T dwarfs, but the fitted physical parameters can be under- or over-estimated, suggesting the models' assumptions might be inadequate to fully interpret late-T dwarf spectra (Section 5). Here we explore specific shortcomings, by focusing on 49 late-T dwarfs in our sample, as the other 6 objects are resolved or likely binaries (Section 4).

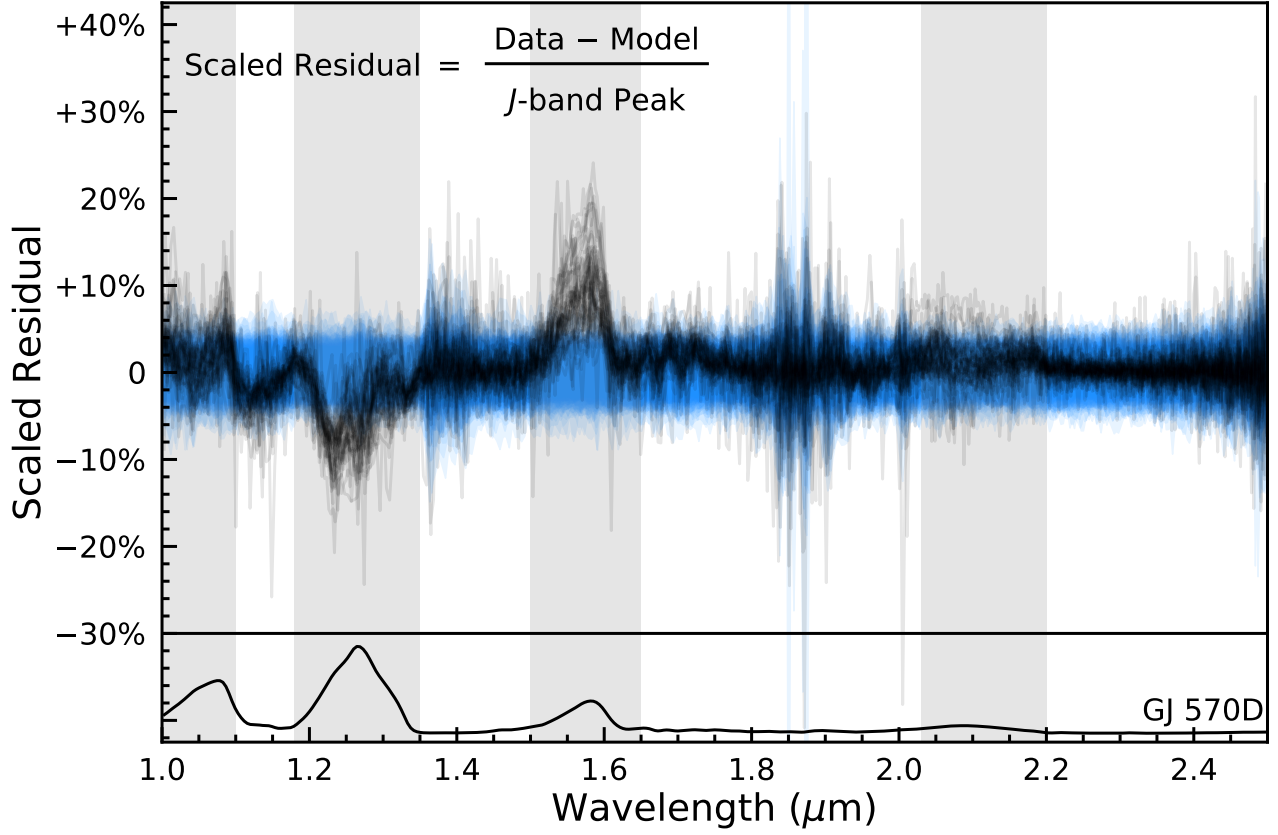


Figure 16. Stacked spectral-fitting residuals of our 49 late-T dwarfs (binaries removed), with each residual (i.e., data – model; black) normalized by the object’s observed peak J -band flux. The 1σ and 2σ dispersions of 5×10^4 draws from Starfish’s full covariance matrix are shown as deep and light blue shadows, respectively, and they are normalized by the same peak flux for each object. The resulting stack has a tight distribution at each wavelength and exhibits prominent features in $YJHK$ bands (grey shadow, with specific wavelength ranges shown in Equation 2). The spectrum of GJ 570D is plotted at the bottom as a reference.

6.1. Starfish Covariance Hyper-Parameters

As discussed in Paper I, we can assess the systematic difference between data and models using the fitted covariance hyper-parameters $\{a_N, a_G, \ell\}$ of our late-T dwarfs. The parameter ℓ characterizes the autocorrelation wavelength of data–model residuals, caused by (1) the oversampled instrumental line spread function (LSF), and (2) the systematics of model assumptions. If the correlated residuals of an object are solely due to the instrumental LSF, then its fitted ℓ should be within $[820, 1840]$ km s $^{-1}$ and $[425, 1115]$ km s $^{-1}$ for spectra taken by the SpeX 0.5'' and 0.8'' slits, respectively (see Appendix of Paper I). However, the spectroscopically inferred ℓ of almost all our late-T dwarfs are significantly higher than the range expected from the LSF, suggesting the correlated residuals of our sample do not arise from the instrument’s spectral resolution but rather shortcomings of the model predictions (Figure 14). Figure 14 also shows the inferred ℓ of our sample has no correlations with the objects’ spectral types or fitted $\{T_{\text{eff}}, \log g, Z\}$.

Given that the modeling systematics dominate the correlated residuals, we can use the other two hyper-parameters (a_N and a_G) to quantify the modeling systematics. Specifically, we can compute $\sqrt{a_G/a_N}$ and regard it as an equivalent flux that describes the average “model uncertainties” (as opposed to measurement uncertainties). Normalizing this value by an object’s peak J -band flux (Equation 7 of Paper I), we define the normalized model uncertainty as $\epsilon_J = \sqrt{a_G/a_N}/\max(f_{\text{obs},J})$, with higher values suggesting more significant data-model discrepancies.

We summarize the derived ϵ_J of our sample in Table 5 and find the systematic difference between the cloudless Sonora-Bobcat models and late-T dwarf spectra is on average $\approx 2\% - 4\%$ of the observed peak J -band fluxes over $1.0 - 2.5 \mu\text{m}$ wavelengths¹³, equivalent to a S/N (the ratio of signal to model uncertainty) of 50 – 25. This is in ac-

¹³ We note these values describe an average systematic difference between observed spectra and Sonora-Bobcat models over the $1.0 - 2.5 \mu\text{m}$ range. As shown in Figure 16, such systematic difference can be as high

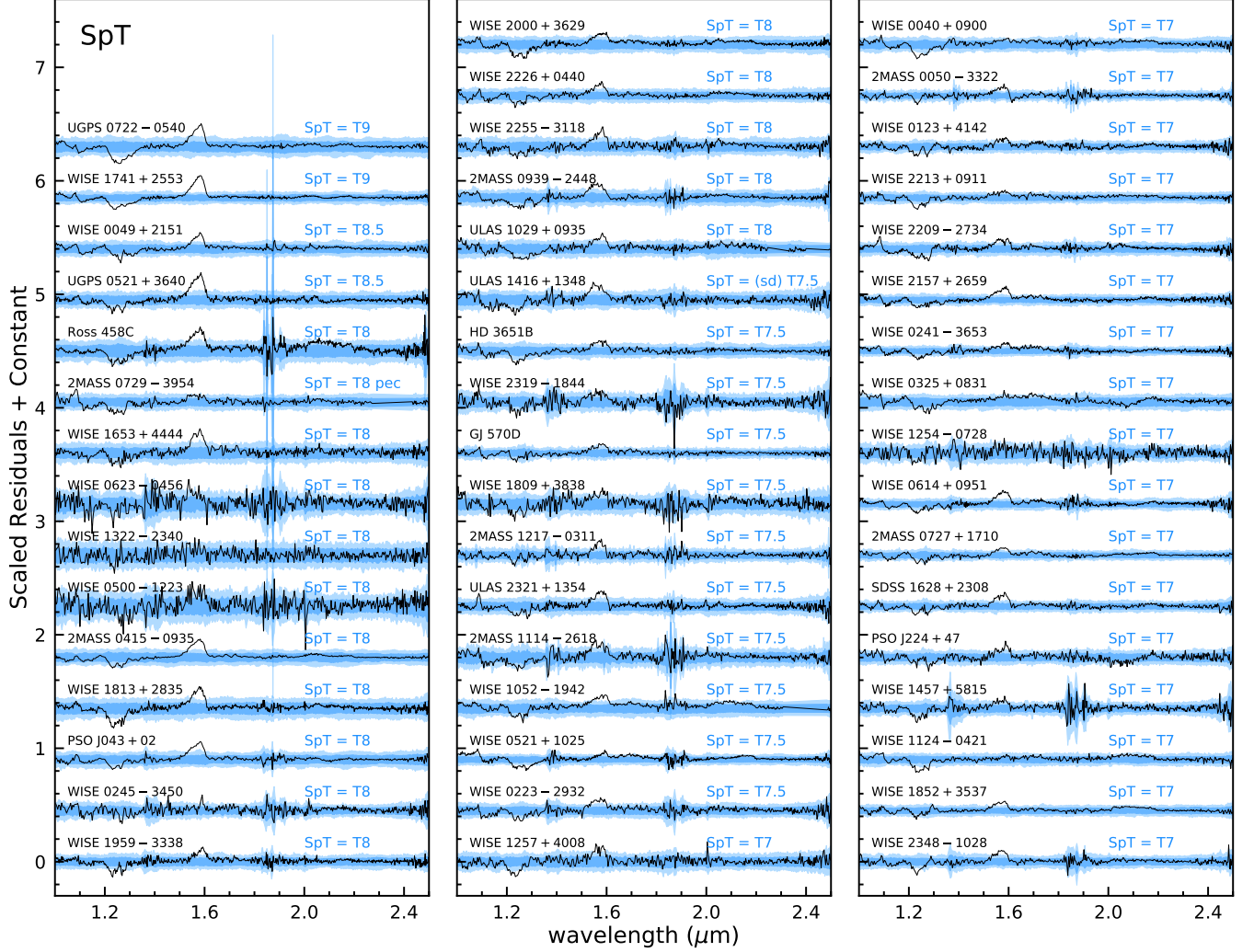


Figure 17. Residuals of our 49 late-T dwarfs (binaries removed) shown in order of spectral types, and spectroscopically inferred T_{eff} , $\log g$, and Z . We use each object’s observed peak J -band flux to normalize its residual (black), as well as 1σ and 2σ dispersions of 5×10^4 draws from Starfish’s full covariance matrix (blue shadows). The J -band and H -band residuals tend to be more significant with later spectral types and cooler effective temperatures. The H -band residual also becomes more prominent with increasing metallicities.

cord with our conclusion in Paper I based on the three late-T benchmarks, which are also included in the analysis here. This result implies that model uncertainties exceed measurement uncertainties when fitting the cloudless Sonora-Bobcat models to late-T dwarf spectra with $S/N \gtrsim 50$ per pixel in J band. As a consequence, increasing the S/N of observations does not necessarily improve the precision of the fitted physical parameters, as also seen in Figure 4 and discussed in Section 3.2.1.

Figure 15 plots our objects’ ϵ_J as a function of their spectral types and fitted physical parameters. We find the data-model difference tends to be larger toward later spec-

tral types, cooler effective temperatures, and possibly higher $\log g$ and Z . These trends indicate some important atmospheric processes are likely missing in the model assumptions, which we discuss in the following section.

6.2. Spectral-Fitting Residuals

Missing physical processes in model assumptions should leave footprints in our objects’ spectral-fitting residuals. Thanks to our large sample of late-T dwarfs, we can investigate these residuals and assess how models deviate from the observations as a function of wavelength and atmospheric parameters. In Figure 16, we normalize the fitting residuals for each object by its observed peak J -band flux and then stack them together. The resulting stack has a tight distri-

as 10% – 20% of the objects’ peak J -band fluxes over narrow wavelength ranges in J and H bands.

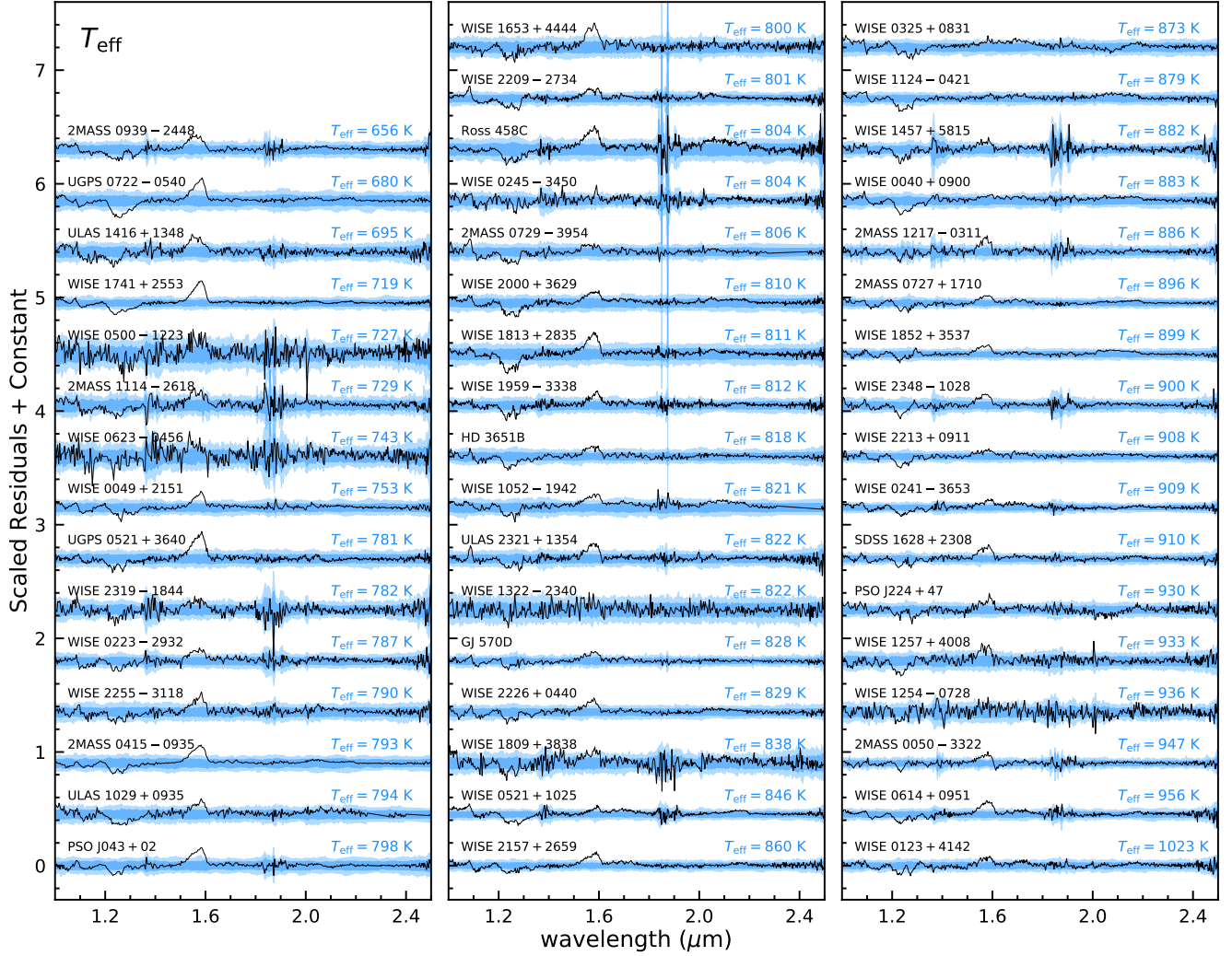


Figure 17. Continued

bution as a function of wavelength and exhibits prominent features in *YJHK* bands.

In order to study how the residuals are correlated with atmospheric properties, we plot residuals sorted by the objects' spectral types and fitted $\{T_{\text{eff}}, \log g, Z\}$ in Figure 17. We further define the following quantities q_Y , q_J , q_H , and q_K to evaluate the data-model difference in *YJHK* bands for each object (Table 5),

$$q(\lambda\lambda) = 1 - \frac{\int_{\lambda\lambda} f_{\text{model},\lambda} d\lambda}{\int_{\lambda\lambda} f_{\text{obs},\lambda} d\lambda}$$

such that

$$\begin{aligned} q_Y &\equiv q([1.00\mu\text{m}, 1.10\mu\text{m}]) \\ q_J &\equiv q([1.18\mu\text{m}, 1.35\mu\text{m}]) \\ q_H &\equiv q([1.50\mu\text{m}, 1.65\mu\text{m}]) \\ q_K &\equiv q([2.03\mu\text{m}, 2.20\mu\text{m}]) \end{aligned} \quad (2)$$

Here $\lambda\lambda$ corresponds to the wavelength range of prominent *YJHK*-band features seen in Figure 16 and does not follow the standard definition of the filters. In addition, $f_{\text{model},\lambda}$ and $f_{\text{obs},\lambda}$ are the fitted model and the observed spectrum of the object, respectively. The sign of q indicates whether the models under-predict (positive) or over-predict (negative) the data, with larger absolute values of q indicating larger data-model discrepancies. By definition, model atmospheres that perfectly match the data will have $q = 0$ for all wavelength ranges.

In *Y* band ($\approx 1.0 - 1.1 \mu\text{m}$), our fitted models slightly under-predict the spectra of most late-T dwarfs (Figure 16 and 17). This is likely related to the potassium resonance doublet at $0.77 \mu\text{m}$ (Allard et al. 1999; Burrows et al. 2000), whose pressure-broadened wings can extend to *Y* and *J* bands. The *K* line profile depends on the treatment of collisions between H_2 molecules and *K* atoms (e.g., Baudino et al. 2017; Phillips et al. 2020). The cloudless Sonora-Bobcat

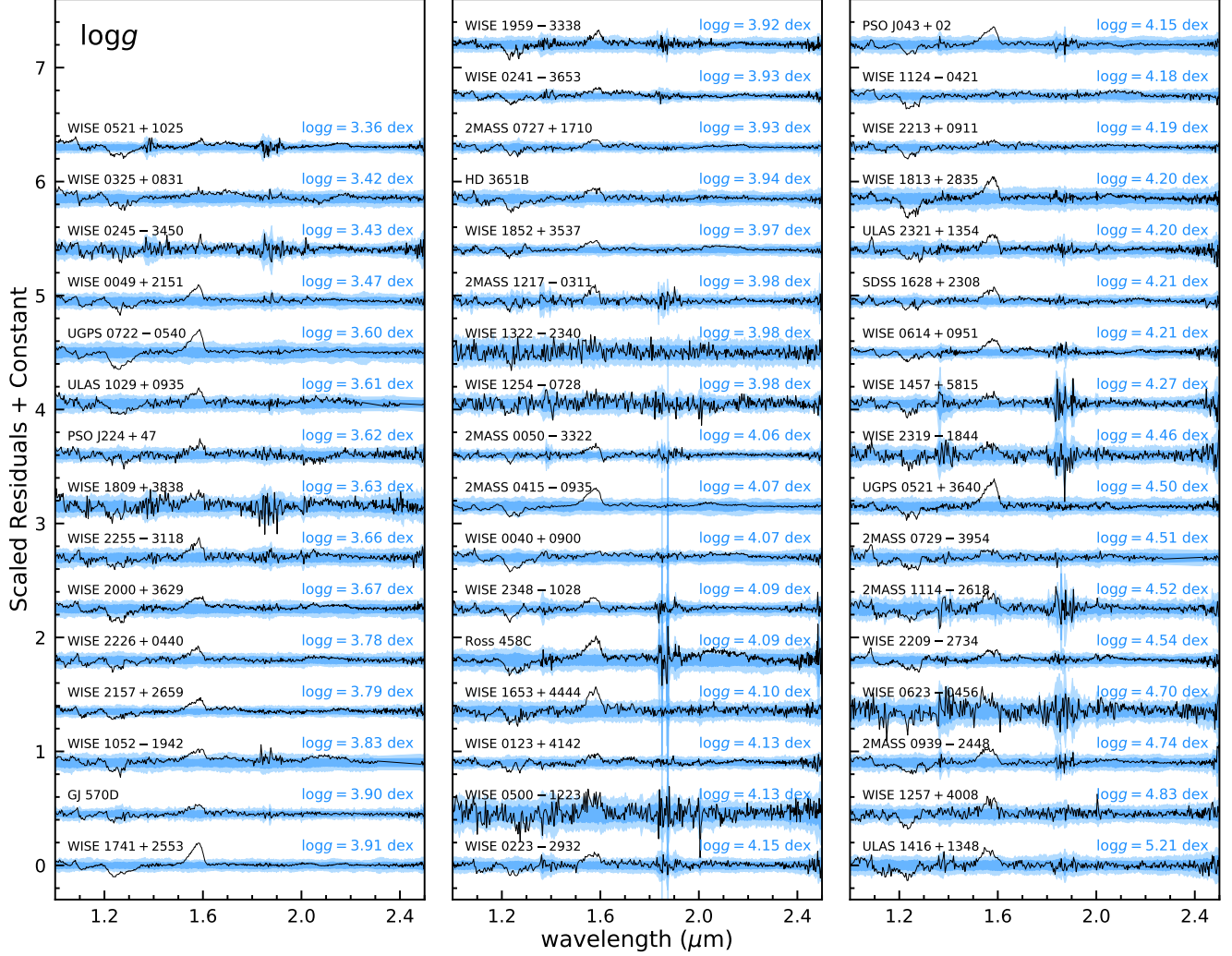


Figure 17. Continued

models adopt the K line shape theory by [Allard et al. \(2007\)](#). [Allard et al. \(2016\)](#) have improved calculations of the K–H₂ potential, which might predict more accurate shapes for the K I doublet and thereby the Y-band fluxes (e.g., [Phillips et al. 2020](#)).

In *J* band ($\approx 1.18 - 1.35 \mu\text{m}$), our fitted models over-predict spectra of all late-T dwarfs, and we find q_J is correlated with spectral type and T_{eff} (Figure 18), as the *J*-band residuals increase for later-type and cooler objects. This residual plausibly arises from clouds (e.g., [Morley et al. 2012](#)), given that fluxes at near-infrared spectral peaks are emitted from the deep atmosphere and thus more sensitive to cloud opacity. Including clouds into Sonora-Bobcat models might therefore produce spectra that better match the observations. Also, with lower effective temperatures, condensates of various species are expected to form (e.g., Na₂S, KCl, MnS, ZnS; [Lodders 1999](#); [Morley et al. 2012](#)), leading to a larger *J*-band discrepancy between data and the cloud-

less models. This is consistent with the $q_J - T_{\text{eff}}$ correlation in Figure 18.

Alternatively, the over-predicted *J*-band flux of the cloudless Sonora-Bobcat models might be related to the assumption that the deep temperature gradient in convective regions lies along an adiabat. As demonstrated by [Tremblin et al. \(2015, 2019\)](#), cloudless dis-equilibrium models with (1) atmospheric mixing (described by the eddy diffusion coefficients K_{zz}) and (2) reduced vertical temperature gradient (as compared to the adiabatic lapse rate) are more appropriate for spectra of T/Y dwarfs than cloudless, chemical-equilibrium models. While these models can explain the *J*-band residuals of our sample, they will need to explain the q_J –SpT and $q_J - T_{\text{eff}}$ correlations as seen in Figure 18. One implication from these correlations is that the thermo-chemical instability in the [Tremblin et al. \(2015\)](#) models should be more significant with later spectral types and cooler T_{eff} for late-T dwarfs. To examine this hypothesis, further investigation is needed to

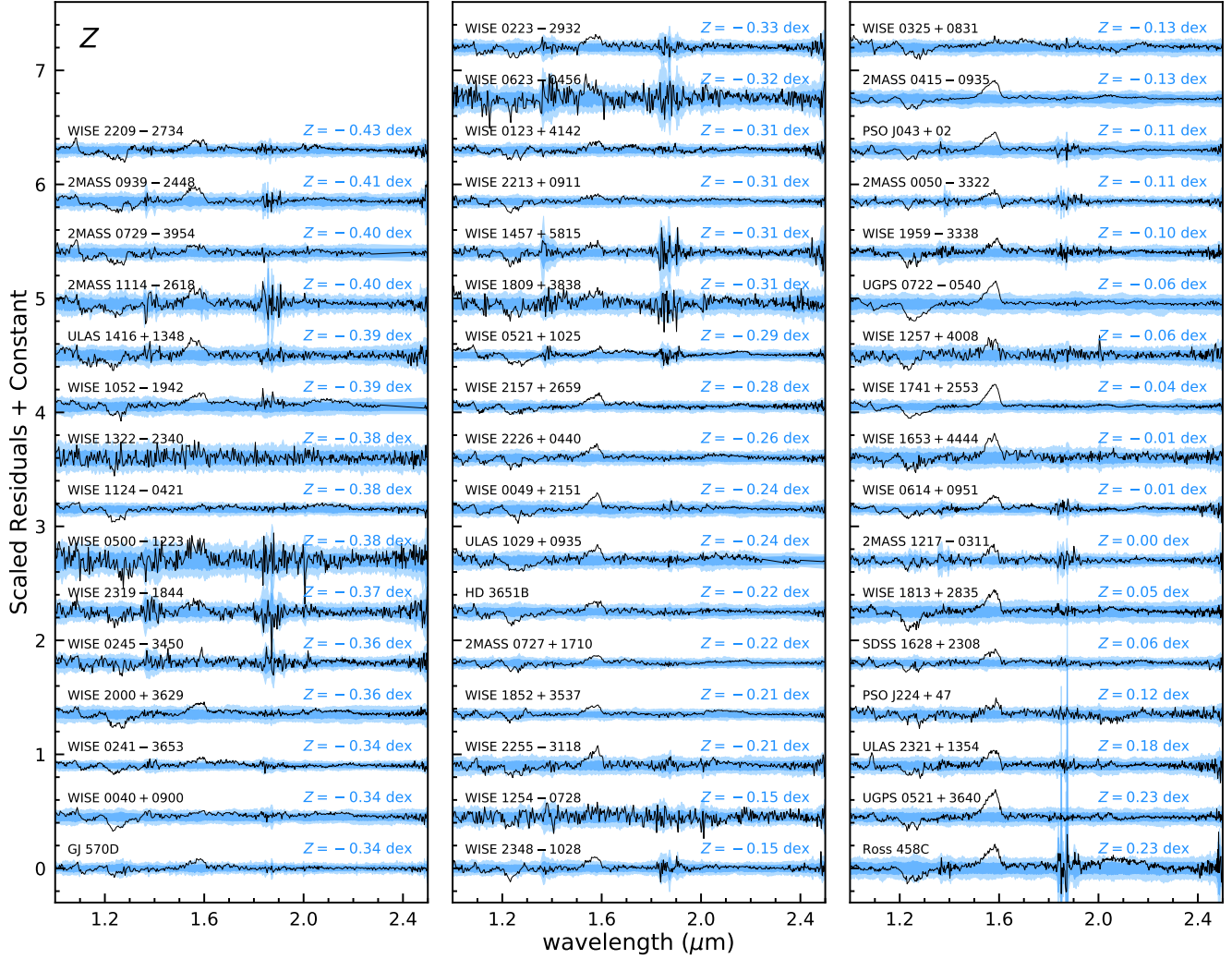


Figure 17. Continued

study such instability in brown dwarf atmospheres as a function of physical properties.

In H band ($\approx 1.50 - 1.65 \mu\text{m}$), our fitted models under-predict spectra of all late-T dwarfs, and we find the residuals (q_H) become more significant with later spectral types, cooler effective temperatures, and higher metallicities (Figures 18). These can be related to the dis-equilibrium abundance of NH_3 , which would be less than the amount assumed by the equilibrium chemistry within the cloudless Sonora-Bobcat models and thus lead to weaker absorption in the blue wing of H band (Saumon et al. 2006, 2012; Cushing et al. 2011; Zahnle & Marley 2014). However, the NH_3 cross-section is peaked around $1.5 \mu\text{m}$ (or wavenumbers of $6600 - 6700 \text{ cm}^{-1}$; e.g., Yurchenko et al. 2011; Coles et al. 2019), slightly offset from the H -band residuals of our late-T dwarfs which are peaked near $1.58 \mu\text{m}$. Alternatively, the under-predicted H -band spectra could well be a consequence of the spectral-fitting procedure responding to the

over-predicted J -band flux by choosing models that under-predict the H -band flux. Studying our late-T dwarf spectra using (1) cloudless models with dis-equilibrium chemistry or (2) cloudy models with equilibrium chemistry will help better understand this H -band residual.

In K band ($\approx 2.03 - 2.20 \mu\text{m}$), our fitted models only slightly under-predict spectra of most late-T dwarfs. Similar to J band, such K -band residuals may arise from clouds and/or reductions in the vertical temperature gradient. As shown by Morley et al. (2012; their Figure 11) and Tremblin et al. (2015; their Figure 1), either of these two processes can reduce fluxes in YJ bands and increase the flux in K band.

7. SUMMARY AND FUTURE WORK

We have conducted a forward-modeling analysis for 55 late-T (T7–T9) dwarfs using low-resolution ($R \approx 50 - 250$) near-infrared ($1.0 - 2.5 \mu\text{m}$) spectra and state-of-art, cloudless Sonora-Bobcat model atmospheres with $T_{\text{eff}} = 600 -$

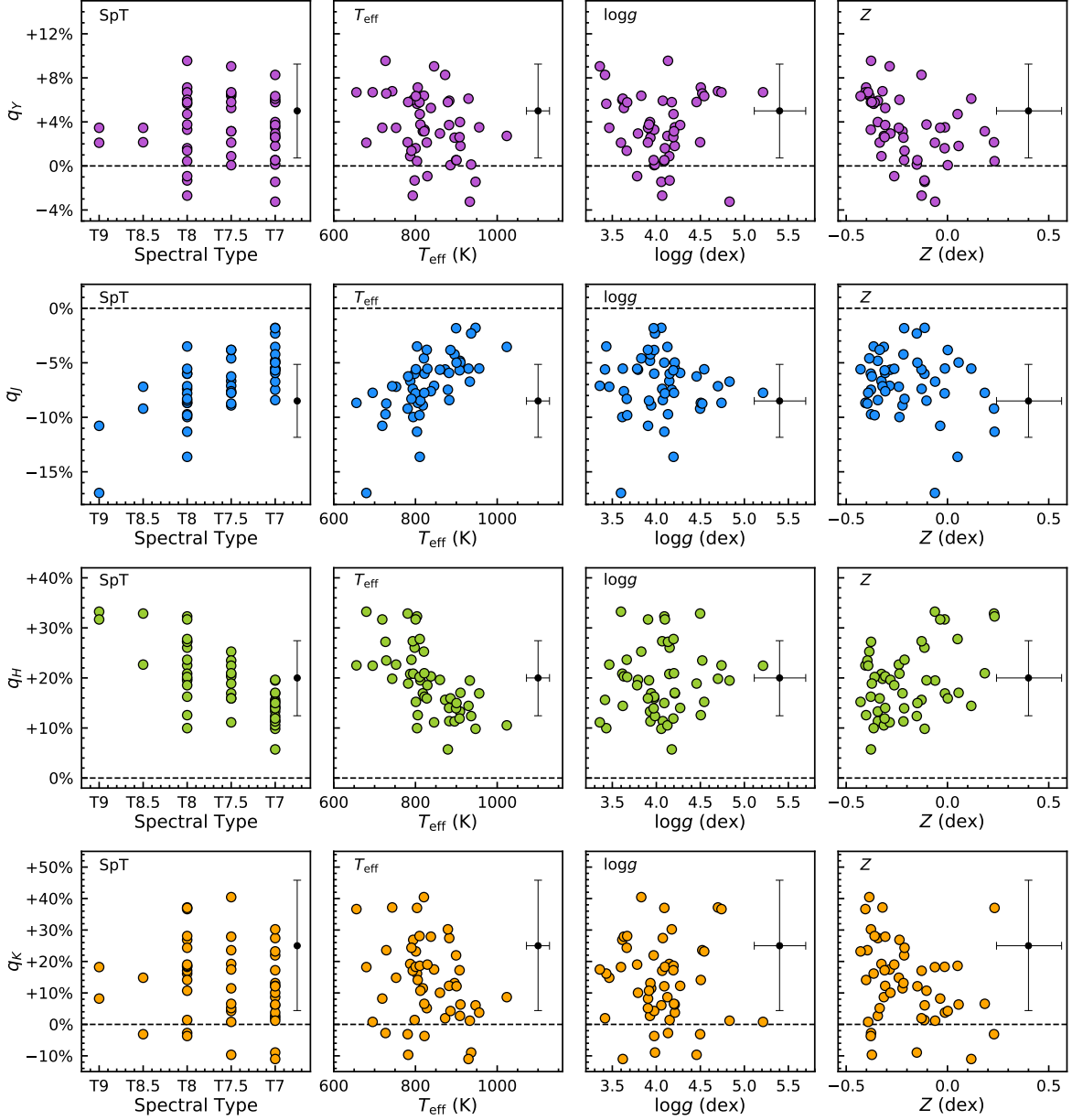


Figure 18. The q_Y (purple), q_J (blue), q_H (green), and q_K (orange) of our 49 late-T dwarfs (binaries removed) as a function of spectral type and atmospheric $\{T_{\text{eff}}, \log g, Z\}$, with median uncertainties shown by black error bars. The q values (Equation 2) quantify the fitted residuals of the object in $YJHK$ bands. The sign of q indicates whether the models under-predict (positive) or over-predict (negative) the observed spectra over a given band pass, with larger absolute values of q indicating larger data-model discrepancies. By definition, perfect models should have $q = 0$ at all wavelengths (dashed horizontal lines).

1200 K, $\log g = 3.25 - 5.5$ dex, and $Z = \{-0.5, 0, +0.5\}$ dex. Our sample contains 90% of the nearby T7–T9 population with distances ≤ 25 pc, J -band magnitudes ≤ 17.5 mag, and declinations from -40° to $+70^\circ$. Our work is the largest analysis of brown dwarf spectra using multi-metallicity models to date, as well as the most systematic test of any set of ultracool model atmospheres. Our forward-modeling framework was constructed and validated in Paper I, which uses the Bayesian inference tool Starfish (Czekala et al. 2015). Com-

pared to traditional forward-modeling studies, our analysis produces more realistic error estimates since we account for uncertainties from model interpolation and correlated residuals due to instrumental effects and systematics of model assumptions.

We have inferred effective temperatures (T_{eff}), surface gravities ($\log g$), metallicities (Z), radii (R), masses (M), and bolometric luminosities (L_{bol}) for our late-T dwarfs, with the typical resulting $\{T_{\text{eff}}, \log g, Z\}$ uncertainties being

$\approx 1/3 - 1/2$ of the Sonora-Bobcat model grid spacing. We found no difference in the precision of these physical parameters for spectra with two different spectral resolutions ($R \approx 80 - 250$ and $50 - 160$). Combining the resulting parameter posteriors of our entire sample, we found some fitted parameters are correlated, including T_{eff} and R , R and M , and $\log g$ and Z . Correlations within the first two pairs are expected by the Stephen-Boltzmann law and the calculation of mass from spectroscopic parameters, respectively. The third correlation illustrates that $\log g$ and Z are degenerate in the cloudless Sonora-Bobcat models, and we provide a quantification of this $\log g - Z$ dependence. For late-T dwarfs, the degeneracy acts such that an increase in Z , combined with a $3.4\times$ larger increase in $\log g$, results in a spectrum that has similar fitted atmospheric parameters. Consequently, using solar-metallicity model atmospheres to study late-T dwarfs whose metallicities are in fact non-solar will bias the inferred $\log g$, but likely not other parameters.

By virtue of having a large sample of spectra within a focused spectral type range (as opposed to a smaller sample of objects over a wide spectral type range), we can study population properties of T7–T9 dwarfs to provide useful diagnostics about our set of grid models, which assume cloudless and chemical-equilibrium atmospheres:

1. The spectroscopically inferred metallicities of our entire sample and a volume-limited subset within 25 pc are $0.3 - 0.4$ dex lower than those of nearby FGKM stars (e.g., [Hinkel et al. 2014](#)). This significant discrepancy is unlikely to be a real difference between the sub-stellar and stellar populations, but rather because our fitted metallicities are underestimated, which is also seen from our Paper I analysis of the late-T benchmarks HD 3651B and GJ 570D.
2. The inferred ages of our sample, based on their fitted $\{T_{\text{eff}}, \log g, Z\}$ and evolutionary models, have a median of 50 Myr and a 1σ confidence interval of 10 Myr–0.4 Gyr. These values are implausibly younger than the robustly determined ages of nearby M8–T5 binaries ([Dupuy & Liu 2017](#)) and thus are likely underestimated.
3. The spectroscopically inferred effective temperatures of our sample show a similar spread (± 100 K) at a given spectral type as compared to empirical effective temperature scales, but our T_{eff} appear systematically hotter (by $50 - 200$ K) for $\geq T8$ dwarfs. Also, our derived $T_{\text{eff}} - \text{SpT}$ relation for late-T dwarfs is weakly correlated with fitted $\log g$ and Z , as objects with either lower $\log g$ or higher Z have on average hotter T_{eff} at a given spectral type. The possible gravity and metallicity dependence seen in this work might be caused by the over- and/or under-estimated physical parameters from spectral fitting, but it should be further validated

using more late-T benchmarks with diverse ages and metallicities.

4. The spectroscopically inferred masses of our sample are unphysically small (mostly $1 - 8 M_{\text{Jup}}$), due to the underestimate of their fitted $\log g$ and/or R .

Using the hyper-parameters from our spectral-fitting results, we quantified that the systematic difference between the observed late-T dwarf spectra and the Sonora-Bobcat models is on average $\approx 2\% - 4\%$ of the objects' peak J -band fluxes over the $1.0 - 2.5 \mu\text{m}$ range (as high as $10 - 20\%$ of the objects' peak J -band fluxes over narrow wavelength ranges in J and H bands), equivalent to a S/N of $50 - 25$. Therefore, model uncertainties exceed measurement uncertainties when fitting the Sonora-Bobcat models to late-T dwarf spectra with S/N higher than these values. This can also explain why the fitted parameter precision of our sample does not improve with increasing S/N once it is above ≈ 50 per pixel in J band.

In order to investigate how to improve model assumptions, we stacked the spectral-fitting residuals of our entire sample and investigated these as a function of wavelength and the inferred atmospheric properties. We found common, prominent residual features in $YJHK$ bands:

1. In Y band, the cloudless Sonora-Bobcat models tend to under-predict the observed fluxes, which is likely related to the potassium line profiles. Further improvements of the alkali opacities might help reduce this residual (e.g., [Allard et al. 2016](#)).
2. In J band, the cloudless Sonora-Bobcat models tend to over-predict the observed fluxes by an amount which is larger for later spectral types and cooler T_{eff} . This effect is likely caused by missing opacity from clouds (e.g., [Morley et al. 2012](#)) or the model assumption that the deep temperature gradient in convective regions lies along an adiabat (e.g., [Tremblin et al. 2015](#)). Including clouds or assuming a reduced temperature gradient could result in spectra that better match the observations.
3. In H band, the cloudless Sonora-Bobcat models tend to under-predict the observed fluxes by an amount which is larger for later spectral types, cooler T_{eff} , and higher Z . This residual might be explained by the disequilibrium abundance of NH_3 (e.g., [Saumon et al. 2006](#); [Cushing et al. 2011](#)) which is not included by the Sonora-Bobcat assumption of equilibrium chemistry, although our residuals do not seem to precisely coincide with the expected wavelength for NH_3 opacities. Also, this H -band residual could merely be a consequence of the spectral-fitting procedure responding to the over-predicted J -band flux.

4. In *K* band, the cloudless Sonora-Bobcat models tend to under-predict the observed fluxes, which likely arises from the same reason that cause the *J*-band residuals.

In future work, spectroscopic analysis of late-T dwarfs will benefit from models that include improved opacities, clouds, reduced vertical temperature gradient, and/or chemical disequilibrium. Such will also be essential to studying ultracool dwarfs with higher or lower effective temperatures than late-T dwarfs, for which there are already numerous spectra. *James Webb Space Telescope* can further extend spectroscopic observations down to cooler temperatures and wider wavelength coverage. In addition, the analysis conducted in our work can also be extended to other sets of grid models to verify whether the physical assumptions made by those models can reproduce the observations, and what atmospheric processes might be included to improve data-model consistency. Since brown dwarfs harbor similar atmospheric processes as imaged exoplanets, models employed to interpret both classes of objects are generated from the same theoretical framework. Dedicated analyses of brown dwarf atmospheres will therefore help us to robustly characterize direct spectroscopy of exoplanets and thereby understand their appearance, formation, and evolution.

We thank Mark Phillips, Didier Saumon, Caroline Morley, Eugene Magnier, Paul Mollière, Joe Zalesky, Trent Dupuy, Ehsan Gharib-Nezhad for insightful discussions and comments on this work. We thank Ian Czekala, Michael Gully-Santiago, and Miles Lucas for helpful discussions about Starfish. We also thank Michael Gully-Santiago for implementing Starfish for IRTF/SpeX prism data and sharing initial work on spectroscopic analysis for T dwarfs (<https://github.com/gully/jammer-G1570D>).

We thank Trent Dupuy for providing age posteriors of brown dwarf binaries with dynamical mass measurements. This work has benefited from The UltracoolSheet at <http://bit.ly/UltracoolSheet>, maintained by Will Best, Trent Dupuy, Michael Liu, Rob Siverd, and Zhoujian Zhang, and developed from compilations by Dupuy & Liu (2012), Dupuy & Kraus (2013), Liu et al. (2016), Best et al. (2018), and Best et al. (2021). This work benefited from 2017–2019 Exoplanet Summer Program in the Other Worlds Laboratory (OWL) at the University of California, Santa Cruz, a program funded by the Heising-Simons Foundation. M.C.L. acknowledges the National Science Foundation (NSF) grant AST-1518339. This work is funded in part by the Gordon and Betty Moore Foundation through Grant GBMF8550 to M.C.L. The advanced computing resources from the University of Hawaii Information Technology Services – Cyberinfrastructure are greatly acknowledged and Z. Z. thanks the technical support received from Curt Dodds. This research was greatly facilitated by the TOPCAT software written by Mark Taylor (<http://www.starlink.ac.uk/topcat/>). Finally, the authors wish to recognize and acknowledge the very significant cultural role and reverence that the summit of Maunakea has always had within the indigenous Hawaiian community. We are most fortunate to have the opportunity to conduct observations from this mountain.

Facilities: IRTF (SpeX)

Software: Starfish (Czekala et al. 2015), *emcee* (Foreman-Mackey et al. 2013), Spextool (Cushing et al. 2004), TOPCAT (Taylor 2005), Astropy (Astropy Collaboration et al. 2013, 2018), IPython (Pérez & Granger 2007), Numpy (Oliphant 2006), Scipy (Jones et al. 2001), Matplotlib (Hunter 2007).

APPENDIX

A. BOLOMETRIC LUMINOSITIES: COMPARISON WITH LITERATURE

Among our sample, 15 late-T dwarfs have bolometric luminosities in the literature. Filippazzo et al. (2015) constructed SEDs for 14 of our T7–T9 dwarfs by combining optical, near-infrared, and mid-infrared photometry and spectroscopy, and then computed bolometric luminosities by integrating their SEDs, with short-wavelength fluxes linearly extrapolated to zero wavelength and long-wavelength fluxes approximated by a Rayleigh-Jeans tail. Line et al. (2017) performed a retrieval analysis for SpeX prism spectra of 11 of our T7–T8 dwarfs and computed L_{bol} by integrating the fitted models. Six objects in these two studies now have newer parallaxes with much higher precisions: HD 3651B, PSO J043.5395+02.3995, 2MASS J1217110–031113, Ross 458C, ULAS 1416+1348, and GJ 570D. We thereby scale these objects’ literature L_{bol} values with the new parallaxes, without modifying the published uncertainties.

Figure 19 and Table 7 compare our L_{bol} values for these 15 late-T dwarfs with the literature and suggest a general consistency. Our work produces slightly fainter L_{bol} , with the differences having a weighted mean and weighted root mean square of 0.057 ± 0.099 dex compared to Filippazzo et al. (2015) and 0.075 ± 0.044 dex compared to Line et al. (2017). For UGPS J072227.51–054031.2 (UGPS 0722–0540), our estimated L_{bol} is fainter than the value in Filippazzo et al. (2015) by 8.4σ . As shown in Figure 2, our fitted cloudless models do not well match this object’s observed spectrum and our spectroscopically inferred $T_{\text{eff}} = 680 \pm 26$ K is much higher than the values of 500 – 580 K as suggested by Morley et al. (2012) and Tremblin

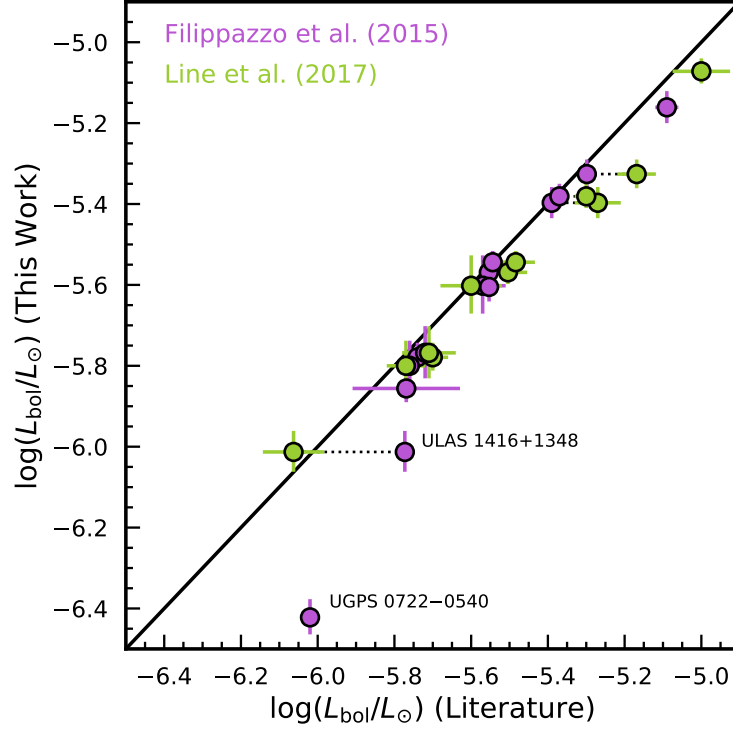


Figure 19. Comparison of bolometric luminosities for 15 late-T dwarfs with measurements both by us and the literature (Appendix A). We use dotted lines to connect results for same object. Our computed L_{bol} 's of these objects are generally consistent with the literature values but are systematically fainter by 0.06 – 0.07 dex.

et al. (2015), whose models account for sulfide clouds or diabatic convection (also see Section 6.2) and can better match this object's spectrum. Our over-estimated T_{eff} for UGPS 0722–0540 might lead to a smaller ratio between the integrated fluxes in mid-infrared wavelengths (approximated by our fitted models) and in near-infrared wavelengths (indicated by our SpeX prism data), resulting in an under-estimated L_{bol} . For ULAS 1416+1348, our derived $L_{\text{bol}} = -6.013^{+0.052}_{-0.049}$ dex is 4.7σ fainter than the value in Filippazzo et al. (2015), but is consistent with that in Line et al. (2017).

B. BOLOMETRIC CORRECTIONS

Table 8 presents our bolometric corrections for late-T dwarfs in J_{MKO} , H_{MKO} , and K_{MKO} bands computed using their bolometric fluxes (with $M_{\text{bol},\odot} = +4.74$). For this calculation, we exclude six objects that are resolved or candidate binaries, as well as two objects with peculiar spectra (2MASS J0939–2448 and ULAS J1416+1348; see Section 4). Comparison with the bolometric corrections of Liu et al. (2010) demonstrates the 1σ consistency. Filippazzo et al. (2015) provided bolometric corrections using 2MASS bands, so we cannot compare directly to their results. Following Dupuy & Liu (2012), we also compute an estimate of the intrinsic (astrophysical) scatter in the bolometric correction at a given spectral type and band.

C. FORWARD-MODELING ANALYSIS WITH THE TRADITIONAL APPROACH

We also conduct the forward-modeling analysis for our late-T dwarfs following the traditional approach described in Paper I. We use the cloudless Sonora-Bobcat model atmospheres over their entire parameter space of $[200, 2400]$ K in T_{eff} , $[3.25, 5.5]$ dex in $\log g$, and $[-0.5, +0.5]$ dex in Z , and use linear interpolation to synthesize model spectra with an arbitrary set of grid parameters. We determine six physical parameters $\{T_{\text{eff}}, \log g, Z, v_r, v \sin i, \log \Omega\}$ with same priors as our Starfish-based analysis (Section 3.1), and construct our covariance matrix by simply placing squared flux uncertainties of spectra along its diagonal axis.

We use *emcee* to fit our $1.0 - 2.5 \mu\text{m}$ spectra with 24 walkers and terminate the fitting process with 3×10^4 iterations given that such number of iterations exceeds 50 times the autocorrelation length of all the fitted parameters. We incorporate the systematic error of 180 km s^{-1} into the inferred radial velocity to account for the uncertainty in the wavelength calibration of the SpeX prism data (Section 3.1). We also incorporate the systematic error of $0.4\sigma_{H_{\text{MKO}}}$ into the inferred $\log \Omega$ to account for the uncertainty in

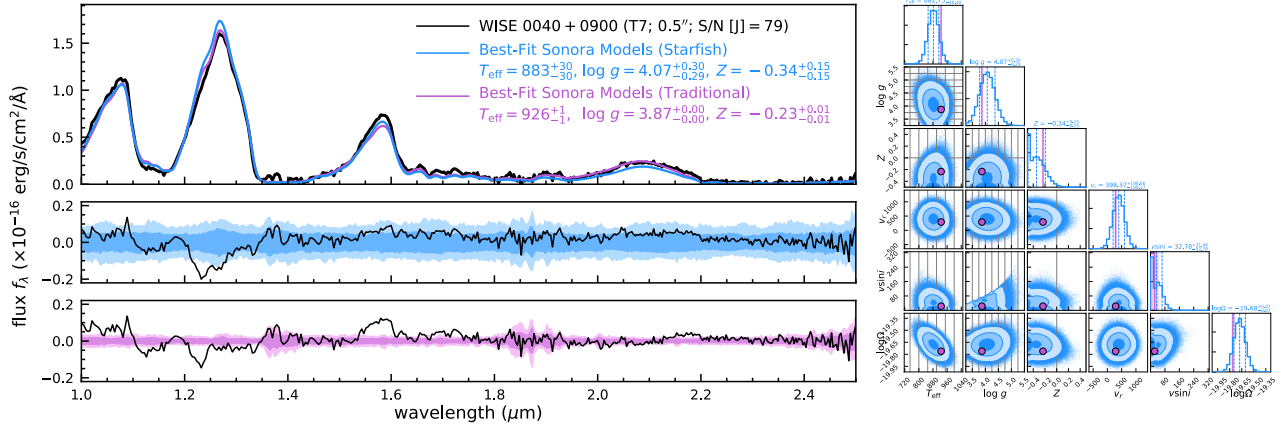


Figure 20. Comparisons of results from Starfish and traditional forward-modeling analyses, with a similar format as Figure 2. Left: The upper panel shows the observed spectrum (black) and the median model spectra of those interpolated at parameters drawn from the MCMC chains based on the Starfish (blue) and traditional (purple) methods. The middle and lower panel show the residual of each method (data–model; black). Right: Posteriors of the six physical parameters $\{T_{\text{eff}}, \log g, Z, v_r, v \sin i, \log \Omega\}$ derived from the Starfish-based forward-modeling analysis (blue). We overlay the median values and uncertainties from the traditional method (purple), shown as vertical lines and shadows in the 1-D histograms and as circles and error bars in the 2-D histograms. We use grey vertical and horizontal lines to mark the $\{T_{\text{eff}}, \log g, Z\}$ grids points of the cloudless Sonora-Bobcat models. Figures of spectral-fitting results for our entire sample (55 late-T dwarfs with 57 spectra) are accessible online.

flux calibration (Section 3.1), where $\sigma_{H_{\text{MKO}}}$ is the photometric error in an object’s H -band magnitude. We compute the objects’ radii (R) and masses (M) using their parallaxes and $\log g$ and $\log \Omega$ posteriors and also compute ages by interpolating the Sonora-Bobcat evolutionary models using the fitted $\{T_{\text{eff}}, \log g, Z\}$. We summarize all inferred parameters and their uncertainties in Table 9.

Figure 20 compares the parameter posteriors and the fitted model spectra (interpolated at parameters drawn from the MCMC samples) derived from the traditional approach to those from the Starfish analysis. While the fitted model spectra by these two methods both match the data, the residuals from the traditional approach significantly exceed measurement uncertainties in some wavelength ranges, indicating that the more sophisticated Starfish covariance matrix better describes the difference between the data and models (also see Figure 5 of Czekala et al. 2015). Also, the fitted models from the two methods are not always identical at several wavelengths, primarily because of their vastly different covariance matrices, which weight residuals and compute the likelihoods differently given the same set of physical parameters.

Figure 21 compares eight physical parameters $\{T_{\text{eff}}, \log g, Z, v_r, v \sin i, \log \Omega, R, M\}$ of late-T dwarfs inferred from the two approaches. The weighted mean and weighted root mean square of the Starfish–Traditional parameter differences are -16 ± 23 K for T_{eff} , -0.09 ± 0.23 dex for $\log g$, -0.09 ± 0.10 dex for Z , 45 ± 125 km s $^{-1}$ for v_r , -1 ± 6 km s $^{-1}$ for $v \sin i$, 0.040 ± 0.061 dex for $\log \Omega$, 0.03 ± 0.06 dex for R , and -0.17 ± 1.14 dex for M . Therefore, the results from these two spectral-fitting methods are generally consistent. Several objects have significantly different properties based on the two methods: WISE 2209 – 2734, ULAS 1416 + 1348, WISE 0500 – 1223, 2MASS 0939 – 2448, and WISE 0458 + 6434.

For WISE 2209 – 2734, the Starfish analysis derives $\log g$ and Z that are smaller than the traditional method by 0.95 ± 0.34 dex and 0.33 ± 0.10 dex, respectively. However, the fitted model spectra from the two methods are similar, given that these parameter offsets follow the $\log g - Z$ degeneracy of the cloudless Sonora-Bobcat models that we find based on the stacked posteriors of our late-T dwarf sample (Section 3.2.2). The different results from the two methods are thus likely caused by the different covariance matrices used to compute the likelihood.

ULAS 1416 + 1348 is a wide-orbit companion to a low-metallicity late-L dwarf (see Section 4.2). Its $\{T_{\text{eff}}, \log g, \log \Omega, R, M\}$ are different between the two methods by $1 - 6\sigma$, but we find the fitted model spectra from Starfish better match the data especially for the blue wing of Y band (Figure 20).

Among the remaining three objects, WISE 0458 + 6434 is a resolved $0.51''$ T8.5+T9 binary (Section 4.1). Binarity can result in spectral peculiarity and cause the two forward-modeling approaches to derive different parameters. The binarity of WISE 0500 – 1223 and 2MASS 0939 – 2448 are uncertain (Section 4.2). In addition, parameter posteriors of WISE 0500 – 1223 inferred from the traditional method show two peaks, with one peak consistent with the Starfish results. This anomaly might also be related to the low S/N of data (≈ 13 in J band).

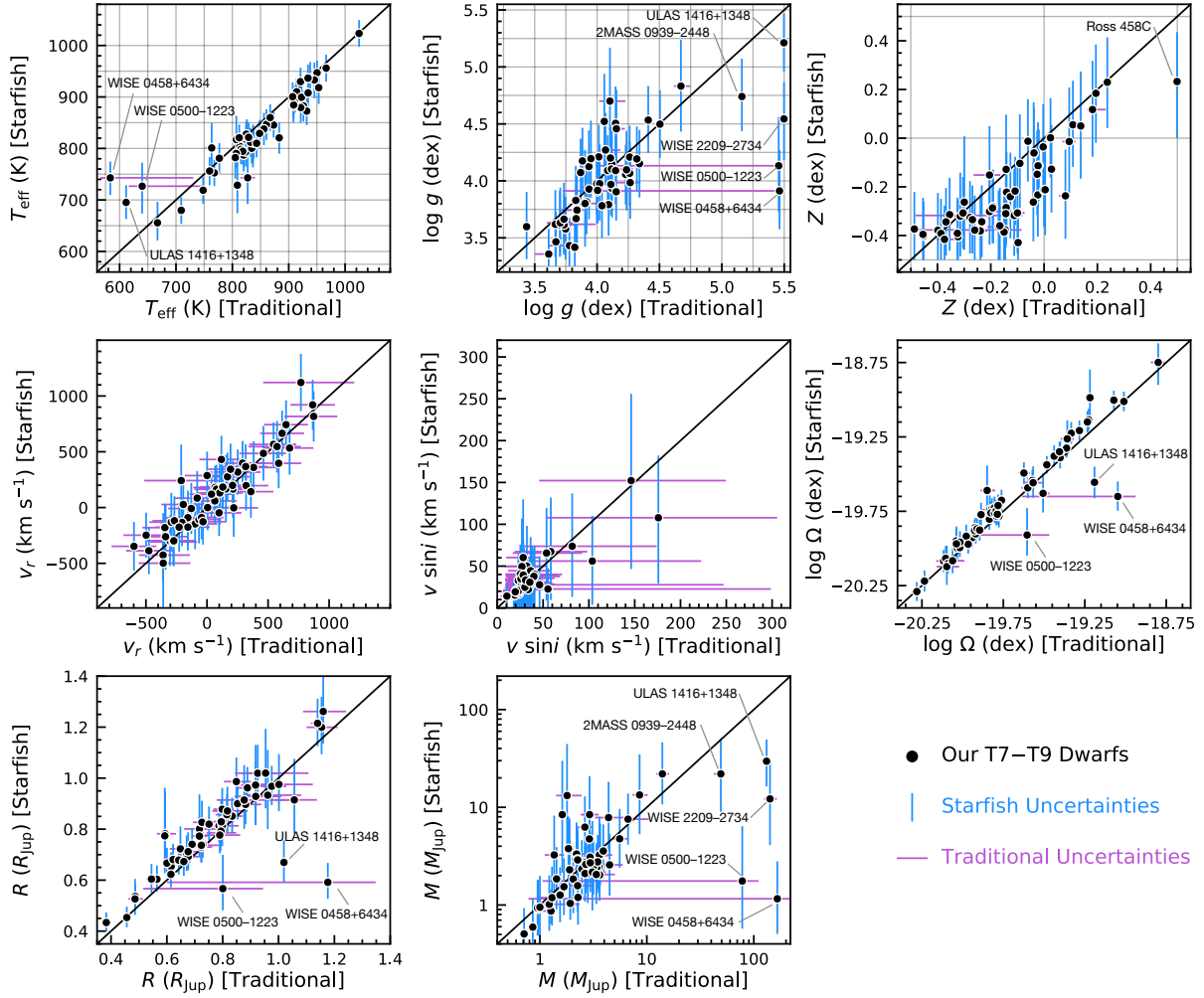


Figure 21. Comparison of eight physical parameters of our late-T dwarfs $\{T_{\text{eff}}, \log g, Z, v_r, v \sin i, \log \Omega, R, M\}$ as inferred from Starfish and traditional forward-modeling analysis (masses are compared in the logarithmic scale). We use grey vertical and horizontal lines to mark the $\{T_{\text{eff}}, \log g, Z\}$ grids of the cloudless Sonora-Bobcat models. The results from the two methods are generally consistent within the uncertainties, although there are systematic differences in almost all parameters except for v_r and $v \sin i$. We label the objects that have significantly different parameters from the two methods and discuss them in Appendix C.

Table 6 compares typical parameter uncertainties between the two methods. The traditional forward-modeling approach produces artificially small parameter errors by factors of 2 – 15 in $\{T_{\text{eff}}, \log g, Z, \log \Omega, R, M\}$ and factors of 1 – 2 in v_r and $v \sin i$ (also see Figure 4). We note that the larger error estimates from Starfish are more realistic, given that Starfish accounts for uncertainties from model interpolation and correlated residuals.

REFERENCES

- Aberasturi, M., Burgasser, A. J., Mora, A., et al. 2014, *AJ*, 148, 129, doi: [10.1088/0004-6256/148/6/129](https://doi.org/10.1088/0004-6256/148/6/129)
- Allard, F. 2014, in *IAU Symposium*, Vol. 299, Exploring the Formation and Evolution of Planetary Systems, ed. M. Booth, B. C. Matthews, & J. R. Graham, 271–272
- Allard, F., Homeier, D., & Freytag, B. 2011, *Astronomical Society of the Pacific Conference Series*, Vol. 448, Model Atmospheres From Very Low Mass Stars to Brown Dwarfs, ed. C. Johns-Krull, M. K. Browning, & A. A. West, 91
- . 2012, *Philosophical Transactions of the Royal Society of London Series A*, 370, 2765, doi: [10.1098/rsta.2011.0269](https://doi.org/10.1098/rsta.2011.0269)
- Allard, N. F., Royer, A., Kielkopf, J. F., & Feautrier, N. 1999, *PhRvA*, 60, 1021, doi: [10.1103/PhysRevA.60.1021](https://doi.org/10.1103/PhysRevA.60.1021)
- Allard, N. F., Spiegelman, F., & Kielkopf, J. F. 2007, *A&A*, 465, 1085, doi: [10.1051/0004-6361:20066616](https://doi.org/10.1051/0004-6361:20066616)
- . 2016, *A&A*, 589, A21, doi: [10.1051/0004-6361/201628270](https://doi.org/10.1051/0004-6361/201628270)
- Allen, P. R., Koerner, D. W., Reid, I. N., & Trilling, D. E. 2005, *ApJ*, 625, 385, doi: [10.1086/429548](https://doi.org/10.1086/429548)
- Allers, K. N., & Liu, M. C. 2013, *ApJ*, 772, 79, doi: [10.1088/0004-637X/772/2/79](https://doi.org/10.1088/0004-637X/772/2/79)
- Astropy Collaboration, Robitaille, T. P., Tollerud, E. J., et al. 2013, *A&A*, 558, A33, doi: [10.1051/0004-6361/201322068](https://doi.org/10.1051/0004-6361/201322068)
- Astropy Collaboration, Price-Whelan, A. M., Sipőcz, B. M., et al. 2018, *AJ*, 156, 123, doi: [10.3847/1538-3881/aabc4f](https://doi.org/10.3847/1538-3881/aabc4f)
- Baraffe, I., Chabrier, G., Allard, F., & Hauschildt, P. H. 1998, *A&A*, 337, 403, <https://arxiv.org/abs/astro-ph/9805009>
- Baraffe, I., Chabrier, G., Barman, T. S., Allard, F., & Hauschildt, P. H. 2003a, *A&A*, 402, 701, doi: [10.1051/0004-6361:20030252](https://doi.org/10.1051/0004-6361:20030252)
- . 2003b, *A&A*, 402, 701, doi: [10.1051/0004-6361:20030252](https://doi.org/10.1051/0004-6361:20030252)
- Barnes, J. W., & Fortney, J. J. 2003, *ApJ*, 588, 545, doi: [10.1086/373893](https://doi.org/10.1086/373893)
- Baudino, J.-L., Mollière, P., Venot, O., et al. 2017, *ApJ*, 850, 150, doi: [10.3847/1538-4357/aa95be](https://doi.org/10.3847/1538-4357/aa95be)
- Beatty, T. G., Morley, C. V., Curtis, J. L., et al. 2018, *AJ*, 156, 168, doi: [10.3847/1538-3881/aad697](https://doi.org/10.3847/1538-3881/aad697)
- Bell, C. P. M., Mamajek, E. E., & Naylor, T. 2015, *MNRAS*, 454, 593, doi: [10.1093/mnras/stv1981](https://doi.org/10.1093/mnras/stv1981)
- Best, W. M. J., Dupuy, T. J., Liu, M. C., Siverd, R. J., & Zhang, Z. 2020b, The UltracoolSheet: Photometry, Astrometry, Spectroscopy, and Multiplicity for 3000+ Ultracool Dwarfs and Imaged Exoplanets, Zenodo, doi: [10.5281/zenodo.4169085](https://doi.org/10.5281/zenodo.4169085)
- Best, W. M. J., Liu, M. C., Magnier, E. A., & Dupuy, T. J. 2020a, *AJ*, 159, 257, doi: [10.3847/1538-3881/ab84f4](https://doi.org/10.3847/1538-3881/ab84f4)
- . 2021, *AJ*, 161, 42, doi: [10.3847/1538-3881/abc893](https://doi.org/10.3847/1538-3881/abc893)
- Best, W. M. J., Liu, M. C., Magnier, E. A., et al. 2015, *ApJ*, 814, 118, doi: [10.1088/0004-637X/814/2/118](https://doi.org/10.1088/0004-637X/814/2/118)
- . 2017, *ApJ*, 837, 95, doi: [10.3847/1538-4357/aa5df0](https://doi.org/10.3847/1538-4357/aa5df0)
- Best, W. M. J., Magnier, E. A., Liu, M. C., et al. 2018, *ApJS*, 234, 1, doi: [10.3847/1538-4365/aa9982](https://doi.org/10.3847/1538-4365/aa9982)
- Bihain, G., Scholz, R. D., Storm, J., & Schnurr, O. 2013, *A&A*, 557, A43, doi: [10.1051/0004-6361/201322141](https://doi.org/10.1051/0004-6361/201322141)
- Bond, J. C., Tinney, C. G., Butler, R. P., et al. 2006, *MNRAS*, 370, 163, doi: [10.1111/j.1365-2966.2006.10459.x](https://doi.org/10.1111/j.1365-2966.2006.10459.x)
- Bowler, B. P., Liu, M. C., & Dupuy, T. J. 2010a, *ApJ*, 710, 45, doi: [10.1088/0004-637X/710/1/45](https://doi.org/10.1088/0004-637X/710/1/45)
- Bowler, B. P., Liu, M. C., Dupuy, T. J., & Cushing, M. C. 2010b, *ApJ*, 723, 850, doi: [10.1088/0004-637X/723/1/850](https://doi.org/10.1088/0004-637X/723/1/850)
- Bowler, B. P., Dupuy, T. J., Endl, M., et al. 2018, *AJ*, 155, 159, doi: [10.3847/1538-3881/aab2a6](https://doi.org/10.3847/1538-3881/aab2a6)
- Brandt, T. D., Dupuy, T. J., Bowler, B. P., et al. 2020, *AJ*, 160, 196, doi: [10.3847/1538-3881/abb45e](https://doi.org/10.3847/1538-3881/abb45e)
- Brewer, J. M., Fischer, D. A., Valenti, J. A., & Piskunov, N. 2016, *ApJS*, 225, 32, doi: [10.3847/0067-0049/225/2/32](https://doi.org/10.3847/0067-0049/225/2/32)
- Burgasser, A. J. 2004, *ApJS*, 155, 191, doi: [10.1086/424386](https://doi.org/10.1086/424386)
- . 2007, *ApJ*, 658, 617, doi: [10.1086/511176](https://doi.org/10.1086/511176)
- Burgasser, A. J. 2014, in *Astronomical Society of India Conference Series*, Vol. 11, Astronomical Society of India Conference Series, 7–16
- Burgasser, A. J., Burrows, A., & Kirkpatrick, J. D. 2006a, *ApJ*, 639, 1095, doi: [10.1086/499344](https://doi.org/10.1086/499344)
- Burgasser, A. J., Cruz, K. L., Cushing, M., et al. 2010a, *ApJ*, 710, 1142, doi: [10.1088/0004-637X/710/2/1142](https://doi.org/10.1088/0004-637X/710/2/1142)
- Burgasser, A. J., Geballe, T. R., Leggett, S. K., Kirkpatrick, J. D., & Golimowski, D. A. 2006b, *ApJ*, 637, 1067, doi: [10.1086/498563](https://doi.org/10.1086/498563)
- Burgasser, A. J., Gelino, C. R., Cushing, M. C., & Kirkpatrick, J. D. 2012, *ApJ*, 745, 26, doi: [10.1088/0004-637X/745/1/26](https://doi.org/10.1088/0004-637X/745/1/26)
- Burgasser, A. J., Kirkpatrick, J. D., Cruz, K. L., et al. 2006c, *ApJS*, 166, 585, doi: [10.1086/506327](https://doi.org/10.1086/506327)
- Burgasser, A. J., Looper, D., & Rayner, J. T. 2010b, *AJ*, 139, 2448, doi: [10.1088/0004-6256/139/6/2448](https://doi.org/10.1088/0004-6256/139/6/2448)
- Burgasser, A. J., Looper, D. L., Kirkpatrick, J. D., Cruz, K. L., & Swift, B. J. 2008a, *ApJ*, 674, 451, doi: [10.1086/524726](https://doi.org/10.1086/524726)
- Burgasser, A. J., McElwain, M. W., Kirkpatrick, J. D., et al. 2004, *AJ*, 127, 2856, doi: [10.1086/383549](https://doi.org/10.1086/383549)
- Burgasser, A. J., & Splat Development Team. 2017, in *Astronomical Society of India Conference Series*, Vol. 14, Astronomical Society of India Conference Series, 7–12
- Burgasser, A. J., Tinney, C. G., Cushing, M. C., et al. 2008b, *ApJL*, 689, L53, doi: [10.1086/595747](https://doi.org/10.1086/595747)

- Burgasser, A. J., Kirkpatrick, J. D., Brown, M. E., et al. 1999, *ApJL*, 522, L65, doi: [10.1086/312221](https://doi.org/10.1086/312221)
- Burgasser, A. J., Kirkpatrick, J. D., Cutri, R. M., et al. 2000, *ApJL*, 531, L57, doi: [10.1086/312522](https://doi.org/10.1086/312522)
- Burgasser, A. J., Kirkpatrick, J. D., Brown, M. E., et al. 2002, *ApJ*, 564, 421, doi: [10.1086/324033](https://doi.org/10.1086/324033)
- Burningham, B., Marley, M. S., Line, M. R., et al. 2017, *MNRAS*, 470, 1177, doi: [10.1093/mnras/stx1246](https://doi.org/10.1093/mnras/stx1246)
- Burningham, B., Pinfield, D. J., Leggett, S. K., et al. 2008, *MNRAS*, 391, 320, doi: [10.1111/j.1365-2966.2008.13885.x](https://doi.org/10.1111/j.1365-2966.2008.13885.x)
- , 2009, *MNRAS*, 395, 1237, doi: [10.1111/j.1365-2966.2009.14620.x](https://doi.org/10.1111/j.1365-2966.2009.14620.x)
- Burningham, B., Pinfield, D. J., Lucas, P. W., et al. 2010a, *MNRAS*, 406, 1885, doi: [10.1111/j.1365-2966.2010.16800.x](https://doi.org/10.1111/j.1365-2966.2010.16800.x)
- Burningham, B., Leggett, S. K., Lucas, P. W., et al. 2010b, *MNRAS*, 404, 1952, doi: [10.1111/j.1365-2966.2010.16411.x](https://doi.org/10.1111/j.1365-2966.2010.16411.x)
- Burningham, B., Lucas, P. W., Leggett, S. K., et al. 2011, *MNRAS*, 414, L90, doi: [10.1111/j.1745-3933.2011.01062.x](https://doi.org/10.1111/j.1745-3933.2011.01062.x)
- Burningham, B., Cardoso, C. V., Smith, L., et al. 2013, *MNRAS*, 433, 457, doi: [10.1093/mnras/stt740](https://doi.org/10.1093/mnras/stt740)
- Burrows, A., Burgasser, A. J., Kirkpatrick, J. D., et al. 2002, *ApJ*, 573, 394, doi: [10.1086/340584](https://doi.org/10.1086/340584)
- Burrows, A., Heng, K., & Nampaisarn, T. 2011, *ApJ*, 736, 47, doi: [10.1088/0004-637X/736/1/47](https://doi.org/10.1088/0004-637X/736/1/47)
- Burrows, A., Hubbard, W. B., Lunine, J. I., & Liebert, J. 2001, *Reviews of Modern Physics*, 73, 719, doi: [10.1103/RevModPhys.73.719](https://doi.org/10.1103/RevModPhys.73.719)
- Burrows, A., & Liebert, J. 1993, *Reviews of Modern Physics*, 65, 301, doi: [10.1103/RevModPhys.65.301](https://doi.org/10.1103/RevModPhys.65.301)
- Burrows, A., Marley, M. S., & Sharp, C. M. 2000, *ApJ*, 531, 438, doi: [10.1086/308462](https://doi.org/10.1086/308462)
- Burrows, A., & Sharp, C. M. 1999, *ApJ*, 512, 843, doi: [10.1086/306811](https://doi.org/10.1086/306811)
- Burrows, A., Sudarsky, D., & Hubeny, I. 2006, *ApJ*, 640, 1063, doi: [10.1086/500293](https://doi.org/10.1086/500293)
- Burrows, A., Marley, M., Hubbard, W. B., et al. 1997, *ApJ*, 491, 856, doi: [10.1086/305002](https://doi.org/10.1086/305002)
- Chabrier, G., Baraffe, I., Allard, F., & Hauschildt, P. 2000, *ApJ*, 542, 464, doi: [10.1086/309513](https://doi.org/10.1086/309513)
- Chambers, K. C., Magnier, E. A., Metcalfe, N., et al. 2016, *arXiv e-prints*. <https://arxiv.org/abs/1612.05560>
- Chiu, K., Fan, X., Leggett, S. K., et al. 2006, *AJ*, 131, 2722, doi: [10.1086/501431](https://doi.org/10.1086/501431)
- Coles, P. A., Yurchenko, S. N., & Tennyson, J. 2019, *MNRAS*, 490, 4638, doi: [10.1093/mnras/stz2778](https://doi.org/10.1093/mnras/stz2778)
- Cushing, M. C., Kirkpatrick, J. D., Gelino, C. R., et al. 2014, *AJ*, 147, 113, doi: [10.1088/0004-6256/147/5/113](https://doi.org/10.1088/0004-6256/147/5/113)
- Cushing, M. C., Vacca, W. D., & Rayner, J. T. 2004, *PASP*, 116, 362, doi: [10.1086/382907](https://doi.org/10.1086/382907)
- Cushing, M. C., Marley, M. S., Saumon, D., et al. 2008, *ApJ*, 678, 1372, doi: [10.1086/526489](https://doi.org/10.1086/526489)
- Cushing, M. C., Kirkpatrick, J. D., Gelino, C. R., et al. 2011, *ApJ*, 743, 50, doi: [10.1088/0004-637X/743/1/50](https://doi.org/10.1088/0004-637X/743/1/50)
- Cutri, R. M., & et al. 2014, *VizieR Online Data Catalog*, 2328
- Czekala, I., Andrews, S. M., Mandel, K. S., Hogg, D. W., & Green, G. M. 2015, *ApJ*, 812, 128, doi: [10.1088/0004-637X/812/2/128](https://doi.org/10.1088/0004-637X/812/2/128)
- Dahn, C. C., Harris, H. C., Vrba, F. J., et al. 2002, *AJ*, 124, 1170, doi: [10.1086/341646](https://doi.org/10.1086/341646)
- Day-Jones, A. C., Marocco, F., Pinfield, D. J., et al. 2013, *MNRAS*, 430, 1171, doi: [10.1093/mnras/sts685](https://doi.org/10.1093/mnras/sts685)
- Deacon, N. R., Magnier, E. A., Liu, M. C., et al. 2017, *MNRAS*, 467, 1126, doi: [10.1093/mnras/stx065](https://doi.org/10.1093/mnras/stx065)
- Del Burgo, C., Martín, E. L., Zapatero Osorio, M. R., & Hauschildt, P. H. 2009, *A&A*, 501, 1059, doi: [10.1051/0004-6361/200810752](https://doi.org/10.1051/0004-6361/200810752)
- Díaz, R. F., Damiani, C., Deleuil, M., et al. 2013, *A&A*, 551, L9, doi: [10.1051/0004-6361/201321124](https://doi.org/10.1051/0004-6361/201321124)
- Dieterich, S. B., Weinberger, A. J., Boss, A. P., et al. 2018, *ApJ*, 865, 28, doi: [10.3847/1538-4357/aadadc](https://doi.org/10.3847/1538-4357/aadadc)
- Dupuy, T. J., & Kraus, A. L. 2013, *Science*, 341, 1492, doi: [10.1126/science.1241917](https://doi.org/10.1126/science.1241917)
- Dupuy, T. J., & Liu, M. C. 2012, *ApJS*, 201, 19, doi: [10.1088/0067-0049/201/2/19](https://doi.org/10.1088/0067-0049/201/2/19)
- , 2017, *ApJS*, 231, 15, doi: [10.3847/1538-4365/aa5e4c](https://doi.org/10.3847/1538-4365/aa5e4c)
- Dupuy, T. J., Liu, M. C., & Ireland, M. J. 2009, *ApJ*, 692, 729, doi: [10.1088/0004-637X/692/1/729](https://doi.org/10.1088/0004-637X/692/1/729)
- , 2014, *ApJ*, 790, 133, doi: [10.1088/0004-637X/790/2/133](https://doi.org/10.1088/0004-637X/790/2/133)
- Edge, A., Sutherland, W., & Viking Team. 2016, *VizieR Online Data Catalog*, II/343
- Edvardsson, B., Andersen, J., Gustafsson, B., et al. 1993, *A&A*, 500, 391
- Eisenhardt, P. R. M., Marocco, F., Fowler, J. W., et al. 2020, *ApJS*, 247, 69, doi: [10.3847/1538-4365/ab7f2a](https://doi.org/10.3847/1538-4365/ab7f2a)
- Faherty, J. K., Burgasser, A. J., Cruz, K. L., et al. 2009, *AJ*, 137, 1, doi: [10.1088/0004-6256/137/1/1](https://doi.org/10.1088/0004-6256/137/1/1)
- Faherty, J. K., Burgasser, A. J., Walter, F. M., et al. 2012, *ApJ*, 752, 56, doi: [10.1088/0004-637X/752/1/56](https://doi.org/10.1088/0004-637X/752/1/56)
- Faherty, J. K., Riedel, A. R., Cruz, K. L., et al. 2016, *ApJS*, 225, 10, doi: [10.3847/0067-0049/225/1/10](https://doi.org/10.3847/0067-0049/225/1/10)
- Fegley, Bruce, J., & Lodders, K. 1994, *Icarus*, 110, 117, doi: [10.1006/icar.1994.1111](https://doi.org/10.1006/icar.1994.1111)
- Filippazzo, J. C., Giorla Godfrey, P., Cruz, K. L., et al. 2016, *The BDNYC Database*, Zenodo, doi: [10.5281/zenodo.45169](https://doi.org/10.5281/zenodo.45169)
- Filippazzo, J. C., Rice, E. L., Faherty, J., et al. 2015, *ApJ*, 810, 158, doi: [10.1088/0004-637X/810/2/158](https://doi.org/10.1088/0004-637X/810/2/158)

- Foreman-Mackey, D., Hogg, D. W., Lang, D., & Goodman, J. 2013, *PASP*, 125, 306, doi: [10.1086/670067](https://doi.org/10.1086/670067)
- Fortney, J. J., Marley, M. S., Saumon, D., & Lodders, K. 2008, *ApJ*, 683, 1104, doi: [10.1086/589942](https://doi.org/10.1086/589942)
- Gagné, J., Mamajek, E. E., Malo, L., et al. 2018, *ApJ*, 856, 23, doi: [10.3847/1538-4357/aaae09](https://doi.org/10.3847/1538-4357/aaae09)
- Gaia Collaboration, Prusti, T., de Bruijne, J. H. J., et al. 2016a, *A&A*, 595, A1, doi: [10.1051/0004-6361/201629272](https://doi.org/10.1051/0004-6361/201629272)
- Gaia Collaboration, Brown, A. G. A., Vallenari, A., et al. 2016b, *A&A*, 595, A2, doi: [10.1051/0004-6361/201629512](https://doi.org/10.1051/0004-6361/201629512)
- . 2018, *A&A*, 616, A1, doi: [10.1051/0004-6361/201833051](https://doi.org/10.1051/0004-6361/201833051)
- Gelino, C. R., Kirkpatrick, J. D., Cushing, M. C., et al. 2011, *AJ*, 142, 57, doi: [10.1088/0004-6256/142/2/57](https://doi.org/10.1088/0004-6256/142/2/57)
- Goldman, B., Marsat, S., Henning, T., Clemens, C., & Greiner, J. 2010, *MNRAS*, 405, 1140, doi: [10.1111/j.1365-2966.2010.16524.x](https://doi.org/10.1111/j.1365-2966.2010.16524.x)
- Golimowski, D. A., Leggett, S. K., Marley, M. S., et al. 2004, *AJ*, 127, 3516, doi: [10.1086/420709](https://doi.org/10.1086/420709)
- Gonzales, E. C., Burningham, B., Faherty, J. K., et al. 2020, *ApJ*, 905, 46, doi: [10.3847/1538-4357/abbee2](https://doi.org/10.3847/1538-4357/abbee2)
- Gully-Santiago, M. A., Herczeg, G. J., Czekala, I., et al. 2017, *ApJ*, 836, 200, doi: [10.3847/1538-4357/836/2/200](https://doi.org/10.3847/1538-4357/836/2/200)
- Hewett, P. C., Warren, S. J., Leggett, S. K., & Hodgkin, S. T. 2006, *MNRAS*, 367, 454, doi: [10.1111/j.1365-2966.2005.09969.x](https://doi.org/10.1111/j.1365-2966.2005.09969.x)
- Hinkel, N. R., Timmes, F. X., Young, P. A., Pagano, M. D., & Turnbull, M. C. 2014, *AJ*, 148, 54, doi: [10.1088/0004-6256/148/3/54](https://doi.org/10.1088/0004-6256/148/3/54)
- Hinkel, N. R., Young, P. A., Pagano, M. D., et al. 2016, *ApJS*, 226, 4, doi: [10.3847/0067-0049/226/1/4](https://doi.org/10.3847/0067-0049/226/1/4)
- Hinkel, N. R., Mamajek, E. E., Turnbull, M. C., et al. 2017, *ApJ*, 848, 34, doi: [10.3847/1538-4357/aa8b0f](https://doi.org/10.3847/1538-4357/aa8b0f)
- Hunter, J. D. 2007, *Computing in Science & Engineering*, 9, 90, doi: [10.1109/MCSE.2007.55](https://doi.org/10.1109/MCSE.2007.55)
- Ivanyuk, O. M., Jenkins, J. S., Pavlenko, Y. V., Jones, H. R. A., & Pinfield, D. J. 2017, *MNRAS*, 468, 4151, doi: [10.1093/mnras/stx647](https://doi.org/10.1093/mnras/stx647)
- Jenkins, J. S., Jones, H. R. A., Pavlenko, Y., et al. 2008, *A&A*, 485, 571, doi: [10.1051/0004-6361:20078611](https://doi.org/10.1051/0004-6361:20078611)
- Jones, E., Oliphant, T., Peterson, P., et al. 2001, *SciPy: Open source scientific tools for Python*. <http://www.scipy.org/>
- Kirkpatrick, J. D., Reid, I. N., Liebert, J., et al. 1999, *ApJ*, 519, 802, doi: [10.1086/307414](https://doi.org/10.1086/307414)
- Kirkpatrick, J. D., Cruz, K. L., Barman, T. S., et al. 2008, *ApJ*, 689, 1295, doi: [10.1086/592768](https://doi.org/10.1086/592768)
- Kirkpatrick, J. D., Cushing, M. C., Gelino, C. R., et al. 2011, *ApJS*, 197, 19, doi: [10.1088/0067-0049/197/2/19](https://doi.org/10.1088/0067-0049/197/2/19)
- Kirkpatrick, J. D., Gelino, C. R., Cushing, M. C., et al. 2012, *ApJ*, 753, 156, doi: [10.1088/0004-637X/753/2/156](https://doi.org/10.1088/0004-637X/753/2/156)
- Kirkpatrick, J. D., Martin, E. C., Smart, R. L., et al. 2019, *ApJS*, 240, 19, doi: [10.3847/1538-4365/aaf6af](https://doi.org/10.3847/1538-4365/aaf6af)
- Knapp, G. R., Leggett, S. K., Fan, X., et al. 2004, *AJ*, 127, 3553, doi: [10.1086/420707](https://doi.org/10.1086/420707)
- Lawrence, A., Warren, S. J., Almaini, O., et al. 2007, *MNRAS*, 379, 1599, doi: [10.1111/j.1365-2966.2007.12040.x](https://doi.org/10.1111/j.1365-2966.2007.12040.x)
- . 2012, *VizieR Online Data Catalog*, II/314
- Leggett, S. K., Marley, M. S., Freedman, R., et al. 2007, *ApJ*, 667, 537, doi: [10.1086/519948](https://doi.org/10.1086/519948)
- Leggett, S. K., Tremblin, P., Esplin, T. L., Luhman, K. L., & Morley, C. V. 2017, *ApJ*, 842, 118, doi: [10.3847/1538-4357/aa6fb5](https://doi.org/10.3847/1538-4357/aa6fb5)
- Leggett, S. K., Golimowski, D. A., Fan, X., et al. 2002, *ApJ*, 564, 452, doi: [10.1086/324037](https://doi.org/10.1086/324037)
- Leggett, S. K., Cushing, M. C., Saumon, D., et al. 2009, *ApJ*, 695, 1517, doi: [10.1088/0004-637X/695/2/1517](https://doi.org/10.1088/0004-637X/695/2/1517)
- Leggett, S. K., Burningham, B., Saumon, D., et al. 2010, *ApJ*, 710, 1627, doi: [10.1088/0004-637X/710/2/1627](https://doi.org/10.1088/0004-637X/710/2/1627)
- Leggett, S. K., Saumon, D., Marley, M. S., et al. 2012, *ApJ*, 748, 74, doi: [10.1088/0004-637X/748/2/74](https://doi.org/10.1088/0004-637X/748/2/74)
- Leggett, S. K., Dupuy, T. J., Morley, C. V., et al. 2019, *ApJ*, 882, 117, doi: [10.3847/1538-4357/ab3393](https://doi.org/10.3847/1538-4357/ab3393)
- Liebert, J., & Burgasser, A. J. 2007, *ApJ*, 655, 522, doi: [10.1086/509882](https://doi.org/10.1086/509882)
- Line, M. R., Teske, J., Burningham, B., Fortney, J. J., & Marley, M. S. 2015, *ApJ*, 807, 183, doi: [10.1088/0004-637X/807/2/183](https://doi.org/10.1088/0004-637X/807/2/183)
- Line, M. R., Marley, M. S., Liu, M. C., et al. 2017, *ApJ*, 848, 83, doi: [10.3847/1538-4357/aa7ff0](https://doi.org/10.3847/1538-4357/aa7ff0)
- Liu, M. C., Dupuy, T. J., & Allers, K. N. 2016, *ApJ*, 833, 96, doi: [10.3847/1538-4357/833/1/96](https://doi.org/10.3847/1538-4357/833/1/96)
- Liu, M. C., Dupuy, T. J., Bowler, B. P., Leggett, S. K., & Best, W. M. J. 2012, *ApJ*, 758, 57, doi: [10.1088/0004-637X/758/1/57](https://doi.org/10.1088/0004-637X/758/1/57)
- Liu, M. C., Dupuy, T. J., & Ireland, M. J. 2008, *ApJ*, 689, 436, doi: [10.1086/591837](https://doi.org/10.1086/591837)
- Liu, M. C., Dupuy, T. J., & Leggett, S. K. 2010, *ApJ*, 722, 311, doi: [10.1088/0004-637X/722/1/311](https://doi.org/10.1088/0004-637X/722/1/311)
- Liu, M. C., Leggett, S. K., & Chiu, K. 2007, *ApJ*, 660, 1507, doi: [10.1086/512662](https://doi.org/10.1086/512662)
- Liu, M. C., Leggett, S. K., Golimowski, D. A., et al. 2006, *ApJ*, 647, 1393, doi: [10.1086/505561](https://doi.org/10.1086/505561)
- Liu, M. C., Delorme, P., Dupuy, T. J., et al. 2011a, *ApJ*, 740, 108, doi: [10.1088/0004-637X/740/2/108](https://doi.org/10.1088/0004-637X/740/2/108)
- Liu, M. C., Deacon, N. R., Magnier, E. A., et al. 2011b, *ApJL*, 740, L32, doi: [10.1088/2041-8205/740/2/L32](https://doi.org/10.1088/2041-8205/740/2/L32)
- Lodders, K. 1999, *ApJ*, 519, 793, doi: [10.1086/307387](https://doi.org/10.1086/307387)
- . 2002, *ApJ*, 577, 974, doi: [10.1086/342241](https://doi.org/10.1086/342241)

- Lodders, K., Palme, H., & Gail, H. P. 2009, *Landolt Bönstein*, 4B, 712, doi: [10.1007/978-3-540-88055-4_34](https://doi.org/10.1007/978-3-540-88055-4_34)
- Lodieu, N. 2013, *MNRAS*, 431, 3222, doi: [10.1093/mnras/stt402](https://doi.org/10.1093/mnras/stt402)
- Lodieu, N., Hambly, N. C., Jameson, R. F., et al. 2007, *MNRAS*, 374, 372, doi: [10.1111/j.1365-2966.2006.11151.x](https://doi.org/10.1111/j.1365-2966.2006.11151.x)
- Looper, D. L., Gelino, C. R., Burgasser, A. J., & Kirkpatrick, J. D. 2008, *ApJ*, 685, 1183, doi: [10.1086/590382](https://doi.org/10.1086/590382)
- Looper, D. L., Kirkpatrick, J. D., & Burgasser, A. J. 2007, *AJ*, 134, 1162, doi: [10.1086/520645](https://doi.org/10.1086/520645)
- Lucas, P. W., Tinney, C. G., Burningham, B., et al. 2010, *MNRAS*, 408, L56, doi: [10.1111/j.1745-3933.2010.00927.x](https://doi.org/10.1111/j.1745-3933.2010.00927.x)
- Luhman, K. L. 2006, *ApJ*, 645, 676, doi: [10.1086/504073](https://doi.org/10.1086/504073)
- Luhman, K. L., & Mamajek, E. E. 2012, *ApJ*, 758, 31, doi: [10.1088/0004-637X/758/1/31](https://doi.org/10.1088/0004-637X/758/1/31)
- Luhman, K. L., Mamajek, E. E., Allen, P. R., & Cruz, K. L. 2009, *ApJ*, 703, 399, doi: [10.1088/0004-637X/703/1/399](https://doi.org/10.1088/0004-637X/703/1/399)
- Luhman, K. L., Patten, B. M., Marengo, M., et al. 2007, *ApJ*, 654, 570, doi: [10.1086/509073](https://doi.org/10.1086/509073)
- Luhman, K. L., Loutrel, N. P., McCurdy, N. S., et al. 2012, *ApJ*, 760, 152, doi: [10.1088/0004-637X/760/2/152](https://doi.org/10.1088/0004-637X/760/2/152)
- Mace, G. N., Kirkpatrick, J. D., Cushing, M. C., et al. 2013a, *ApJS*, 205, 6, doi: [10.1088/0067-0049/205/1/6](https://doi.org/10.1088/0067-0049/205/1/6)
- . 2013b, *ApJ*, 777, 36, doi: [10.1088/0004-637X/777/1/36](https://doi.org/10.1088/0004-637X/777/1/36)
- Mace, G. N., Mann, A. W., Skiff, B. A., et al. 2018, *ApJ*, 854, 145, doi: [10.3847/1538-4357/aaa8dd](https://doi.org/10.3847/1538-4357/aaa8dd)
- Mainzer, A., Cushing, M. C., Skrutskie, M., et al. 2011, *ApJ*, 726, 30, doi: [10.1088/0004-637X/726/1/30](https://doi.org/10.1088/0004-637X/726/1/30)
- Manjavacas, E., Apai, D., Zhou, Y., et al. 2019, *AJ*, 157, 101, doi: [10.3847/1538-3881/aaf88f](https://doi.org/10.3847/1538-3881/aaf88f)
- Marley, M. S., & Robinson, T. D. 2015, *ARA&A*, 53, 279, doi: [10.1146/annurev-astro-082214-122522](https://doi.org/10.1146/annurev-astro-082214-122522)
- Marley, M. S., Saumon, D., Fortney, J. J., et al. 2017, in *American Astronomical Society Meeting Abstracts*, Vol. 230, American Astronomical Society Meeting Abstracts #230, 315.07
- Marley, M. S., Saumon, D., & Goldblatt, C. 2010, *ApJL*, 723, L117, doi: [10.1088/2041-8205/723/1/L117](https://doi.org/10.1088/2041-8205/723/1/L117)
- Marley, M. S., Seager, S., Saumon, D., et al. 2002, *ApJ*, 568, 335, doi: [10.1086/338800](https://doi.org/10.1086/338800)
- Marocco, F., Eisenhardt, P. R. M., Fowler, J. W., et al. 2020, *arXiv e-prints*, arXiv:2012.13084, <https://arxiv.org/abs/2012.13084>
- McMahon, R. G., Banerji, M., Gonzalez, E., et al. 2013, *The Messenger*, 154, 35
- Meisner, A. M., Faherty, J. K., Kirkpatrick, J. D., et al. 2020, *ApJ*, 899, 123, doi: [10.3847/1538-4357/aba633](https://doi.org/10.3847/1538-4357/aba633)
- Metchev, S. A., & Hillenbrand, L. A. 2006, *ApJ*, 651, 1166, doi: [10.1086/507836](https://doi.org/10.1086/507836)
- Mollière, P., Wardenier, J. P., van Boekel, R., et al. 2019, *A&A*, 627, A67, doi: [10.1051/0004-6361/201935470](https://doi.org/10.1051/0004-6361/201935470)
- Montet, B. T., Johnson, J. A., Muirhead, P. S., et al. 2015, *ApJ*, 800, 134, doi: [10.1088/0004-637X/800/2/134](https://doi.org/10.1088/0004-637X/800/2/134)
- Morley, C. V., Fortney, J. J., Marley, M. S., et al. 2012, *ApJ*, 756, 172, doi: [10.1088/0004-637X/756/2/172](https://doi.org/10.1088/0004-637X/756/2/172)
- Mugrauer, M., Seifahrt, A., Neuhäuser, R., & Mazeh, T. 2006, *MNRAS*, 373, L31, doi: [10.1111/j.1745-3933.2006.00237.x](https://doi.org/10.1111/j.1745-3933.2006.00237.x)
- Nakajima, T., Oppenheimer, B. R., Kulkarni, S. R., et al. 1995, *Nature*, 378, 463, doi: [10.1038/378463a0](https://doi.org/10.1038/378463a0)
- Oliphant, T. 2006, *NumPy: A guide to NumPy, USA: Trelgol Publishing*. <http://www.numpy.org/>
- Pérez, F., & Granger, B. E. 2007, *Computing in Science and Engineering*, 9, 21, doi: [10.1109/MCSE.2007.53](https://doi.org/10.1109/MCSE.2007.53)
- Petigura, E. A., & Marcy, G. W. 2011, *ApJ*, 735, 41, doi: [10.1088/0004-637X/735/1/41](https://doi.org/10.1088/0004-637X/735/1/41)
- Phillips, M. W., Tremblin, P., Baraffe, I., et al. 2020, *A&A*, 637, A38, doi: [10.1051/0004-6361/201937381](https://doi.org/10.1051/0004-6361/201937381)
- Pinfield, D. J., Burningham, B., Lodieu, N., et al. 2012, *MNRAS*, 422, 1922, doi: [10.1111/j.1365-2966.2012.20549.x](https://doi.org/10.1111/j.1365-2966.2012.20549.x)
- Pinfield, D. J., Gomes, J., Day-Jones, A. C., et al. 2014, *MNRAS*, 437, 1009, doi: [10.1093/mnras/stt1437](https://doi.org/10.1093/mnras/stt1437)
- Ramírez, I., Allende Prieto, C., & Lambert, D. L. 2013, *ApJ*, 764, 78, doi: [10.1088/0004-637X/764/1/78](https://doi.org/10.1088/0004-637X/764/1/78)
- Rayner, J. T., Toomey, D. W., Onaka, P. M., et al. 2003, *PASP*, 115, 362, doi: [10.1086/367745](https://doi.org/10.1086/367745)
- Rice, E. L., Barman, T., Mclean, I. S., Prato, L., & Kirkpatrick, J. D. 2010, *ApJS*, 186, 63, doi: [10.1088/0067-0049/186/1/63](https://doi.org/10.1088/0067-0049/186/1/63)
- Riedel, A. R., Blunt, S. C., Lambrides, E. L., et al. 2017, *AJ*, 153, 95, doi: [10.3847/1538-3881/153/3/95](https://doi.org/10.3847/1538-3881/153/3/95)
- Santos, N. C., Israelian, G., & Mayor, M. 2004, *A&A*, 415, 1153, doi: [10.1051/0004-6361:20034469](https://doi.org/10.1051/0004-6361:20034469)
- Saumon, D., & Marley, M. S. 2008, *ApJ*, 689, 1327, doi: [10.1086/592734](https://doi.org/10.1086/592734)
- Saumon, D., Marley, M. S., Abel, M., Frommhold, L., & Freedman, R. S. 2012, *ApJ*, 750, 74, doi: [10.1088/0004-637X/750/1/74](https://doi.org/10.1088/0004-637X/750/1/74)
- Saumon, D., Marley, M. S., Cushing, M. C., et al. 2006, *ApJ*, 647, 552, doi: [10.1086/505419](https://doi.org/10.1086/505419)
- Saumon, D., Marley, M. S., Leggett, S. K., et al. 2007, *ApJ*, 656, 1136, doi: [10.1086/510557](https://doi.org/10.1086/510557)
- Schmidt, S. J., Cruz, K. L., Bongiorno, B. J., Liebert, J., & Reid, I. N. 2007, *AJ*, 133, 2258, doi: [10.1086/512158](https://doi.org/10.1086/512158)
- Schmidt, S. J., West, A. A., Burgasser, A. J., Bochanski, J. J., & Hawley, S. L. 2010, *AJ*, 139, 1045, doi: [10.1088/0004-6256/139/3/1045](https://doi.org/10.1088/0004-6256/139/3/1045)
- Schneider, A. C., Cushing, M. C., Kirkpatrick, J. D., et al. 2015, *ApJ*, 804, 92, doi: [10.1088/0004-637X/804/2/92](https://doi.org/10.1088/0004-637X/804/2/92)

- Scholz, R. D. 2010a, *A&A*, 510, L8,
doi: [10.1051/0004-6361/201014078](https://doi.org/10.1051/0004-6361/201014078)
- . 2010b, *A&A*, 515, A92,
doi: [10.1051/0004-6361/201014264](https://doi.org/10.1051/0004-6361/201014264)
- Scholz, R. D., Bihain, G., Schnurr, O., & Storm, J. 2011, *A&A*, 532, L5, doi: [10.1051/0004-6361/201117297](https://doi.org/10.1051/0004-6361/201117297)
- Siverd, R. J., Beatty, T. G., Pepper, J., et al. 2012, *ApJ*, 761, 123,
doi: [10.1088/0004-637X/761/2/123](https://doi.org/10.1088/0004-637X/761/2/123)
- Skrutskie, M. F., Cutri, R. M., Stiening, R., et al. 2006, *AJ*, 131, 1163, doi: [10.1086/498708](https://doi.org/10.1086/498708)
- Smiljanic, R., Korn, A. J., Bergemann, M., et al. 2014, *A&A*, 570, A122, doi: [10.1051/0004-6361/201423937](https://doi.org/10.1051/0004-6361/201423937)
- Soto, M. G., & Jenkins, J. S. 2018, *A&A*, 615, A76,
doi: [10.1051/0004-6361/201731533](https://doi.org/10.1051/0004-6361/201731533)
- Stephens, D. C., Leggett, S. K., Cushing, M. C., et al. 2009, *ApJ*, 702, 154, doi: [10.1088/0004-637X/702/1/154](https://doi.org/10.1088/0004-637X/702/1/154)
- Taylor, M. B. 2005, in *Astronomical Society of the Pacific Conference Series*, Vol. 347, *Astronomical Data Analysis Software and Systems XIV*, ed. P. Shopbell, M. Britton, & R. Ebert, 29
- Thompson, M. A., Kirkpatrick, J. D., Mace, G. N., et al. 2013, *PASP*, 125, 809, doi: [10.1086/671426](https://doi.org/10.1086/671426)
- Tinney, C. G., Burgasser, A. J., & Kirkpatrick, J. D. 2003, *AJ*, 126, 975, doi: [10.1086/376481](https://doi.org/10.1086/376481)
- Tinney, C. G., Burgasser, A. J., Kirkpatrick, J. D., & McElwain, M. W. 2005, *AJ*, 130, 2326, doi: [10.1086/491734](https://doi.org/10.1086/491734)
- Tinney, C. G., Kirkpatrick, J. D., Faherty, J. K., et al. 2018, *ApJS*, 236, 28, doi: [10.3847/1538-4365/aabad3](https://doi.org/10.3847/1538-4365/aabad3)
- Torres, G., Fischer, D. A., Sozzetti, A., et al. 2012, *ApJ*, 757, 161,
doi: [10.1088/0004-637X/757/2/161](https://doi.org/10.1088/0004-637X/757/2/161)
- Tremblin, P., Amundsen, D. S., Chabrier, G., et al. 2016, *ApJL*, 817, L19, doi: [10.3847/2041-8205/817/2/L19](https://doi.org/10.3847/2041-8205/817/2/L19)
- Tremblin, P., Amundsen, D. S., Mourier, P., et al. 2015, *ApJL*, 804, L17, doi: [10.1088/2041-8205/804/1/L17](https://doi.org/10.1088/2041-8205/804/1/L17)
- Tremblin, P., Chabrier, G., Baraffe, I., et al. 2017, *ApJ*, 850, 46,
doi: [10.3847/1538-4357/aa9214](https://doi.org/10.3847/1538-4357/aa9214)
- Tremblin, P., Padiou, T., Phillips, M. W., et al. 2019, *ApJ*, 876, 144, doi: [10.3847/1538-4357/ab05db](https://doi.org/10.3847/1538-4357/ab05db)
- UKIDSS Consortium. 2012, *VizieR Online Data Catalog*, II/316
- Valenti, J. A., & Fischer, D. A. 2005, *ApJS*, 159, 141,
doi: [10.1086/430500](https://doi.org/10.1086/430500)
- van Leeuwen, F. 2007, *A&A*, 474, 653,
doi: [10.1051/0004-6361:20078357](https://doi.org/10.1051/0004-6361:20078357)
- Wielen, R. 1977, *A&A*, 60, 263
- Wright, E. L., Eisenhardt, P. R. M., Mainzer, A. K., et al. 2010, *AJ*, 140, 1868, doi: [10.1088/0004-6256/140/6/1868](https://doi.org/10.1088/0004-6256/140/6/1868)
- Yurchenko, S. N., Barber, R. J., & Tennyson, J. 2011, *MNRAS*, 413, 1828, doi: [10.1111/j.1365-2966.2011.18261.x](https://doi.org/10.1111/j.1365-2966.2011.18261.x)
- Zahnle, K. J., & Marley, M. S. 2014, *ApJ*, 797, 41,
doi: [10.1088/0004-637X/797/1/41](https://doi.org/10.1088/0004-637X/797/1/41)
- Zalesky, J. A., Line, M. R., Schneider, A. C., & Patience, J. 2019, *ApJ*, 877, 24, doi: [10.3847/1538-4357/ab16db](https://doi.org/10.3847/1538-4357/ab16db)
- Zapatero Osorio, M. R., Martín, E. L., Béjar, V. J. S., et al. 2007, *ApJ*, 666, 1205, doi: [10.1086/520673](https://doi.org/10.1086/520673)
- Zhang, Z., Liu, M. C., Best, W. M. J., Dupuy, T. J., & Siverd, R. J. 2021, *ApJ*, 911, 7, doi: [10.3847/1538-4357/abe3fa](https://doi.org/10.3847/1538-4357/abe3fa)
- Zhang, Z., Liu, M. C., Marley, M. S., Line, M. R., & Best, W. M. J. 2020b, *arXiv e-prints*, arXiv:2011.12294.
<https://arxiv.org/abs/2011.12294>
- Zhang, Z., Liu, M. C., Best, W. M. J., et al. 2018a, *ApJ*, 858, 41,
doi: [10.3847/1538-4357/aab269](https://doi.org/10.3847/1538-4357/aab269)
- Zhang, Z., Liu, M. C., Hermes, J. J., et al. 2020a, *ApJ*, 891, 171,
doi: [10.3847/1538-4357/ab765c](https://doi.org/10.3847/1538-4357/ab765c)
- Zhang, Z. H., Pinfield, D. J., Gálvez-Ortiz, M. C., et al. 2017, *MNRAS*, 464, 3040, doi: [10.1093/mnras/stw2438](https://doi.org/10.1093/mnras/stw2438)
- . 2018b, *MNRAS*, 479, 1383,
doi: [10.1093/mnras/sty1352](https://doi.org/10.1093/mnras/sty1352)
- Zuckerman, B. 2019, *ApJ*, 870, 27,
doi: [10.3847/1538-4357/aaee66](https://doi.org/10.3847/1538-4357/aaee66)
- Zuckerman, B., Bessell, M. S., Song, I., & Kim, S. 2006, *ApJL*, 649, L115, doi: [10.1086/508060](https://doi.org/10.1086/508060)

Table 1. Sample of T7–T9 Dwarfs: Spectroscopy

Object	Type ^a	SpT	IRTF/SpeX Spectra				References			
			Slit ($''$)	J-band S/N ^b	Obs. Date ^c (UT)	A0V Star ^c	Discovery	Type	SpT	Spectra
HD 3651B	C	T7.5	0.5	73	–	–	10	10	12	11
WISE J004024.88 + 090054.8		T7	0.5	80	–	–	34	...	34	38
WISE J004945.61 + 215120.0		T8.5	0.5	78	–	–	34	...	34	38
			0.8	35	2012-01-20	HD 9711	34	...	34	40
2MASS J00501994 – 3322402		T7	0.5	61	–	–	5	...	6	8
WISEPA J012333.21 + 414203.9		T7	0.8	60	2017-10-22	HD 1561	25	...	25	40
WISEPC J022322.39 – 293258.1		T7.5	0.5	50	–	–	25	...	25	38
WISE J024124.73 – 365328.0		T7	0.8	57	2017-11-15	HD 18546	29	...	39	40
WISE J024512.62 – 345047.8		T8	0.5	27	–	–	34	...	34	38
PSO J043.5395 + 02.3995		T8	0.5	107	–	–	26,28	...	26	38
WISE J032547.72 + 083118.2		T7	0.5	66	–	–	34	...	34	38
2MASS J0415195 – 093506		T8	0.5	176	–	–	3	...	6	38
WISEPA J045853.89 + 643452.9	B	T8.5	0.5	24	–	–	27	24	25	38
WISEPA J050003.05 – 122343.2		T8	0.5	13	–	–	25	...	25	38
WISE J052126.29 + 102528.4		T7.5	0.8	79	2017-03-13	HD 35036	33	...	33	40
UGPS J052127.27 + 364048.6		T8.5	0.8	40	2017-10-21	HD 31069	22	...	22	40
WISE J061437.73 + 095135.0		T7	0.8	94	2017-11-02	HD 41076	34	...	34	40
WISEPA J062309.94 – 045624.6		T8	0.5	14	–	–	25	...	25	38
UGPS J072227.51 – 054031.2		T9	0.5	79	–	–	19	...	23	38
2MASS J0727182 + 171001		T7	0.5	106	–	–	3	...	6	8
2MASS J07290002 – 3954043		T8 pec	0.5	52	–	–	13	...	13	13
2MASS J09393548 – 2448279		T8	0.5	50	–	–	5	...	6	8
ULAS J102940.52 + 093514.6		T8	0.5	45	–	–	32	...	32	38
WISE J103907.73 – 160002.9	B?	T7.5	0.5	29	–	–	34	...	34	38
WISE J105257.95 – 194250.2		T7.5	0.5	67	–	–	35	...	35	38
2MASS J11145133 – 2618235		T7.5	0.5	29	–	–	5	...	6	8
WISE J112438.12 – 042149.7		T7	0.5	81	–	–	34	...	34	38
2MASS J1217110 – 031113		T7.5	0.5	31	–	–	1	...	6	8
WISE J125448.52 – 072828.4		T7	0.5	21	–	–	35	...	35	38
WISE J125715.90 + 400854.2		T7	0.5	33	–	–	34	...	34	38
Ross 458C	C	T8	0.5	43	2015-07-07	HD 116960	18	18	23	40
WISEPA J132233.66 – 234017.1		T8	0.5	27	–	–	25	...	25	38
ULAS J141623.94 + 134836.3	C	(sd) T7.5	0.5	48	–	–	17,21	17,21	14	38

Table 1 continued

Table 1 (*continued*)

Object	Type ^a	SpT	IRTF/SpeX Spectra				References			
			Slit ($''$)	J -band S/N ^b	Obs. Date ^c (UT)	A0V Star ^c	Discovery	Type	SpT	Spectra
WISEPC J145715.03 + 581510.2		T7	0.5	39	—	—	25	...	25	38
GJ 570D	C	T7.5	0.5	37	—	—	2	2	6	4
PSO J224.3820 + 47.4057		T7	0.8	40	—	—	37	...	37	37
SDSS J150411.63 + 102718.4	B?	T7	0.8	49	2017-05-12	HD 132072	9	...	9	40
2MASS J1553022 + 153236	B	T7	0.5	141	—	—	3	7	6	16
SDSS J162838.77 + 230821.1		T7	0.8	53	—	—	9	...	9	38
WISEPA J165311.05 + 444423.9		T8	0.5	33	—	—	25	...	25	38
WISEPA J171104.60 + 350036.8	B	T8	0.5	20	—	—	25	31	25	38
			0.8	34	—	—	25	31	25	31
WISEPA J174124.26 + 255319.5		T9	0.8	106	2017-03-15	HD 165029	25,28	...	25	40
WISE J180901.07 + 383805.4		T7.5	0.8	27	—	—	30	...	34	38
WISE J181329.40 + 283533.3		T8	0.5	46	2017-06-27	HD 174567	34	...	34	40
WISEPA J185215.78 + 353716.3		T7	0.5	115	2011-04-20	HD 165029	25	...	25	40
WISEPA J195905.66 — 333833.7		T8	0.5	38	2017-06-13	HD 194982	25	...	25	40
WISE J200050.19 + 362950.1		T8	0.5	67	2017-06-13	HD 191225	36	...	36	40
WISEPC J215751.38 + 265931.4		T7	0.8	70	2017-07-10	HD 210290	25	...	25	40
WISEPC J220922.10 — 273439.5		T7	0.8	64	2017-07-19	HD 202025	25	...	25	40
WISEPC J221354.69 + 091139.4		T7	0.5	74	—	—	25	...	25	38
WISEPC J222623.05 + 044003.9		T8	0.5	69	—	—	25	...	25	38
WISEPC J225540.74 — 311841.8		T8	0.5	43	—	—	25	...	25	38
WISEPC J231939.13 — 184404.3		T7.5	0.5	26	—	—	25	...	25	38
ULAS J232123.79 + 135454.9		T7.5	0.8	45	2017-07-19	HD 210501	20	...	15	40
WISEPC J234026.62 — 074507.2	B?	T7	0.5	99	—	—	25	...	25	38
WISEPC J234841.10 — 102844.4		T7	0.5	71	—	—	25	...	25	38

^a “B”: Resolved binaries; “B?”: Binarity is likely but not confirmed (Section 4.2); “C”: Companions to stars or brown dwarfs. Remaining objects are single field dwarfs.

^b Signal-to-noise ratio around the J -band peak ($1.2 - 1.3 \mu\text{m}$) of the object’s spectra.

^c For spectra taken from our own observations, we show the observation date and the A0V telluric standard star.

References—(1) Burgasser et al. (1999), (2) Burgasser et al. (2000), (3) Burgasser et al. (2002), (4) Burgasser et al. (2004), (5) Tinney et al. (2005), (6) Burgasser et al. (2006b), (7) Burgasser et al. (2006c), (8) Burgasser et al. (2006a), (9) Chiu et al. (2006), (10) Mugrauer et al. (2006), (11) Burgasser (2007), (12) Luhman et al. (2007), (13) Looper et al. (2007), (14) Burgasser et al. (2010b), (15) Burningham et al. (2010a), (16) Burgasser et al. (2010a), (17) Burningham et al. (2010b), (18) Goldman et al. (2010), (19) Lucas et al. (2010), (20) Scholz (2010b), (21) Scholz (2010a), (22) Burningham et al. (2011), (23) Cushing et al. (2011), (24) Gelino et al. (2011), (25) Kirkpatrick et al. (2011), (26) Liu et al. (2011b), (27) Mainzer et al. (2011), (28) Scholz et al. (2011), (29) Kirkpatrick et al. (2012), (30) Luhman et al. (2012), (31) Liu et al. (2012), (32) Burningham et al. (2013), (33) Bihain et al. (2013), (34) Mace et al. (2013a), (35) Thompson et al. (2013), (36) Cushing et al. (2014), (37) Best et al. (2015), (38) Burgasser & Splat Development Team (2017), (39) Tinney et al. (2018), (40) This work

Table 2. Sample of T7–T9 Dwarfs: Astrometry

Object	Type ^a	SpT	R.A. ^b (hh:mm:ss.ss)	Decl. ^b (dd:mm:ss.s)	$\mu_{\alpha} \cos \delta$ (mas yr ⁻¹)	μ_{δ} (mas yr ⁻¹)	Parallax (mas)	References
HD 3651B	C	T7.5	00:39:18.91	21:15:16.8	-462.06 ± 0.11	-369.81 ± 0.06	89.79 ± 0.06	6,7
WISE J004024.88 + 090054.8		T7	00:40:24.89	09:00:54.5	-53.90 ± 2.80	-62.60 ± 2.30	71.40 ± 2.70	9
WISE J004945.61 + 215120.0		T8.5	00:49:45.65	21:51:19.7	-483.20 ± 1.40	-46.50 ± 1.40	139.90 ± 2.50	8
2MASS J00501994 – 3322402		T7	00:50:21.05	–33:22:28.9	1150.50 ± 2.20	939.10 ± 2.10	94.60 ± 2.40	3
WISEPA J012333.21 + 414203.9		T7	01:23:33.25	41:42:03.9	601.10 ± 1.30	88.80 ± 1.30	39.40 ± 2.40	9
WISEPC J022322.39 – 293258.1		T7.5	02:23:22.38	–29:32:57.3	780.20 ± 1.10	-535.10 ± 1.50	80.70 ± 2.60	8
WISE J024124.73 – 365328.0		T7	02:41:24.75	–36:53:28.1	242.00 ± 1.50	148.40 ± 1.40	52.40 ± 2.70	8
WISE J024512.62 – 345047.8		T8	02:45:12.62	–34:50:47.8	–	–	–	...
PSO J043.5395 + 02.3995		T8	02:54:09.56	02:23:58.6	2562.61 ± 0.15	221.95 ± 1.34	146.10 ± 1.50	8
WISE J032547.72 + 083118.2		T7	03:25:47.73	08:31:18.2	116.20 ± 1.80	-38.10 ± 1.70	78.50 ± 3.00	8
2MASS J0415195 – 093506		T8	04:15:21.27	–09:35:00.4	2214.30 ± 1.20	535.90 ± 1.20	175.20 ± 1.70	3
WISEPA J045853.89 + 643452.9	B	T8.5	04:58:53.91	64:34:52.6	207.70 ± 1.20	291.20 ± 1.20	109.20 ± 3.60	8
WISEPA J050003.05 – 122343.2		T8	05:00:03.04	–12:23:43.2	-533.70 ± 1.70	490.50 ± 1.80	84.60 ± 2.20	9
WISE J052126.29 + 102528.4		T7.5	05:21:26.31	10:25:28.4	215.50 ± 5.60	-418.30 ± 2.80	141.50 ± 5.10	9
UGPS J052127.27 + 364048.6		T8.5	05:21:27.42	36:40:43.6	569.00 ± 0.90	-1511.00 ± 1.00	122.20 ± 1.60	8
WISE J061437.73 + 095135.0		T7	06:14:37.75	09:51:35.2	387.50 ± 1.70	-156.30 ± 1.50	56.80 ± 2.00	9
WISEPA J062309.94 – 045624.6		T8	06:23:09.93	–04:56:24.5	-906.30 ± 1.80	168.80 ± 1.60	86.50 ± 1.70	9
UGPS J072227.51 – 054031.2		T9	07:22:27.28	–05:40:29.8	-904.14 ± 1.71	352.03 ± 1.21	242.80 ± 2.40	5
2MASS J0727182 + 171001		T7	07:27:19.16	17:09:51.3	1045.50 ± 1.10	-763.70 ± 1.00	112.50 ± 0.90	3
2MASS J07290002 – 3954043		T8 pec	07:28:59.50	–39:53:45.4	-566.60 ± 5.30	1643.40 ± 5.50	126.30 ± 8.30	4
2MASS J09393548 – 2448279		T8	09:39:35.93	–24:48:39.0	573.40 ± 2.30	-1044.70 ± 2.50	187.30 ± 4.60	2
ULAS J102940.52 + 093514.6		T8	10:29:40.52	09:35:14.1	-419.40 ± 2.00	-142.60 ± 1.80	68.50 ± 1.70	9
WISE J103907.73 – 160002.9	B?	T7.5	10:39:07.74	–16:00:03.0	-197.60 ± 2.20	-120.30 ± 2.30	45.20 ± 1.90	9
WISE J105257.95 – 194250.2		T7.5	10:52:57.95	–19:42:50.2	317.90 ± 2.20	-314.90 ± 2.00	67.90 ± 2.20	9
2MASS J11145133 – 2618235		T7.5	11:14:48.75	–26:18:27.9	-3021.50 ± 1.80	-389.50 ± 2.10	179.20 ± 1.40	3
WISE J112438.12 – 042149.7		T7	11:24:38.11	–04:21:49.6	-569.10 ± 2.40	68.90 ± 3.00	57.50 ± 3.40	9
2MASS J1217110 – 031113		T7.5	12:17:10.28	–03:11:12.2	-1054.39 ± 1.70	75.58 ± 1.84	91.70 ± 2.20	1,8
WISE J125448.52 – 072828.4		T7	12:54:48.51	–07:28:28.3	1.40 ± 2.70	-133.80 ± 2.90	41.30 ± 2.70	9
WISE J125715.90 + 400854.2		T7	12:57:15.92	40:08:54.2	294.90 ± 1.60	167.90 ± 1.40	57.10 ± 1.80	9
Ross 458C	C	T8	13:00:41.64	12:21:14.6	-632.15 ± 0.50	-36.02 ± 0.19	86.86 ± 0.15	6,7
WISEPA J132233.66 – 234017.1		T8	13:22:33.63	–23:40:17.1	-348.31 ± 1.47	391.62 ± 1.57	77.50 ± 4.20	8
ULAS J141623.94 + 134836.3	C	(sd) T7.5	14:16:23.97	13:48:36.1	85.69 ± 0.69	129.07 ± 0.47	107.56 ± 0.30	6,7
WISEPC J145715.03 + 581510.2		T7	14:57:15.02	58:15:10.2	-488.60 ± 4.90	-65.80 ± 4.90	46.70 ± 5.70	9
GJ 570D	C	T7.5	14:57:15.84	–21:22:08.1	1031.40 ± 0.17	-1723.65 ± 0.13	170.01 ± 0.09	6,7

Table 2 continued

Table 2 (*continued*)

Object	Type ^a	SpT	R.A. ^b (hh:mm:ss.ss)	Decl. ^b (dd:mm:ss.s)	$\mu_{\alpha} \cos \delta$ (mas yr ⁻¹)	μ_{δ} (mas yr ⁻¹)	Parallax (mas)	References
PSO J224.3820 + 47.4057		T7	14:57:31.68	47:24:20.2	139.80 ± 3.00	-84.50 ± 2.30	49.50 ± 3.00	9
SDSS J150411.63 + 102718.4	B?	T7	15:04:11.81	10:27:15.4	373.60 ± 1.90	-369.20 ± 2.10	46.10 ± 1.50	3
2MASSI J1553022 + 153236	B	T7	15:53:01.93	15:32:38.8	-385.90 ± 0.70	166.20 ± 0.90	75.10 ± 0.90	3
SDSS J162838.77 + 230821.1		T7	16:28:38.99	23:08:17.9	412.30 ± 0.80	-443.00 ± 0.70	75.10 ± 0.90	3
WISEPA J165311.05 + 444423.9		T8	16:53:11.03	44:44:22.7	-76.00 ± 1.90	-398.20 ± 2.40	75.70 ± 1.90	9
WISEPA J171104.60 + 350036.8	B	T8	17:11:04.59	35:00:36.8	-156.30 ± 1.10	-71.20 ± 1.20	40.30 ± 2.40	8
WISEPA J174124.26 + 255319.5		T9	17:41:24.23	25:53:19.2	-505.34 ± 1.11	-1472.61 ± 1.28	214.30 ± 2.80	8
WISE J180901.07 + 383805.4		T7.5	18:09:01.07	38:38:05.2	-590.70 ± 2.60	-506.70 ± 2.30	52.30 ± 2.30	9
WISE J181329.40 + 283533.3		T8	18:13:29.40	28:35:33.3	-208.90 ± 2.10	-468.10 ± 2.90	73.60 ± 2.00	9
WISEPA J185215.78 + 353716.3		T7	18:52:15.82	35:37:16.2	254.40 ± 3.00	-288.00 ± 3.00	66.40 ± 2.90	9
WISEPA J195905.66 - 333833.7		T8	19:59:05.65	-33:38:33.8	-8.60 ± 1.00	-193.20 ± 1.10	85.30 ± 2.20	8
WISE J200050.19 + 362950.1		T8	20:00:50.19	36:29:50.1	2.20 ± 3.30	368.30 ± 4.20	131.20 ± 2.90	9
WISEPC J215751.38 + 265931.4		T7	21:57:51.35	26:59:31.3	65.80 ± 1.30	-100.50 ± 1.60	62.80 ± 2.20	9
WISEPC J220922.10 - 273439.5		T7	22:09:22.09	-27:34:39.9	-765.10 ± 2.00	-440.90 ± 2.20	72.40 ± 3.80	9
WISEPC J221354.69 + 091139.4		T7	22:13:54.70	09:11:39.4	-116.20 ± 1.50	-35.40 ± 1.80	52.10 ± 3.10	9
WISEPC J222623.05 + 044003.9		T8	22:26:23.06	04:40:03.3	-283.17 ± 3.83	-463.55 ± 5.08	54.40 ± 5.90	8
WISEPC J225540.74 - 311841.8		T8	22:55:40.76	-31:18:42.0	300.20 ± 1.50	-162.10 ± 2.20	70.70 ± 4.20	8
WISEPC J231939.13 - 184404.3		T7.5	23:19:39.15	-18:44:04.4	74.00 ± 1.40	131.20 ± 1.40	85.10 ± 3.10	9
ULAS J232123.79 + 135454.9		T7.5	23:21:23.83	13:54:53.3	78.70 ± 1.20	-561.60 ± 1.40	83.60 ± 2.40	8
WISEPC J234026.62 - 074507.2	B?	T7	23:40:26.62	-07:45:08.5	152.80 ± 0.95	-250.12 ± 1.25	47.80 ± 3.10	8
WISEPC J234841.10 - 102844.4		T7	23:48:41.12	-10:28:44.1	620.80 ± 2.10	146.20 ± 1.90	67.60 ± 3.80	9

^a “B”: Resolved binaries; “B?”: Binarity is likely but not confirmed (Section 4.2); “C”: Companions to stars or brown dwarfs. Remaining objects are single field dwarfs.

^b Coordinates are provided at epoch J2000 with equinox J2000.

References—(1) [Tinney et al. \(2003\)](#), (2) [Burgasser et al. \(2008b\)](#), (3) [Dupuy & Liu \(2012\)](#), (4) [Faherty et al. \(2012\)](#), (5) [Leggett et al. \(2012\)](#), (6) [Gaia Collaboration et al. \(2016a\)](#), (7) [Gaia Collaboration et al. \(2018\)](#), (8) [Kirkpatrick et al. \(2019\)](#), (9) [Best et al. \(2020a\)](#)

Table 3. Sample of T7–T9 Dwarfs: Photometry

Object	Type ^a	SpT	Near-Infrared MKO Photometry					AllWISE Photometry			Spitzer/IRAC Photometry		
			Y_{MKO} (mag)	J_{MKO} (mag)	H_{MKO} (mag)	K_{MKO} (mag)	References	W1 (mag)	W2 (mag)	References	[3.6] (mag)	[4.5] (mag)	References
HD 3651B	C	T7.5	17.12 ± 0.06	16.16 ± 0.03	16.68 ± 0.04	16.87 ± 0.05	4,26	–	–	...	15.38 ± 0.04	13.62 ± 0.02	8
WISE J004024.88 + 090054.8		T7	17.15 ± 0.02	16.13 ± 0.01	16.56 ± 0.02	16.55 ± 0.05	12	15.99 ± 0.06	13.83 ± 0.05	19	15.07 ± 0.02	13.76 ± 0.02	17
WISE J004945.61 + 215120.0		T8.5	17.29 ± 0.17	16.44 ± 0.16	16.72 ± 0.02	16.80 ± 0.17	24,26	15.92 ± 0.06	13.03 ± 0.03	19	15.01 ± 0.02	13.04 ± 0.02	17
2MASS J00501994 – 3322402		T7	16.85 ± 0.10	15.65 ± 0.10	16.04 ± 0.10	15.91 ± 0.10	8	15.60 ± 0.04	13.58 ± 0.03	19	14.87 ± 0.02	13.59 ± 0.02	24
WISEPA J012333.21 + 414203.9		T7	18.10 ± 0.05	16.99 ± 0.02	17.25 ± 0.05	17.25 ± 0.06	25,26	16.84 ± 0.08	14.95 ± 0.07	19	16.12 ± 0.03	14.84 ± 0.02	24
WISEPC J022322.39 – 293258.1		T7.5	18.08 ± 0.07	17.10 ± 0.05	17.30 ± 0.11	17.59 ± 0.08	10,26	16.87 ± 0.08	14.02 ± 0.04	19	15.81 ± 0.03	14.01 ± 0.02	10
WISE J024124.73 – 365328.0 ^b		T7	17.73 ± 0.05	16.72 ± 0.01	17.04 ± 0.07	17.27 ± 0.05	16,24,27	16.86 ± 0.08	14.35 ± 0.04	19	15.74 ± 0.03	14.35 ± 0.02	24
WISE J024512.62 – 345047.8		T8	18.65 ± 0.11	17.77 ± 0.09	18.27 ± 0.10	18.05 ± 0.11	17,26	17.03 ± 0.10	14.50 ± 0.05	19	16.05 ± 0.03	14.59 ± 0.02	17
PSO J043.5395 + 02.3995		T8	17.00 ± 0.01	15.92 ± 0.01	16.29 ± 0.02	16.73 ± 0.05	12	15.81 ± 0.05	12.76 ± 0.03	19	14.69 ± 0.02	12.70 ± 0.02	10
WISE J032547.72 + 083118.2		T7	17.14 ± 0.09	16.29 ± 0.07	16.19 ± 0.08	16.39 ± 0.09	26	15.35 ± 0.04	13.53 ± 0.03	19	14.70 ± 0.02	13.59 ± 0.02	17
2MASS J0415195 – 093506		T8	16.39 ± 0.06	15.32 ± 0.03	15.70 ± 0.03	15.83 ± 0.03	2,26	15.14 ± 0.04	12.29 ± 0.03	19	14.26 ± 0.02	12.37 ± 0.02	24
WISEPA J045853.89 + 643452.9	B	T8.5	18.02 ± 0.09	17.13 ± 0.07	17.45 ± 0.11	17.74 ± 0.10	9,26	16.44 ± 0.07	13.02 ± 0.03	19	15.08 ± 0.02	12.98 ± 0.02	10
WISEPA J050003.05 – 122343.2		T8	18.69 ± 0.07	17.88 ± 0.02	18.13 ± 0.12	18.07 ± 0.08	12,26	17.45 ± 0.15	13.98 ± 0.04	19	15.95 ± 0.03	14.00 ± 0.02	10
WISE J052126.29 + 102528.4		T7.5	15.71 ± 0.05	14.87 ± 0.02	15.27 ± 0.05	15.00 ± 0.05	25,26	14.11 ± 0.03	12.29 ± 0.02	19	–	–	...
UGPS J052127.27 + 364048.6 ^b		T8.5	18.08 ± 0.05	16.94 ± 0.02	17.28 ± 0.04	17.32 ± 0.09	13,27	14.40 ± 0.03	13.00 ± 0.03	19	14.94 ± 0.02	13.58 ± 0.02	24
WISE J061437.73 + 095135.0		T7	17.54 ± 0.05	16.44 ± 0.02	16.66 ± 0.05	16.51 ± 0.05	25,26	16.62 ± 0.11	14.24 ± 0.05	19	15.48 ± 0.03	14.09 ± 0.02	17
WISEPA J062309.94 – 045624.6		T8	18.04 ± 0.06	17.10 ± 0.02	17.34 ± 0.07	17.27 ± 0.09	25,26	16.84 ± 0.09	13.81 ± 0.04	19	15.49 ± 0.03	13.74 ± 0.02	10
UGPS J072227.51 – 054031.2		T9	17.37 ± 0.02	16.52 ± 0.01	16.90 ± 0.02	17.07 ± 0.08	7	15.25 ± 0.05	12.20 ± 0.02	19	14.30 ± 0.02	12.22 ± 0.02	24
2MASS J0727182 + 171001		T7	16.16 ± 0.06	15.19 ± 0.03	15.67 ± 0.03	15.69 ± 0.03	2,11	15.19 ± 0.04	12.96 ± 0.03	19	14.46 ± 0.02	13.02 ± 0.02	24
2MASS J07290002 – 3954043		T8 pec	16.60 ± 0.09	15.66 ± 0.08	16.05 ± 0.10	16.50 ± 0.10	26	15.29 ± 0.03	12.97 ± 0.02	19	14.47 ± 0.01	12.95 ± 0.01	23
2MASS J09393548 – 2448279		T8	16.47 ± 0.09	15.61 ± 0.09	15.96 ± 0.09	16.83 ± 0.09	5	14.91 ± 0.03	11.64 ± 0.02	19	13.77 ± 0.02	11.62 ± 0.02	24
ULAS J102940.52 + 093514.6		T8	18.24 ± 0.02	17.28 ± 0.01	17.63 ± 0.01	17.64 ± 0.02	14	16.78 ± 0.12	14.38 ± 0.07	19	16.08 ± 0.03	14.46 ± 0.02	18
WISE J103907.73 – 160002.9	B?	T7.5	18.19 ± 0.03	16.89 ± 0.02	17.19 ± 0.04	17.09 ± 0.07	16,26	16.48 ± 0.07	14.18 ± 0.05	19	15.87 ± 0.03	14.21 ± 0.02	24
WISE J105257.95 – 194250.2		T7.5	17.72 ± 0.05	16.83 ± 0.02	17.08 ± 0.05	17.00 ± 0.05	25,26	16.58 ± 0.08	14.11 ± 0.04	19	15.66 ± 0.03	14.22 ± 0.02	18
2MASS J11145133 – 2618235		T7.5	16.36 ± 0.05	15.52 ± 0.05	15.82 ± 0.05	16.54 ± 0.05	8	15.25 ± 0.04	12.27 ± 0.02	19	14.19 ± 0.02	12.35 ± 0.02	24
WISE J112438.12 – 042149.7		T7	17.35 ± 0.05	16.37 ± 0.02	16.77 ± 0.05	16.64 ± 0.06	25,26	16.45 ± 0.08	14.05 ± 0.05	19	15.37 ± 0.02	14.10 ± 0.02	17
2MASS J1217110 – 031113		T7.5	16.58 ± 0.03	15.56 ± 0.03	15.98 ± 0.03	15.92 ± 0.03	1	15.27 ± 0.04	13.21 ± 0.03	19	14.75 ± 0.02	13.29 ± 0.02	24
WISE J125448.52 – 072828.4		T7	18.41 ± 0.06	17.30 ± 0.01	17.63 ± 0.03	17.40 ± 0.07	18,26	16.78 ± 0.10	14.85 ± 0.08	19	16.33 ± 0.04	14.82 ± 0.02	18
WISE J125715.90 + 400854.2		T7	18.14 ± 0.06	16.89 ± 0.02	17.14 ± 0.06	17.18 ± 0.06	25,26	16.67 ± 0.08	14.43 ± 0.05	19	15.92 ± 0.03	14.49 ± 0.02	17
Ross 458C	C	T8	17.72 ± 0.03	16.69 ± 0.02	17.01 ± 0.04	16.90 ± 0.06	12	16.04 ± 0.06	13.85 ± 0.04	19	15.28 ± 0.01	13.77 ± 0.01	23
WISEPA J132233.66 – 234017.1		T8	17.74 ± 0.12	16.75 ± 0.11	16.65 ± 0.14	17.02 ± 0.40	26	16.73 ± 0.09	13.96 ± 0.04	19	15.67 ± 0.03	13.89 ± 0.02	10
ULAS J141623.94 + 134836.3	C	(sd) T7.5	18.16 ± 0.03	17.26 ± 0.02	17.58 ± 0.03	18.43 ± 0.09	12,26	15.99 ± 0.19	12.78 ± 0.04	19	14.74 ± 0.02	12.80 ± 0.02	24
WISEPC J145715.03 + 581510.2		T7	17.81 ± 0.06	16.79 ± 0.02	17.14 ± 0.06	17.21 ± 0.06	25,26	16.66 ± 0.06	14.42 ± 0.04	19	15.85 ± 0.03	14.44 ± 0.02	24

Table 3 continued

Table 3 (continued)

Object	Type ^a	SpT	Near-Infrared MKO Photometry					AllWISE Photometry			Spitzer/IRAC Photometry		
			Y_{MKO} (mag)	J_{MKO} (mag)	H_{MKO} (mag)	K_{MKO} (mag)	References	W1 (mag)	W2 (mag)	References	[3.6] (mag)	[4.5] (mag)	References
GJ 570D	C	T7.5	15.78 ± 0.10	14.82 ± 0.05	15.28 ± 0.05	15.52 ± 0.05	8	14.93 ± 0.04	12.13 ± 0.02	19	13.88 ± 0.02	12.15 ± 0.02	24
PSO J224.3820 + 47.4057		T7	18.01 ± 0.06	17.11 ± 0.02	17.43 ± 0.06	17.08 ± 0.06	21,25,26	16.62 ± 0.06	14.65 ± 0.04	19	–	–	...
SDSS J150411.63 + 102718.4	B?	T7	17.63 ± 0.02	16.51 ± 0.01	16.99 ± 0.05	17.12 ± 0.08	12	16.22 ± 0.06	14.06 ± 0.04	19	15.50 ± 0.03	14.06 ± 0.02	24
2MASS J1553022 + 153236	B	T7	16.37 ± 0.06	15.34 ± 0.03	15.76 ± 0.03	15.94 ± 0.03	2	15.29 ± 0.04	13.03 ± 0.03	19	14.51 ± 0.02	13.13 ± 0.02	24
SDSS J162838.77 + 230821.1		T7	17.27 ± 0.03	16.25 ± 0.03	16.63 ± 0.03	16.72 ± 0.03	3	16.27 ± 0.05	13.92 ± 0.04	19	15.44 ± 0.03	13.94 ± 0.02	24
WISEPA J165311.05 + 444423.9		T8	18.11 ± 0.06	17.08 ± 0.02	17.60 ± 0.05	17.07 ± 0.06	25,26	16.49 ± 0.05	13.82 ± 0.03	19	15.67 ± 0.03	13.87 ± 0.02	10
WISEPA J171104.60 + 350036.8	B	T8	18.55 ± 0.14	17.63 ± 0.13	18.06 ± 0.14	18.10 ± 0.14	26	17.80 ± 0.16	14.63 ± 0.04	19	16.46 ± 0.04	14.62 ± 0.02	10
WISEPA J174124.26 + 255319.5		T9	17.10 ± 0.05	16.18 ± 0.02	16.31 ± 0.04	17.02 ± 0.20	15,26	15.30 ± 0.04	12.35 ± 0.02	19	14.43 ± 0.02	12.39 ± 0.02	10
WISE J180901.07 + 383805.4		T7.5	18.23 ± 0.06	17.39 ± 0.02	17.70 ± 0.06	17.32 ± 0.07	25,26	17.59 ± 0.13	14.98 ± 0.06	19	16.49 ± 0.04	14.90 ± 0.02	17
WISE J181329.40 + 283533.3		T8	17.86 ± 0.05	16.91 ± 0.02	17.11 ± 0.06	16.93 ± 0.06	25,26	15.58 ± 0.04	14.04 ± 0.04	19	15.82 ± 0.03	14.19 ± 0.02	17
WISEPA J185215.78 + 353716.3		T7	17.41 ± 0.05	16.32 ± 0.02	16.73 ± 0.06	16.52 ± 0.06	25,26	15.95 ± 0.05	14.14 ± 0.04	19	15.58 ± 0.03	14.19 ± 0.02	10
WISEPA J195905.66 – 333833.7		T8	17.67 ± 0.09	16.71 ± 0.07	17.18 ± 0.05	16.93 ± 0.09	10,26	16.15 ± 0.06	13.84 ± 0.04	19	15.36 ± 0.02	13.79 ± 0.02	17
WISE J200050.19 + 362950.1		T8	16.31 ± 0.05	15.44 ± 0.01	15.85 ± 0.01	16.13 ± 0.04	13,20,26	15.08 ± 0.06	12.69 ± 0.03	19	14.22 ± 0.02	12.68 ± 0.02	23
WISEPC J215751.38 + 265931.4		T7	18.00 ± 0.05	17.04 ± 0.02	17.49 ± 0.04	17.35 ± 0.06	25,26	16.99 ± 0.11	14.49 ± 0.05	19	16.01 ± 0.03	14.44 ± 0.02	10
WISEPC J220922.10 – 273439.5		T7	17.53 ± 0.05	16.55 ± 0.02	16.91 ± 0.06	17.31 ± 0.06	25,26	16.31 ± 0.08	13.86 ± 0.04	19	15.48 ± 0.03	13.90 ± 0.02	10
WISEPC J221354.69 + 091139.4		T7	17.81 ± 0.05	16.76 ± 0.02	17.11 ± 0.06	17.12 ± 0.06	25,26	16.58 ± 0.08	14.65 ± 0.06	19	15.79 ± 0.03	14.56 ± 0.02	10
WISEPC J222623.05 + 044003.9		T8	18.04 ± 0.03	16.90 ± 0.02	17.45 ± 0.07	17.24 ± 0.09	12	16.86 ± 0.11	14.51 ± 0.06	19	16.12 ± 0.03	14.54 ± 0.02	10
WISEPC J225540.74 – 311841.8		T8	18.38 ± 0.02	17.33 ± 0.01	17.66 ± 0.03	17.42 ± 0.05	22,26	16.55 ± 0.08	14.16 ± 0.05	19	15.91 ± 0.03	14.21 ± 0.02	10
WISEPC J231939.13 – 184404.3		T7.5	18.56 ± 0.06	17.56 ± 0.02	17.95 ± 0.05	18.27 ± 0.08	10,26	16.67 ± 0.09	13.82 ± 0.04	19	15.92 ± 0.03	13.95 ± 0.02	10
ULAS J232123.79 + 135454.9		T7.5	17.92 ± 0.03	16.72 ± 0.03	17.15 ± 0.03	17.16 ± 0.01	6	16.94 ± 0.12	14.11 ± 0.06	19	15.86 ± 0.03	14.19 ± 0.02	24
WISEPC J234026.62 – 074507.2	B?	T7	17.20 ± 0.06	16.08 ± 0.03	16.41 ± 0.04	16.51 ± 0.06	26	15.93 ± 0.06	13.60 ± 0.04	19	15.19 ± 0.02	13.62 ± 0.02	10
WISEPC J234841.10 – 102844.4		T7	17.69 ± 0.05	16.62 ± 0.02	16.99 ± 0.06	16.84 ± 0.06	25,26	16.65 ± 0.09	14.38 ± 0.05	19	15.87 ± 0.03	14.36 ± 0.02	10

^a “B”: Resolved binaries; “B?”: Binarity is likely but not confirmed (Section 4.2); “C”: Companions to stars or brown dwarfs. Remaining objects are single field dwarfs.

^b We calculate synthetic photometry for WISE J024124.73 – 365328.0 (Y_{MKO} and K_{MKO}) and UGPS J052127.27 + 364048.6 (Y_{MKO}) using their SpeX prism spectra and the approach described in Best et al. (2021).

References—(1) Leggett et al. (2002), (2) Knapp et al. (2004), (3) Chiu et al. (2006), (4) Luhman et al. (2007), (5) Leggett et al. (2009), (6) Burningham et al. (2010a), (7) Lucas et al. (2010), (8) Leggett et al. (2010), (9) Gelino et al. (2011), (10) Kirkpatrick et al. (2011), (11) Dupuy & Liu (2012), (12) Lawrence et al. (2012), (13) UKIDSS Consortium (2012), (14) Burningham et al. (2013), (15) Dupuy & Kraus (2013), (16) McMahon et al. (2013), (17) Mace et al. (2013a), (18) Thompson et al. (2013), (19) Cutri & et al. (2014), (20) Cushing et al. (2014), (21) Best et al. (2015), (22) Edge et al. (2016), (23) Leggett et al. (2017), (24) Kirkpatrick et al. (2019), (25) Best et al. (2020a), (26) Best et al. (2021), (27) This work

Table 4. Starfish-Based Forward-Modeling Analysis: Fitted parameters of T7–T9 Dwarfs

Object	Slit ($''$)	T_{eff} (K)	$\log g$ (dex)	Z (dex)	v_r (km s $^{-1}$)	$v \sin i$ (km s $^{-1}$)	$\log \Omega$ (dex)	a_N	$\log a_G$ (dex)	ℓ (km s $^{-1}$)	additive $\log \Omega$ systematics ^a	
											J band (dex)	K band (dex)
HD 3651B	0.5 $''$	818 $^{+28}_{-28}$ (19)	3.94 $^{+0.29}_{-0.28}$ (0.20)	−0.22 $^{+0.16}_{-0.16}$ (+0.11) (−0.10)	318 $^{+202}_{-202}$ (95)	27 $^{+27}_{-27}$ (20) (18)	−19.543 $^{+0.072}_{-0.070}$ (0.051) (0.046)	1.06 $^{+0.04}_{-0.04}$	−34.64 $^{+0.11}_{-0.11}$	8114 $^{+751}_{-1015}$	+0.049	−0.029
WISE 0040 + 0900	0.5 $''$	883 $^{+30}_{-30}$ (23) (22)	4.07 $^{+0.30}_{-0.29}$ (0.22) (0.22)	−0.34 $^{+0.15}_{-0.15}$ (+0.09) (−0.09)	398 $^{+199}_{-199}$ (88) (85)	33 $^{+31}_{-33}$ (26) (22)	−19.676 $^{+0.072}_{-0.070}$ (0.052) (0.047)	1.03 $^{+0.04}_{-0.04}$	−34.68 $^{+0.11}_{-0.10}$	8153 $^{+725}_{-1020}$	+0.038	−0.015
WISE 0049 + 2151	0.5 $''$	753 $^{+26}_{-26}$ (16) (16)	3.47 $^{+0.26}_{-0.22}$ (0.19) (0.14)	−0.24 $^{+0.18}_{-0.17}$ (+0.14) (−0.12)	−180 $^{+209}_{-209}$ (107) (110)	15 $^{+15}_{-15}$ (10) (10)	−19.348 $^{+0.069}_{-0.069}$ (0.045) (0.048)	1.04 $^{+0.04}_{-0.04}$	−34.50 $^{+0.12}_{-0.11}$	6848 $^{+1065}_{-907}$	−0.067	−0.016
	0.8 $''$	756 $^{+27}_{-28}$ (19) (19)	3.58 $^{+0.28}_{-0.27}$ (0.21) (0.19)	−0.23 $^{+0.18}_{-0.17}$ (+0.14) (−0.12)	−91 $^{+243}_{-245}$ (166) (168)	16 $^{+17}_{-16}$ (12) (11)	−19.390 $^{+0.073}_{-0.072}$ (0.051) (0.052)	1.05 $^{+0.04}_{-0.04}$	−34.66 $^{+0.08}_{-0.07}$	5454 $^{+90}_{-190}$	−0.035	−0.055
2MASS 0050 − 3322	0.5 $''$	947 $^{+23}_{-24}$ (12) (13)	4.06 $^{+0.26}_{-0.26}$ (0.16) (0.18)	−0.11 $^{+0.15}_{-0.15}$ (+0.09) (−0.08)	665 $^{+204}_{-204}$ (96) (98)	30 $^{+28}_{-30}$ (21) (20)	−19.593 $^{+0.069}_{-0.069}$ (0.026) (0.027)	1.08 $^{+0.05}_{-0.05}$	−34.54 $^{+0.07}_{-0.07}$	1809 $^{+416}_{-288}$	−0.002	+0.007
WISE 0123 + 4142	0.8 $''$	1023 $^{+26}_{-26}$ (17) (17)	4.13 $^{+0.32}_{-0.31}$ (0.25) (0.24)	−0.31 $^{+0.15}_{-0.15}$ (+0.10) (−0.09)	−147 $^{+227}_{-226}$ (140) (142)	32 $^{+32}_{-32}$ (25) (21)	−20.290 $^{+0.064}_{-0.064}$ (0.032) (0.032)	0.83 $^{+0.04}_{-0.04}$	−35.66 $^{+0.08}_{-0.08}$	5246 $^{+238}_{-410}$	−0.004	+0.029
WISE 0223 − 2932	0.5 $''$	787 $^{+31}_{-32}$ (23) (25)	4.15 $^{+0.30}_{-0.29}$ (0.21) (0.21)	−0.33 $^{+0.15}_{-0.15}$ (+0.09) (−0.09)	−387 $^{+211}_{-211}$ (113) (110)	32 $^{+31}_{-32}$ (25) (21)	−19.739 $^{+0.096}_{-0.091}$ (0.069) (0.060)	1.04 $^{+0.04}_{-0.04}$	−35.23 $^{+0.11}_{-0.10}$	8371 $^{+598}_{-989}$	−0.063	+0.020
WISE 0241 − 3653	0.8 $''$	906 $^{+25}_{-25}$ (15) (14)	3.93 $^{+0.26}_{-0.26}$ (0.17) (0.18)	−0.34 $^{+0.14}_{-0.14}$ (+0.07) (−0.07)	−134 $^{+213}_{-212}$ (116) (114)	29 $^{+27}_{-29}$ (20) (19)	−19.927 $^{+0.064}_{-0.065}$ (0.029) (0.030)	0.66 $^{+0.04}_{-0.04}$	−35.50 $^{+0.08}_{-0.08}$	5439 $^{+100}_{-207}$	−0.009	−0.003
WISE 0245 − 3450	0.5 $''$	804 $^{+25}_{-25}$ (15) (15)	3.43 $^{+0.25}_{-0.18}$ (0.16) (0.11)	−0.36 $^{+0.15}_{-0.14}$ (+0.10) (−0.08)	−9 $^{+228}_{-227}$ (144) (139)	152 $^{+104}_{-106}$ (103) (103)	−20.084 $^{+0.074}_{-0.074}$ (0.036) (0.036)	1.00 $^{+0.04}_{-0.04}$	−36.06 $^{+0.14}_{-0.13}$	6579 $^{+1643}_{-1677}$	−0.017	+0.070
PSO J043 + 02	0.5 $''$	798 $^{+28}_{-28}$ (19) (20)	4.15 $^{+0.30}_{-0.30}$ (0.22) (0.22)	−0.11 $^{+0.18}_{-0.17}$ (+0.13) (−0.12)	60 $^{+202}_{-203}$ (94) (93)	30 $^{+29}_{-30}$ (22) (20)	−19.380 $^{+0.074}_{-0.072}$ (0.053) (0.051)	1.02 $^{+0.04}_{-0.04}$	−34.24 $^{+0.10}_{-0.10}$	7984 $^{+798}_{-912}$	+0.017	−0.059
WISE 0325 + 0831	0.5 $''$	873 $^{+28}_{-27}$ (19) (19)	3.42 $^{+0.25}_{-0.17}$ (0.18) (0.10)	−0.13 $^{+0.22}_{-0.20}$ (+0.20) (−0.15)	−248 $^{+202}_{-201}$ (93) (91)	17 $^{+17}_{-17}$ (11) (11)	−19.493 $^{+0.072}_{-0.071}$ (0.043) (0.038)	1.06 $^{+0.04}_{-0.04}$	−34.35 $^{+0.11}_{-0.11}$	8482 $^{+512}_{-819}$	−0.156	−0.122
2MASS 0415 − 0935	0.5 $''$	793 $^{+28}_{-28}$ (19) (20)	4.07 $^{+0.28}_{-0.28}$ (0.20) (0.20)	−0.13 $^{+0.18}_{-0.18}$ (+0.14) (−0.13)	180 $^{+195}_{-195}$ (76) (76)	29 $^{+28}_{-29}$ (22) (19)	−19.135 $^{+0.074}_{-0.072}$ (0.051) (0.051)	1.06 $^{+0.04}_{-0.04}$	−33.75 $^{+0.09}_{-0.10}$	8227 $^{+644}_{-797}$	+0.032	+0.001
WISE 0458 + 6434	0.5 $''$	743 $^{+32}_{-33}$ (25) (27)	3.91 $^{+0.36}_{-0.34}$ (0.30) (0.27)	−0.32 $^{+0.19}_{-0.17}$ (+0.15) (−0.11)	1121 $^{+256}_{-257}$ (186) (183)	23 $^{+25}_{-23}$ (19) (15)	−19.651 $^{+0.101}_{-0.096}$ (0.076) (0.071)	1.02 $^{+0.04}_{-0.04}$	−34.93 $^{+0.11}_{-0.11}$	8234 $^{+683}_{-1008}$	−0.019	+0.194
WISE 0500 − 1223	0.5 $''$	727 $^{+46}_{-53}$ (40) (49)	4.13 $^{+0.43}_{-0.41}$ (0.36) (0.34)	−0.38 $^{+0.17}_{-0.12}$ (+0.13) (−0.08)	242 $^{+324}_{-326}$ (275) (267)	28 $^{+34}_{-28}$ (28) (18)	−19.910 $^{+0.182}_{-0.138}$ (0.168) (0.112)	1.07 $^{+0.04}_{-0.04}$	−35.50 $^{+0.14}_{-0.13}$	8045 $^{+819}_{-1273}$	−0.018	+0.217
WISE 0521 + 1025	0.8 $''$	846 $^{+25}_{-24}$ (15) (14)	3.36 $^{+0.22}_{-0.11}$ (0.11) (0.06)	−0.29 $^{+0.16}_{-0.15}$ (+0.10) (−0.09)	184 $^{+220}_{-220}$ (128) (128)	15 $^{+16}_{-15}$ (10) (10)	−19.003 $^{+0.064}_{-0.064}$ (0.031) (0.034)	0.90 $^{+0.04}_{-0.04}$	−33.80 $^{+0.07}_{-0.07}$	5482 $^{+70}_{-148}$	−0.005	+0.026
UGPS 0521 + 3640	0.8 $''$	781 $^{+29}_{-29}$ (22) (21)	4.50 $^{+0.30}_{-0.30}$ (0.22) (0.22)	0.23 $^{+0.18}_{-0.19}$ (0.15) (0.15)	165 $^{+255}_{-257}$ (182) (181)	39 $^{+35}_{-39}$ (30) (26)	−19.783 $^{+0.077}_{-0.075}$ (0.058) (0.051)	0.75 $^{+0.04}_{-0.04}$	−35.11 $^{+0.07}_{-0.07}$	5481 $^{+70}_{-145}$	+0.049	+0.073
WISE 0614 + 0951	0.8 $''$	956 $^{+26}_{-26}$ (17) (17)	4.21 $^{+0.28}_{-0.29}$ (0.20) (0.20)	−0.01 $^{+0.17}_{-0.17}$ (+0.13) (−0.11)	743 $^{+217}_{-218}$ (123) (124)	37 $^{+34}_{-37}$ (29) (25)	−19.902 $^{+0.064}_{-0.065}$ (0.033) (0.034)	0.93 $^{+0.04}_{-0.04}$	−35.06 $^{+0.07}_{-0.07}$	5470 $^{+79}_{-169}$	−0.003	+0.029
WISE 0623 − 0456	0.5 $''$	743 $^{+53}_{-51}$ (49) (47)	4.70 $^{+0.47}_{-0.42}$ (0.44) (0.36)	−0.32 $^{+0.18}_{-0.16}$ (+0.15) (−0.11)	167 $^{+303}_{-301}$ (243) (245)	60 $^{+70}_{-55}$ (69) (40)	−19.610 $^{+0.167}_{-0.156}$ (0.158) (0.145)	1.06 $^{+0.04}_{-0.04}$	−34.98 $^{+0.14}_{-0.14}$	7939 $^{+895}_{-1365}$	−0.056	+0.116
UGPS 0722 − 0540	0.5 $''$	680 $^{+26}_{-26}$ (16) (17)	3.60 $^{+0.30}_{-0.28}$ (0.24) (0.21)	−0.06 $^{+0.21}_{-0.20}$ (+0.17) (−0.16)	28 $^{+204}_{-204}$ (96) (98)	14 $^{+15}_{-14}$ (10) (9)	−19.225 $^{+0.075}_{-0.072}$ (0.056) (0.048)	0.99 $^{+0.04}_{-0.04}$	−34.40 $^{+0.08}_{-0.08}$	8744 $^{+329}_{-599}$	+0.031	−0.040
2MASS 0727 + 1710	0.5 $''$	896 $^{+26}_{-26}$ (17) (17)	3.93 $^{+0.25}_{-0.25}$ (0.15) (0.16)	−0.22 $^{+0.14}_{-0.14}$ (+0.07) (−0.07)	−0 $^{+203}_{-203}$ (95) (96)	27 $^{+26}_{-27}$ (20) (18)	−19.326 $^{+0.063}_{-0.063}$ (0.035) (0.037)	1.07 $^{+0.05}_{-0.05}$	−34.19 $^{+0.09}_{-0.08}$	3206 $^{+447}_{-366}$	+0.027	−0.029
2MASS 0729 − 3954	0.5 $''$	806 $^{+41}_{-42}$ (36) (38)	4.51 $^{+0.32}_{-0.34}$ (0.24) (0.28)	−0.40 $^{+0.14}_{-0.10}$ (+0.09) (−0.06)	197 $^{+225}_{-222}$ (137) (131)	50 $^{+48}_{-50}$ (46) (34)	−19.263 $^{+0.124}_{-0.113}$ (0.110) (0.093)	1.04 $^{+0.04}_{-0.04}$	−34.10 $^{+0.12}_{-0.11}$	7538 $^{+1048}_{-1128}$	−0.004	+0.075
2MASS 0939 − 2448	0.5 $''$	656 $^{+41}_{-34}$ (35) (28)	4.74 $^{+0.33}_{-0.30}$ (0.27) (0.20)	−0.41 $^{+0.15}_{-0.09}$ (+0.11) (−0.06)	84 $^{+243}_{-238}$ (165) (155)	74 $^{+63}_{-61}$ (62) (50)	−18.749 $^{+0.129}_{-0.152}$ (0.109) (0.138)	1.11 $^{+0.05}_{-0.04}$	−33.97 $^{+0.09}_{-0.08}$	3623 $^{+460}_{-381}$	−0.000	+0.010
ULAS 1029 + 0935	0.5 $''$	794 $^{+26}_{-26}$ (17) (17)	3.61 $^{+0.30}_{-0.28}$ (0.23) (0.20)	−0.24 $^{+0.19}_{-0.18}$ (+0.15) (−0.13)	287 $^{+214}_{-214}$ (118) (119)	19 $^{+19}_{-19}$ (13) (12)	−19.860 $^{+0.065}_{-0.066}$ (0.041) (0.043)	1.00 $^{+0.04}_{-0.04}$	−35.30 $^{+0.11}_{-0.10}$	8620 $^{+424}_{-754}$	−0.004	−0.043
WISE 1039 − 1600	0.5 $''$	847 $^{+29}_{-30}$ (21) (22)	3.74 $^{+0.31}_{-0.29}$ (0.24) (0.21)	−0.38 $^{+0.15}_{-0.12}$ (+0.10) (−0.07)	359 $^{+235}_{-235}$ (153) (151)	27 $^{+26}_{-27}$ (21) (17)	−19.803 $^{+0.073}_{-0.072}$ (0.050) (0.049)	1.04 $^{+0.04}_{-0.04}$	−35.06 $^{+0.13}_{-0.13}$	6024 $^{+1816}_{-1537}$	−0.059	+0.064
WISE 1052 − 1942	0.5 $''$	821 $^{+30}_{-31}$ (23) (24)	3.83 $^{+0.30}_{-0.29}$ (0.23) (0.22)	−0.39 $^{+0.15}_{-0.11}$ (+0.10) (−0.07)	−298 $^{+228}_{-226}$ (144) (143)	24 $^{+25}_{-24}$ (19) (16)	−19.772 $^{+0.080}_{-0.077}$ (0.060) (0.052)	1.08 $^{+0.04}_{-0.04}$	−34.92 $^{+0.10}_{-0.10}$	8433 $^{+549}_{-835}$	−0.005	+0.033
2MASS 1114 − 2618	0.5 $''$	726 $^{+60}_{-55}$ (59) (49)	4.52 $^{+0.42}_{-0.42}$ (0.35) (0.38)	−0.40 $^{+0.15}_{-0.10}$ (+0.11) (−0.07)	−130 $^{+262}_{-262}$ (191) (191)	49 $^{+57}_{-49}$ (57) (33)	−18.986 $^{+0.189}_{-0.182}$ (0.179) (0.178)	1.07 $^{+0.05}_{-0.05}$	−33.80 $^{+0.07}_{-0.07}$	2150 $^{+316}_{-264}$	−0.002	−0.001
WISE 1124 − 0421	0.5 $''$	879 $^{+28}_{-29}$ (20) (21)	4.18 $^{+0.29}_{-0.28}$ (0.21) (0.20)	−0.38 $^{+0.14}_{-0.12}$ (+0.08) (−0.07)	566 $^{+198}_{-197}$ (83) (82)	40 $^{+35}_{-40}$ (30) (27)	−19.736 $^{+0.073}_{-0.071}$ (0.050) (0.042)	1.07 $^{+0.04}_{-0.04}$	−34.92 $^{+0.11}_{-0.11}$	8479 $^{+518}_{-906}$	−0.004	+0.040
2MASS 1217 − 0311	0.5 $''$	886 $^{+24}_{-24}$ (14) (13)	3.98 $^{+0.26}_{-0.27}$ (0.17) (0.18)	0.00 $^{+0.16}_{-0.16}$ (0.11) (0.11)	164 $^{+220}_{-221}$ (127) (127)	30 $^{+28}_{-30}$ (22) (20)	−19.437 $^{+0.059}_{-0.059}$ (0.029) (0.028)	1.02 $^{+0.05}_{-0.05}$	−34.22 $^{+0.07}_{-0.06}$	1698 $^{+209}_{-181}$	+0.017	−0.025
WISE 1254 − 0728	0.5 $''$	936 $^{+32}_{-32}$ (24) (25)	3.98 $^{+0.32}_{-0.32}$ (0.24) (0.25)	−0.15 $^{+0.20}_{-0.18}$ (+0.16) (−0.13)	−2 $^{+258}_{-259}$ (184) (187)	28 $^{+29}_{-28}$ (22) (19)	−20.220 $^{+0.072}_{-0.071}$ (0.051) (0.048)	1.09 $^{+0.04}_{-0.04}$	−35.62 $^{+0.14}_{-0.14}$	6486 $^{+1626}_{-1624}$	−0.012	+0.098
WISE 1257 + 4008	0.5 $''$	933 $^{+34}_{-35}$ (27) (29)	4.83 $^{+0.41}_{-0.40}$ (0.37) (0.35)	−0.06 $^{+0.19}_{-0.18}$ (+0.14) (−0.14)	397 $^{+223}_{-224}$ (135) (135)	67 $^{+65}_{-58}$ (63) (45)	−20.067 $^{+0.083}_{-0.080}$ (0.062) (0.055)	1.05 $^{+0.04}_{-0.04}$	−35.05 $^{+0.11}_{-0.11}$	8328 $^{+618}_{-1014}$	−0.004	+0.067
Ross 458C	0.5 $''$	804 $^{+30}_{-29}$ (22) (21)	4.09 $^{+0.31}_{-0.33}$ (0.23) (0.28)	0.23 $^{+0.20}_{-0.23}$ (0.17) (0.20)	276 $^{+217}_{-217}$ (125) (119)	28 $^{+30}_{-28}$ (23) (19)	−19.727 $^{+0.075}_{-0.076}$ (0.054) (0.057)	0.93 $^{+0.04}_{-0.04}$	−34.67 $^{+0.09}_{-0.09}$	8541 $^{+471}_{-747}$	+0.068	−0.135

Table 4 continued

Table 4 (continued)

Object	Slit ($''$)	T_{eff} (K)	$\log g$ (dex)	Z (dex)	v_r (km s $^{-1}$)	$v \sin i$ (km s $^{-1}$)	$\log \Omega$ (dex)	a_N	$\log a_G$ (dex)	ℓ (km s $^{-1}$)	additive $\log \Omega$ systematics ^a	
											J band (dex)	K band (dex)
WISE 1322 – 2340	0.5 $''$	822 $^{+34}_{-37}$ (28) (32)	3.98 $^{+0.34}_{-0.32}$ (0.28) (0.25)	−0.38 $^{+0.15}_{-0.12}$ (+0.11) (−0.08)	132 $^{+281}_{-284}$ (213) (225)	30 $^{+31}_{-30}$ (25) (20)	−19.558 $^{+0.109}_{-0.101}$ (0.083) (0.063)	1.08 $^{+0.05}_{-0.05}$	−33.91 $^{+0.04}_{-0.04}$	825 $^{+8}_{-4}$	−0.198	+0.068
ULAS 1416 + 1348	0.5 $''$	695 $^{+33}_{-32}$ (27) (25)	5.21 $^{+0.26}_{-0.25}$ (0.19) (0.15)	−0.39 $^{+0.14}_{-0.11}$ (+0.09) (−0.07)	−348 $^{+218}_{-218}$ (123) (123)	108 $^{+74}_{-78}$ (74) (74)	−19.555 $^{+0.105}_{-0.107}$ (0.090) (0.097)	1.09 $^{+0.04}_{-0.04}$	−35.36 $^{+0.11}_{-0.10}$	8504 $^{+509}_{-910}$	+0.030	+0.274
WISE 1457 + 5815	0.5 $''$	882 $^{+30}_{-31}$ (23) (24)	4.27 $^{+0.33}_{-0.31}$ (0.26) (0.24)	−0.31 $^{+0.15}_{-0.15}$ (+0.09) (−0.09)	−308 $^{+209}_{-209}$ (109) (106)	44 $^{+40}_{-44}$ (36) (29)	−19.918 $^{+0.078}_{-0.075}$ (0.055) (0.049)	0.97 $^{+0.04}_{-0.04}$	−35.30 $^{+0.13}_{-0.12}$	8274 $^{+659}_{-1029}$	−0.005	+0.086
GJ 570D	0.5 $''$	828 $^{+25}_{-26}$ (16) (16)	3.90 $^{+0.25}_{-0.25}$ (0.16) (0.15)	−0.33 $^{+0.14}_{-0.14}$ (+0.08) (−0.08)	431 $^{+213}_{-212}$ (114) (115)	26 $^{+25}_{-26}$ (18) (17)	−19.012 $^{+0.067}_{-0.066}$ (0.041) (0.037)	1.04 $^{+0.05}_{-0.05}$	−33.79 $^{+0.08}_{-0.08}$	2714 $^{+437}_{-372}$	+0.010	+0.014
PSO J224 + 47	0.8 $''$	930 $^{+27}_{-27}$ (18) (18)	3.62 $^{+0.30}_{-0.29}$ (0.23) (0.22)	0.12 $^{+0.20}_{-0.19}$ (0.16) (0.15)	−426 $^{+242}_{-241}$ (164) (160)	19 $^{+19}_{-19}$ (14) (12)	−20.102 $^{+0.066}_{-0.066}$ (0.036) (0.035)	1.08 $^{+0.04}_{-0.04}$	−35.52 $^{+0.10}_{-0.09}$	5337 $^{+175}_{-354}$	+0.019	+0.084
SDSS 1504 + 1027	0.8 $''$	937 $^{+26}_{-26}$ (17) (17)	3.82 $^{+0.29}_{-0.28}$ (0.21) (0.20)	−0.39 $^{+0.15}_{-0.11}$ (+0.09) (−0.07)	817 $^{+225}_{-226}$ (136) (139)	27 $^{+25}_{-27}$ (20) (17)	−19.972 $^{+0.063}_{-0.063}$ (0.032) (0.033)	0.91 $^{+0.04}_{-0.04}$	−35.28 $^{+0.09}_{-0.08}$	5208 $^{+264}_{-422}$	+0.070	−0.041
2MASS 1553 + 1532	0.5 $''$	885 $^{+27}_{-27}$ (18) (18)	4.10 $^{+0.25}_{-0.25}$ (0.15) (0.15)	−0.30 $^{+0.14}_{-0.14}$ (+0.07) (−0.07)	183 $^{+188}_{-189}$ (59) (59)	40 $^{+34}_{-40}$ (28) (27)	−19.350 $^{+0.066}_{-0.066}$ (0.042) (0.039)	1.01 $^{+0.04}_{-0.04}$	−34.25 $^{+0.10}_{-0.10}$	8263 $^{+650}_{-883}$	+0.014	−0.039
SDSS 1628 + 2308	0.8 $''$	910 $^{+26}_{-26}$ (17) (17)	4.21 $^{+0.28}_{-0.28}$ (0.19) (0.19)	0.05 $^{+0.18}_{-0.22}$ (0.14) (0.12)	−298 $^{+227}_{-229}$ (136) (145)	36 $^{+32}_{-36}$ (26) (24)	−19.781 $^{+0.062}_{-0.062}$ (0.036) (0.036)	1.03 $^{+0.04}_{-0.04}$	−34.97 $^{+0.08}_{-0.08}$	5413 $^{+118}_{-236}$	+0.030	−0.068
WISE 1653 + 4444	0.5 $''$	800 $^{+30}_{-30}$ (22) (22)	4.10 $^{+0.34}_{-0.36}$ (0.28) (0.29)	−0.01 $^{+0.22}_{-0.21}$ (+0.19) (−0.18)	343 $^{+229}_{-230}$ (141) (145)	27 $^{+29}_{-27}$ (23) (18)	−19.950 $^{+0.078}_{-0.078}$ (0.054) (0.057)	1.07 $^{+0.04}_{-0.04}$	−35.22 $^{+0.10}_{-0.10}$	8530 $^{+486}_{-811}$	+0.130	+0.206
WISE 1711 + 3500	0.5 $''$	817 $^{+46}_{-52}$ (41) (46)	3.80 $^{+0.47}_{-0.38}$ (0.43) (0.33)	−0.26 $^{+0.27}_{-0.20}$ (+0.25) (−0.15)	−499 $^{+448}_{-435}$ (403) (386)	27 $^{+30}_{-27}$ (26) (16)	−20.122 $^{+0.141}_{-0.122}$ (0.114) (0.092)	1.18 $^{+0.05}_{-0.05}$	−34.58 $^{+0.05}_{-0.05}$	824 $^{+7}_{-3}$	+0.047	+0.161
	0.8 $''$	821 $^{+26}_{-26}$ (16) (17)	3.61 $^{+0.27}_{-0.26}$ (0.19) (0.18)	−0.42 $^{+0.14}_{-0.08}$ (+0.08) (−0.05)	546 $^{+231}_{-232}$ (146) (147)	21 $^{+21}_{-21}$ (15) (14)	−20.083 $^{+0.085}_{-0.084}$ (0.042) (0.038)	0.98 $^{+0.04}_{-0.04}$	−35.94 $^{+0.10}_{-0.09}$	5306 $^{+198}_{-368}$	−0.008	+0.102
WISE 1741 + 2553	0.8 $''$	719 $^{+26}_{-26}$ (16) (17)	3.91 $^{+0.27}_{-0.28}$ (0.19) (0.20)	−0.04 $^{+0.18}_{-0.17}$ (+0.13) (−0.12)	−118 $^{+219}_{-219}$ (127) (127)	21 $^{+22}_{-21}$ (16) (14)	−19.150 $^{+0.073}_{-0.071}$ (0.054) (0.045)	0.88 $^{+0.04}_{-0.04}$	−34.41 $^{+0.05}_{-0.05}$	5526 $^{+36}_{-76}$	−0.072	−0.210
WISE 1809 + 3838	0.8 $''$	838 $^{+31}_{-31}$ (24) (24)	3.63 $^{+0.31}_{-0.34}$ (0.24) (0.28)	−0.31 $^{+0.19}_{-0.17}$ (+0.15) (−0.12)	−261 $^{+292}_{-296}$ (232) (234)	21 $^{+20}_{-21}$ (14) (13)	−19.997 $^{+0.078}_{-0.079}$ (0.055) (0.053)	1.14 $^{+0.04}_{-0.04}$	−35.33 $^{+0.10}_{-0.10}$	5272 $^{+224}_{-456}$	−0.019	+0.082
WISE 1813 + 2835	0.5 $''$	811 $^{+30}_{-30}$ (22) (22)	4.20 $^{+0.33}_{-0.34}$ (0.27) (0.28)	0.05 $^{+0.22}_{-0.22}$ (0.19) (0.18)	−107 $^{+214}_{-214}$ (117) (115)	35 $^{+34}_{-35}$ (30) (23)	−19.761 $^{+0.079}_{-0.079}$ (0.054) (0.055)	0.92 $^{+0.04}_{-0.04}$	−34.73 $^{+0.09}_{-0.09}$	8526 $^{+480}_{-737}$	−0.004	+0.058
WISE 1852 + 3537	0.5 $''$	899 $^{+27}_{-27}$ (18) (18)	3.97 $^{+0.27}_{-0.27}$ (0.18) (0.19)	−0.21 $^{+0.15}_{-0.15}$ (+0.09) (−0.09)	−175 $^{+210}_{-210}$ (108) (110)	29 $^{+28}_{-29}$ (21) (20)	−19.761 $^{+0.068}_{-0.067}$ (0.037) (0.039)	1.06 $^{+0.04}_{-0.04}$	−34.94 $^{+0.14}_{-0.12}$	6118 $^{+1211}_{-957}$	−0.005	+0.028
WISE 1959 – 3338	0.5 $''$	812 $^{+28}_{-28}$ (19) (19)	3.92 $^{+0.29}_{-0.29}$ (0.21) (0.21)	−0.10 $^{+0.20}_{-0.18}$ (+0.16) (−0.13)	−47 $^{+207}_{-207}$ (102) (105)	24 $^{+25}_{-24}$ (18) (16)	−19.746 $^{+0.073}_{-0.072}$ (0.049) (0.048)	0.98 $^{+0.04}_{-0.04}$	−35.04 $^{+0.11}_{-0.11}$	8097 $^{+748}_{-994}$	+0.048	+0.095
WISE 2000 + 3629	0.5 $''$	810 $^{+27}_{-27}$ (19) (19)	3.67 $^{+0.27}_{-0.27}$ (0.19) (0.18)	−0.36 $^{+0.16}_{-0.14}$ (+0.11) (−0.09)	367 $^{+200}_{-200}$ (88) (89)	21 $^{+21}_{-21}$ (15) (13)	−19.207 $^{+0.068}_{-0.068}$ (0.046) (0.046)	0.95 $^{+0.04}_{-0.04}$	−33.93 $^{+0.10}_{-0.10}$	8254 $^{+634}_{-846}$	+0.035	−0.113
WISE 2157 + 2659	0.8 $''$	860 $^{+26}_{-26}$ (16) (16)	3.79 $^{+0.27}_{-0.27}$ (0.18) (0.19)	−0.28 $^{+0.15}_{-0.15}$ (+0.09) (−0.09)	−176 $^{+219}_{-220}$ (123) (130)	22 $^{+21}_{-22}$ (15) (14)	−19.994 $^{+0.063}_{-0.063}$ (0.034) (0.037)	0.93 $^{+0.04}_{-0.04}$	−35.65 $^{+0.07}_{-0.07}$	5468 $^{+80}_{-170}$	+0.047	+0.100
WISE 2209 – 2734	0.8 $''$	801 $^{+49}_{-46}$ (46) (42)	4.54 $^{+0.32}_{-0.36}$ (0.22) (0.32)	−0.43 $^{+0.14}_{-0.07}$ (+0.08) (−0.04)	142 $^{+235}_{-234}$ (155) (145)	56 $^{+54}_{-52}$ (54) (38)	−19.630 $^{+0.134}_{-0.129}$ (0.121) (0.123)	0.91 $^{+0.04}_{-0.04}$	−35.07 $^{+0.08}_{-0.07}$	5351 $^{+165}_{-292}$	−0.002	+0.054
WISE 2213 + 0911	0.5 $''$	908 $^{+29}_{-30}$ (21) (22)	4.19 $^{+0.28}_{-0.28}$ (0.20) (0.19)	−0.31 $^{+0.14}_{-0.14}$ (+0.07) (−0.08)	−89 $^{+195}_{-195}$ (79) (78)	38 $^{+34}_{-38}$ (28) (25)	−19.957 $^{+0.073}_{-0.073}$ (0.047) (0.047)	1.01 $^{+0.04}_{-0.04}$	−35.36 $^{+0.11}_{-0.11}$	8195 $^{+706}_{-1059}$	−0.002	+0.035
WISE 2226 + 0440	0.5 $''$	829 $^{+26}_{-26}$ (18) (17)	3.78 $^{+0.28}_{-0.28}$ (0.19) (0.21)	−0.26 $^{+0.16}_{-0.16}$ (+0.11) (−0.11)	120 $^{+206}_{-206}$ (101) (103)	25 $^{+24}_{-25}$ (18) (16)	−19.879 $^{+0.071}_{-0.070}$ (0.044) (0.041)	1.05 $^{+0.04}_{-0.04}$	−35.30 $^{+0.11}_{-0.10}$	8024 $^{+788}_{-1008}$	+0.052	+0.085
WISE 2255 – 3118	0.5 $''$	790 $^{+28}_{-27}$ (19) (18)	3.66 $^{+0.32}_{-0.30}$ (0.25) (0.23)	−0.21 $^{+0.20}_{-0.19}$ (+0.16) (−0.14)	921 $^{+224}_{-224}$ (138) (133)	19 $^{+20}_{-19}$ (14) (12)	−19.868 $^{+0.071}_{-0.070}$ (0.047) (0.047)	1.07 $^{+0.04}_{-0.04}$	−35.26 $^{+0.12}_{-0.11}$	7523 $^{+1072}_{-1177}$	−0.013	+0.056
WISE 2319 – 1844	0.5 $''$	782 $^{+39}_{-41}$ (33) (36)	4.46 $^{+0.34}_{-0.33}$ (0.27) (0.27)	−0.37 $^{+0.15}_{-0.13}$ (+0.11) (−0.08)	533 $^{+237}_{-238}$ (155) (161)	39 $^{+39}_{-39}$ (35) (26)	−19.969 $^{+0.117}_{-0.106}$ (0.108) (0.090)	1.01 $^{+0.04}_{-0.04}$	−35.68 $^{+0.13}_{-0.13}$	8258 $^{+667}_{-1066}$	−0.005	+0.189
ULAS 2321 + 1354	0.8 $''$	822 $^{+29}_{-28}$ (21) (20)	4.20 $^{+0.30}_{-0.31}$ (0.22) (0.23)	0.18 $^{+0.20}_{-0.20}$ (0.17) (0.16)	485 $^{+244}_{-244}$ (167) (164)	33 $^{+32}_{-33}$ (26) (22)	−19.770 $^{+0.071}_{-0.071}$ (0.051) (0.049)	0.88 $^{+0.04}_{-0.04}$	−34.95 $^{+0.09}_{-0.09}$	5041 $^{+367}_{-488}$	+0.033	−0.067
WISE 2340 – 0745	0.5 $''$	918 $^{+31}_{-32}$ (23) (24)	4.53 $^{+0.30}_{-0.29}$ (0.22) (0.21)	−0.29 $^{+0.14}_{-0.14}$ (+0.08) (−0.08)	199 $^{+194}_{-194}$ (75) (74)	66 $^{+54}_{-57}$ (51) (44)	−19.711 $^{+0.075}_{-0.072}$ (0.055) (0.049)	1.06 $^{+0.04}_{-0.04}$	−34.73 $^{+0.10}_{-0.10}$	8431 $^{+548}_{-881}$	−0.003	+0.031
WISE 2348 – 1028	0.5 $''$	900 $^{+28}_{-28}$ (19) (20)	4.09 $^{+0.30}_{-0.30}$ (0.23) (0.22)	−0.15 $^{+0.18}_{-0.17}$ (+0.13) (−0.11)	−127 $^{+205}_{-205}$ (100) (101)	31 $^{+30}_{-31}$ (24) (21)	−19.877 $^{+0.070}_{-0.070}$ (0.042) (0.043)	1.02 $^{+0.04}_{-0.04}$	−34.99 $^{+0.12}_{-0.11}$	7297 $^{+1181}_{-1226}$	−0.004	+0.045

NOTE—We report the median and 1σ uncertainties for each fitted parameter with systematic errors incorporated (Section 3.1). The formal 1σ errors of parameters directly obtained from the spectral fitting process are shown in parentheses.

^a The small shifts to be added to our fitted $\log \Omega$ if the objects' observed spectra are flux-calibrated by their J_{MKO} or K_{MKO} photometry rather than H_{MKO} used in this work (see Section 3.1).

Table 5. Starfish-Based Forward-Modeling Analysis: Derived properties of T7–T9 Dwarfs

Object	Slit ($''$)	R (R_{Jup})	M (M_{Jup})	$\log(L_{\text{bol}}/L_{\odot})$ (dex)	Age (Myr)	ϵ_J (%)	$q_{(\lambda\lambda)}$ quantities			
							q_Y (%)	q_I (%)	q_H (%)	q_K (%)
HD 3651B	0.5''	$0.81^{+0.07}_{-0.06}$	$2.33^{+2.27}_{-1.14}$	$-5.569^{+0.026}_{-0.029}$	38^{+76}_{-25}	$2.6^{+0.4}_{-0.3}$	3 ± 4	-9 ± 4	17 ± 8	11 ± 24
WISE 0040 + 0900	0.5''	$0.88^{+0.08}_{-0.08}$	$3.67^{+3.95}_{-1.86}$	$-5.347^{+0.045}_{-0.043}$	50^{+195}_{-34}	$2.6^{+0.3}_{-0.3}$	6 ± 4	-8 ± 3	11 ± 8	27 ± 18
WISE 0049 + 2151	0.5''	$0.65^{+0.06}_{-0.05}$	$0.51^{+0.42}_{-0.19}$	$-5.895^{+0.039}_{-0.039}$	8^{+13}_{-4}	$2.8^{+0.4}_{-0.3}$	3 ± 4	-7 ± 4	23 ± 9	15 ± 26
	0.8''	$0.62^{+0.06}_{-0.05}$	$0.59^{+0.57}_{-0.27}$	$-5.918^{+0.041}_{-0.039}$	12^{+23}_{-7}	$2.6^{+0.3}_{-0.2}$	6 ± 4	-8 ± 3	27 ± 7	24 ± 19
2MASS 0050 – 3322	0.5''	$0.73^{+0.06}_{-0.06}$	$2.45^{+2.04}_{-1.13}$	$-5.397^{+0.039}_{-0.038}$	40^{+105}_{-25}	$1.9^{+0.2}_{-0.1}$	-1 ± 2	-2 ± 1	10 ± 3	6 ± 7
WISE 0123 + 4142	0.8''	$0.79^{+0.08}_{-0.07}$	$3.32^{+3.67}_{-1.72}$	$-5.191^{+0.060}_{-0.058}$	41^{+168}_{-28}	$2.3^{+0.2}_{-0.2}$	3 ± 3	-4 ± 2	11 ± 4	9 ± 12
WISE 0223 – 2932	0.5''	$0.72^{+0.09}_{-0.07}$	$2.95^{+3.43}_{-1.55}$	$-5.718^{+0.054}_{-0.051}$	91^{+318}_{-63}	$2.5^{+0.3}_{-0.3}$	1 ± 4	-7 ± 3	21 ± 8	19 ± 28
WISE 0241 – 3653	0.8''	$0.90^{+0.09}_{-0.08}$	$2.75^{+2.44}_{-1.29}$	$-5.287^{+0.057}_{-0.054}$	26^{+47}_{-17}	$2.1^{+0.2}_{-0.2}$	4 ± 2	-5 ± 2	13 ± 4	3 ± 13
WISE 0245 – 3450 ^a	0.5''	–	–	–	6^{+8}_{-3}	$2.0^{+0.4}_{-0.3}$	6 ± 3	-4 ± 3	10 ± 7	16 ± 17
PSO J043 + 02	0.5''	$0.60^{+0.05}_{-0.05}$	$2.09^{+2.06}_{-1.04}$	$-5.856^{+0.034}_{-0.034}$	92^{+311}_{-62}	$3.1^{+0.4}_{-0.4}$	-1 ± 5	-6 ± 4	26 ± 9	1 ± 31
WISE 0325 + 0831	0.5''	$0.99^{+0.09}_{-0.09}$	$1.04^{+0.81}_{-0.33}$	$-5.265^{+0.047}_{-0.046}$	5^{+7}_{-2}	$2.8^{+0.4}_{-0.3}$	8 ± 4	-6 ± 4	16 ± 9	2 ± 19
2MASS 0415 – 0935	0.5''	$0.67^{+0.06}_{-0.05}$	$2.10^{+1.96}_{-1.02}$	$-5.779^{+0.036}_{-0.033}$	68^{+202}_{-45}	$3.2^{+0.4}_{-0.3}$	-3 ± 6	-7 ± 4	27 ± 9	17 ± 27
WISE 0458 + 6434	0.5''	$0.59^{+0.08}_{-0.06}$	$1.16^{+1.64}_{-0.65}$	$-6.002^{+0.058}_{-0.054}$	44^{+137}_{-32}	$3.7^{+0.5}_{-0.5}$	7 ± 6	-10 ± 5	25 ± 12	-32 ± 68
WISE 0500 – 1223	0.5''	$0.57^{+0.13}_{-0.08}$	$1.76^{+4.65}_{-1.19}$	$-6.070^{+0.058}_{-0.052}$	106^{+549}_{-85}	$3.8^{+0.6}_{-0.5}$	10 ± 7	-10 ± 6	27 ± 12	-3 ± 69
WISE 0521 + 1025	0.8''	$0.96^{+0.08}_{-0.08}$	$0.87^{+0.58}_{-0.23}$	$-5.350^{+0.045}_{-0.043}$	4^{+5}_{-1}	$2.1^{+0.2}_{-0.2}$	9 ± 2	-7 ± 2	11 ± 5	17 ± 11
UGPS 0521 + 3640	0.8''	$0.45^{+0.04}_{-0.04}$	$2.61^{+2.58}_{-1.29}$	$-6.139^{+0.037}_{-0.035}$	470^{+696}_{-343}	$3.6^{+0.3}_{-0.3}$	2 ± 5	-9 ± 4	33 ± 7	-3 ± 22
WISE 0614 + 0951	0.8''	$0.85^{+0.07}_{-0.07}$	$4.75^{+4.30}_{-2.29}$	$-5.242^{+0.042}_{-0.040}$	73^{+207}_{-49}	$2.3^{+0.2}_{-0.2}$	4 ± 3	-6 ± 2	17 ± 5	4 ± 11
WISE 0623 – 0456	0.5''	$0.78^{+0.17}_{-0.13}$	$13.18^{+31.26}_{-9.44}$	$-5.755^{+0.060}_{-0.049}$	738^{+2701}_{-592}	$3.4^{+0.6}_{-0.5}$	7 ± 6	-7 ± 5	20 ± 11	37 ± 39
UGPS 0722 – 0540	0.5''	$0.43^{+0.04}_{-0.03}$	$0.30^{+0.30}_{-0.14}$	$-6.422^{+0.045}_{-0.042}$	19^{+40}_{-12}	$3.7^{+0.4}_{-0.3}$	2 ± 6	-17 ± 6	33 ± 13	18 ± 36
2MASS 0727 + 1710	0.5''	$0.83^{+0.06}_{-0.06}$	$2.40^{+1.91}_{-1.07}$	$-5.381^{+0.031}_{-0.029}$	29^{+46}_{-18}	$1.9^{+0.2}_{-0.2}$	3 ± 3	-4 ± 2	11 ± 4	13 ± 10
2MASS 0729 – 3954	0.5''	$0.80^{+0.14}_{-0.11}$	$8.41^{+12.40}_{-5.19}$	$-5.602^{+0.075}_{-0.069}$	402^{+749}_{-318}	$2.9^{+0.4}_{-0.4}$	7 ± 4	-9 ± 4	13 ± 9	14 ± 37
2MASS 0939 – 2448	0.5''	$0.97^{+0.16}_{-0.16}$	$21.97^{+28.09}_{-12.97}$	$-5.768^{+0.066}_{-0.063}$	1288^{+2492}_{-773}	$3.0^{+0.3}_{-0.3}$	7 ± 3	-9 ± 3	23 ± 7	37 ± 42
ULAS 1029 + 0935	0.5''	$0.74^{+0.06}_{-0.06}$	$0.91^{+0.91}_{-0.43}$	$-5.682^{+0.040}_{-0.038}$	12^{+26}_{-7}	$3.0^{+0.4}_{-0.3}$	6 ± 5	-10 ± 4	21 ± 10	27 ± 21
WISE 1039 – 1600	0.5''	$1.20^{+0.12}_{-0.11}$	$3.20^{+3.58}_{-1.61}$	$-5.157^{+0.050}_{-0.046}$	16^{+37}_{-10}	$2.7^{+0.5}_{-0.4}$	5 ± 4	-6 ± 3	13 ± 8	19 ± 20
WISE 1052 – 1942	0.5''	$0.83^{+0.08}_{-0.07}$	$1.85^{+2.07}_{-0.94}$	$-5.508^{+0.044}_{-0.042}$	24^{+54}_{-16}	$3.1^{+0.4}_{-0.4}$	6 ± 5	-5 ± 4	25 ± 9	40 ± 22
2MASS 1114 – 2618	0.5''	$0.77^{+0.19}_{-0.15}$	$8.41^{+21.51}_{-6.28}$	$-5.800^{+0.062}_{-0.049}$	519^{+1576}_{-444}	$3.5^{+0.3}_{-0.3}$	7 ± 4	-9 ± 3	23 ± 6	24 ± 30
WISE 1124 – 0421	0.5''	$1.02^{+0.11}_{-0.10}$	$6.27^{+6.67}_{-3.15}$	$-5.227^{+0.063}_{-0.058}$	74^{+242}_{-50}	$2.3^{+0.3}_{-0.3}$	6 ± 4	-7 ± 3	6 ± 7	30 ± 18
2MASS 1217 – 0311	0.5''	$0.90^{+0.07}_{-0.06}$	$3.09^{+2.59}_{-1.44}$	$-5.326^{+0.036}_{-0.035}$	36^{+67}_{-23}	$2.5^{+0.2}_{-0.2}$	0 ± 2	-4 ± 2	16 ± 4	4 ± 8
WISE 1254 – 0728	0.5''	$0.81^{+0.09}_{-0.08}$	$2.58^{+2.75}_{-1.33}$	$-5.327^{+0.064}_{-0.060}$	31^{+97}_{-22}	$2.5^{+0.5}_{-0.4}$	0 ± 4	-2 ± 3	12 ± 7	-9 ± 19
WISE 1257 + 4008	0.5''	$0.70^{+0.07}_{-0.06}$	$13.37^{+21.47}_{-8.05}$	$-5.444^{+0.043}_{-0.041}$	709^{+2137}_{-461}	$3.1^{+0.4}_{-0.4}$	-3 ± 6	-7 ± 4	19 ± 9	1 ± 26
Ross 458C	0.5''	$0.68^{+0.06}_{-0.06}$	$2.30^{+2.32}_{-1.20}$	$-5.605^{+0.032}_{-0.036}$	77^{+314}_{-56}	$4.2^{+0.5}_{-0.4}$	0 ± 7	-11 ± 6	32 ± 11	37 ± 18
WISE 1322 – 2340	0.5''	$0.93^{+0.14}_{-0.11}$	$3.26^{+4.72}_{-1.81}$	$-5.424^{+0.066}_{-0.064}$	42^{+135}_{-30}	$6.2^{+0.4}_{-0.4}$	3 ± 4	-6 ± 3	16 ± 7	-4 ± 29

Table 5 continued

Table 5 (continued)

Object	Slit	R	M	$\log(L_{\text{bol}}/L_{\odot})$	Age	ϵ_J	$q(\lambda\lambda)$ quantities			
							q_Y	q_J	q_H	q_K
	('')	(R_{Jup})	(M_{Jup})	(dex)	(Myr)	(%)	(%)	(%)	(%)	(%)
ULAS 1416 + 1348	0.5''	0.67 $^{+0.09}_{-0.08}$	29.63 $^{+19.69}_{-13.25}$	-6.013 $^{+0.052}_{-0.049}$	4544 $^{+3342}_{-2424}$	3.3 $^{+0.4}_{-0.4}$	7 ± 5	-8 ± 4	22 ± 9	1 ± 95
WISE 1457 + 5815	0.5''	1.02 $^{+0.17}_{-0.14}$	7.85 $^{+10.37}_{-4.29}$	-5.229 $^{+0.122}_{-0.105}$	110 $^{+281}_{-79}$	2.3 $^{+0.4}_{-0.3}$	4 ± 4	-6 ± 3	14 ± 7	12 ± 21
GJ 570D	0.5''	0.79 $^{+0.06}_{-0.06}$	2.03 $^{+1.71}_{-0.92}$	-5.544 $^{+0.028}_{-0.031}$	31 $^{+52}_{-20}$	2.0 $^{+0.2}_{-0.2}$	2 ± 3	-4 ± 2	16 ± 4	5 ± 14
PSO J224 + 47	0.8''	0.78 $^{+0.08}_{-0.07}$	1.02 $^{+1.00}_{-0.47}$	-5.378 $^{+0.063}_{-0.059}$	8 $^{+18}_{-5}$	2.4 $^{+0.3}_{-0.3}$	6 ± 3	-6 ± 3	14 ± 6	-11 ± 12
SDSS 1504 + 1027	0.8''	0.97 $^{+0.08}_{-0.07}$	2.47 $^{+2.41}_{-1.20}$	-5.161 $^{+0.040}_{-0.039}$	16 $^{+32}_{-10}$	2.4 $^{+0.3}_{-0.2}$	5 ± 3	-5 ± 2	13 ± 5	10 ± 14
2MASS 1553 + 1532	0.5''	1.21 $^{+0.10}_{-0.09}$	7.56 $^{+6.28}_{-3.42}$	-5.072 $^{+0.032}_{-0.030}$	56 $^{+158}_{-35}$	2.0 $^{+0.2}_{-0.2}$	3 ± 3	-6 ± 3	12 ± 6	16 ± 16
SDSS 1628 + 2308	0.8''	0.74 $^{+0.06}_{-0.05}$	3.57 $^{+3.11}_{-1.68}$	-5.453 $^{+0.031}_{-0.028}$	84 $^{+233}_{-56}$	2.2 $^{+0.2}_{-0.2}$	2 ± 3	-5 ± 2	17 ± 5	6 ± 11
WISE 1653 + 4444	0.5''	0.60 $^{+0.06}_{-0.05}$	1.84 $^{+2.16}_{-1.02}$	-5.837 $^{+0.042}_{-0.039}$	76 $^{+324}_{-56}$	3.6 $^{+0.5}_{-0.4}$	2 ± 6	-8 ± 5	32 ± 10	18 ± 26
WISE 1711 + 3500	0.5''	0.93 $^{+0.18}_{-0.13}$	2.17 $^{+5.07}_{-1.29}$	-5.439 $^{+0.076}_{-0.070}$	22 $^{+122}_{-16}$	10.3 $^{+0.7}_{-0.6}$	6 ± 7	-8 ± 5	22 ± 12	-7 ± 44
	0.8''	0.98 $^{+0.12}_{-0.10}$	1.58 $^{+1.51}_{-0.73}$	-5.395 $^{+0.068}_{-0.064}$	10 $^{+19}_{-6}$	2.2 $^{+0.3}_{-0.2}$	3 ± 3	-5 ± 2	15 ± 6	0 ± 19
WISE 1741 + 2553	0.8''	0.54 $^{+0.05}_{-0.04}$	0.94 $^{+0.85}_{-0.45}$	-6.137 $^{+0.043}_{-0.039}$	49 $^{+91}_{-32}$	2.6 $^{+0.2}_{-0.2}$	3 ± 3	-11 ± 3	32 ± 6	8 ± 20
WISE 1809 + 3838	0.8''	0.83 $^{+0.09}_{-0.08}$	1.19 $^{+1.28}_{-0.57}$	-5.491 $^{+0.051}_{-0.049}$	11 $^{+25}_{-7}$	3.1 $^{+0.4}_{-0.3}$	5 ± 4	-8 ± 4	20 ± 8	28 ± 19
WISE 1813 + 2835	0.5''	0.77 $^{+0.08}_{-0.07}$	3.78 $^{+4.24}_{-2.03}$	-5.609 $^{+0.041}_{-0.039}$	108 $^{+336}_{-79}$	4.1 $^{+0.5}_{-0.4}$	5 ± 7	-14 ± 6	28 ± 11	19 ± 27
WISE 1852 + 3537	0.5''	0.86 $^{+0.08}_{-0.07}$	2.76 $^{+2.44}_{-1.31}$	-5.343 $^{+0.049}_{-0.048}$	33 $^{+61}_{-21}$	2.2 $^{+0.4}_{-0.3}$	1 ± 3	-2 ± 2	14 ± 6	22 ± 13
WISE 1959 - 3338	0.5''	0.68 $^{+0.06}_{-0.06}$	1.54 $^{+1.46}_{-0.75}$	-5.716 $^{+0.043}_{-0.040}$	36 $^{+73}_{-24}$	2.8 $^{+0.4}_{-0.3}$	4 ± 4	-8 ± 4	20 ± 9	11 ± 21
WISE 2000 + 3629	0.5''	0.82 $^{+0.07}_{-0.06}$	1.26 $^{+1.17}_{-0.60}$	-5.558 $^{+0.038}_{-0.036}$	13 $^{+26}_{-8}$	3.1 $^{+0.4}_{-0.3}$	6 ± 5	-10 ± 4	20 ± 9	28 ± 23
WISE 2157 + 2659	0.8''	0.69 $^{+0.06}_{-0.05}$	1.20 $^{+1.07}_{-0.57}$	-5.609 $^{+0.043}_{-0.042}$	18 $^{+34}_{-12}$	2.2 $^{+0.2}_{-0.2}$	3 ± 3	-6 ± 2	20 ± 5	10 ± 15
WISE 2209 - 2734	0.8''	0.91 $^{+0.16}_{-0.13}$	12.19 $^{+18.62}_{-8.09}$	-5.496 $^{+0.065}_{-0.061}$	433 $^{+944}_{-345}$	2.6 $^{+0.3}_{-0.2}$	6 ± 3	-6 ± 2	15 ± 6	23 ± 25
WISE 2213 + 0911	0.5''	0.87 $^{+0.10}_{-0.08}$	4.76 $^{+4.87}_{-2.35}$	-5.312 $^{+0.061}_{-0.058}$	74 $^{+228}_{-49}$	2.1 $^{+0.3}_{-0.2}$	3 ± 4	-6 ± 3	12 ± 6	17 ± 16
WISE 2226 + 0440	0.5''	0.91 $^{+0.14}_{-0.11}$	2.05 $^{+2.06}_{-1.03}$	-5.434 $^{+0.106}_{-0.093}$	20 $^{+39}_{-13}$	2.6 $^{+0.3}_{-0.3}$	-1 ± 4	-6 ± 3	19 ± 8	19 ± 20
WISE 2255 - 3118	0.5''	0.71 $^{+0.08}_{-0.07}$	0.95 $^{+1.04}_{-0.47}$	-5.729 $^{+0.062}_{-0.061}$	15 $^{+35}_{-10}$	3.1 $^{+0.5}_{-0.4}$	1 ± 5	-8 ± 4	24 ± 10	24 ± 23
WISE 2319 - 1844	0.5''	0.53 $^{+0.08}_{-0.06}$	3.25 $^{+4.96}_{-1.95}$	-6.012 $^{+0.052}_{-0.051}$	401 $^{+699}_{-322}$	2.8 $^{+0.4}_{-0.4}$	6 ± 5	-6 ± 4	19 ± 9	-10 ± 47
ULAS 2321 + 1354	0.8''	0.67 $^{+0.06}_{-0.06}$	2.89 $^{+2.79}_{-1.46}$	-5.710 $^{+0.040}_{-0.040}$	110 $^{+311}_{-77}$	3.3 $^{+0.4}_{-0.3}$	3 ± 4	-8 ± 3	21 ± 7	7 ± 17
WISE 2340 - 0745	0.5''	1.26 $^{+0.14}_{-0.13}$	21.96 $^{+24.26}_{-11.25}$	-4.971 $^{+0.064}_{-0.060}$	305 $^{+503}_{-218}$	2.2 $^{+0.3}_{-0.3}$	1 ± 4	-6 ± 3	13 ± 6	18 ± 19
WISE 2348 - 1028	0.5''	0.74 $^{+0.08}_{-0.07}$	2.70 $^{+2.72}_{-1.35}$	-5.477 $^{+0.059}_{-0.056}$	52 $^{+219}_{-35}$	2.7 $^{+0.4}_{-0.3}$	1 ± 4	-5 ± 3	15 ± 7	12 ± 18

NOTE—Radii (R) is derived from the objects' parallaxes and spectroscopically inferred $\log \Omega$. Mass (M) is derived from R and fitted $\log g$. Bolometric luminosity ($\log(L_{\text{bol}}/L_{\odot})$) is derived from integrating the objects' 1.0 – 2.5 μm SpEx spectra and fitted model spectra to shorter and longer wavelengths spanning 0.4 – 50 μm , with spectra scaled by measured parallaxes (Section 3.2). Age is derived from the spectroscopically inferred T_{eff} , $\log g$, Z , and the cloudless Sonora-Bobcat evolutionary models (Section 5.2). The measure of the data-model discrepancy (ϵ_J) is derived from the fitted hyper-parameters a_N and a_G , as well as the objects' J -band peak fluxes (Section 6). The measure of spectral-fitting residuals in $YJHK$ bands, $q(\lambda\lambda)$, is defined in Equation 2 and computed using the objects' observed spectra and their fitted model spectra (Section 6.2).

^a WISE 0245 - 3450 lacks a parallax and thus has no radii, mass, or bolometric luminosity results.

Table 6. Typical Parameter Uncertainties for Our Forward-Modeling Analysis

Method	T_{eff} (K)	$\log g$ (dex)	Z (dex)	v_r (km s ⁻¹)	$v \sin i$ (km s ⁻¹)	$\log \Omega$ (dex)	R (R _{Jup})	M (M _{Jup})
<i>Starfish</i>								
formal	20	0.22	0.102	127	21	0.049	0.06	1.3
adopted	28	0.29	0.154	220	29	0.073	0.08	1.9
<i>Traditional</i>								
formal	3	0.02	0.011	29	20	0.006	0.03	0.2
adopted	3	0.02	0.011	183	20	0.024	0.04	0.3

NOTE—Formal uncertainties are obtained directly from the spectral fitting process and the adopted uncertainties are those with systematic errors incorporated (Section 3.1 and Appendix C). We only show the formal uncertainties if they are different from the adopted ones.

Table 7. Bolometric Luminosities from This Work, [Filippazzo et al. \(2015\)](#), and [Line et al. \(2017\)](#)

Object	SpT	This Work		Literature Values ^a					
		Parallax (mas)	$\log(L_{\text{bol}}/L_{\odot})$ (dex)	Parallax (mas)	Par. Ref.	Filippazzo et al. (2015) $\log(L_{\text{bol}}/L_{\odot})$		Line et al. (2017) $\log(L_{\text{bol}}/L_{\odot})$	
						original (dex)	modified (dex)	original (dex)	modified (dex)
HD 3651B	T7.5	89.79 ± 0.06	$-5.569^{+0.026}_{-0.029}$	90.42 ± 0.32	3	-5.56 ± 0.01	-5.55 ± 0.01	-5.51 ± 0.05	-5.50 ± 0.05
2MASS J00501994 – 3322402	T7	94.60 ± 2.40	$-5.397^{+0.039}_{-0.038}$	94.60 ± 2.40	5	-5.39 ± 0.02	-5.39 ± 0.02	-5.27 ± 0.06	-5.27 ± 0.06
PSO J043.5395 + 02.3995	T8	146.10 ± 1.50	$-5.856^{+0.034}_{-0.034}$	166.00 ± 26.00	7	-5.88 ± 0.14	-5.77 ± 0.14	–	–
2MASS J0415195 – 093506	T8	175.20 ± 1.70	$-5.779^{+0.036}_{-0.033}$	175.20 ± 1.70	5	-5.74 ± 0.01	-5.74 ± 0.01	-5.70 ± 0.04	-5.70 ± 0.04
UGPS J072227.51 – 054031.2	T9	242.80 ± 2.40	$-6.422^{+0.045}_{-0.042}$	242.80 ± 2.40	8	-6.02 ± 0.02	-6.02 ± 0.02	–	–
2MASS J0727182 + 171001	T7	112.50 ± 0.90	$-5.381^{+0.031}_{-0.029}$	112.50 ± 0.90	5	-5.37 ± 0.01	-5.37 ± 0.01	-5.30 ± 0.03	-5.30 ± 0.03
2MASS J07290002 – 3954043	T8 pec	126.30 ± 8.30	$-5.602^{+0.075}_{-0.069}$	126.30 ± 8.30	6	-5.57 ± 0.06	-5.57 ± 0.06	-5.60 ± 0.08	-5.60 ± 0.08
2MASS J09393548 – 2448279	T8	187.30 ± 4.60	$-5.768^{+0.066}_{-0.063}$	187.30 ± 4.60	4	-5.72 ± 0.02	-5.72 ± 0.02	-5.71 ± 0.07	-5.71 ± 0.07
2MASS J11145133 – 2618235	T7.5	179.20 ± 1.40	$-5.800^{+0.062}_{-0.049}$	179.20 ± 1.40	5	-5.76 ± 0.01	-5.76 ± 0.01	-5.77 ± 0.05	-5.77 ± 0.05
2MASS J1217110 – 031113	T7.5	91.70 ± 2.20	$-5.326^{+0.036}_{-0.035}$	90.80 ± 2.20	1	-5.29 ± 0.02	-5.30 ± 0.02	-5.16 ± 0.05	-5.17 ± 0.05
Ross 458C	T8	86.86 ± 0.15	$-5.605^{+0.032}_{-0.036}$	85.54 ± 1.53	6	-5.54 ± 0.02	-5.55 ± 0.02	–	–
ULAS J141623.94 + 134836.3	(sd) T7.5	107.56 ± 0.30	$-6.013^{+0.052}_{-0.049}$	109.70 ± 1.30	5	-5.79 ± 0.01	-5.77 ± 0.01	-6.08 ± 0.08	-6.06 ± 0.08
GJ 570D	T7.5	170.01 ± 0.09	$-5.544^{+0.028}_{-0.031}$	171.22 ± 0.94	3	-5.55 ± 0.01	-5.54 ± 0.01	-5.49 ± 0.05	-5.48 ± 0.05
SDSS J150411.63 + 102718.4	T7	46.10 ± 1.50	$-5.161^{+0.040}_{-0.039}$	46.10 ± 1.50	5	-5.09 ± 0.03	-5.09 ± 0.03	–	–
2MASS J1553022 + 153236	T7	75.10 ± 0.90	$-5.072^{+0.032}_{-0.030}$	75.10 ± 0.90	5	–	–	-5.00 ± 0.08	-5.00 ± 0.08

^a We compute the modified bolometric luminosities by scaling the original literature L_{bol} 's to the more precise parallaxes adopted in this work without modifying the uncertainties provided by the literature.

References—(1) [Tinney et al. \(2003\)](#), (2) [van Leeuwen \(2007\)](#), (3) [van Leeuwen \(2007\)](#), (4) [Burgasser et al. \(2008b\)](#), (5) [Dupuy & Liu \(2012\)](#), (6) [Faherty et al. \(2012\)](#), (7) [Kirkpatrick et al. \(2012\)](#), (8) [Leggett et al. \(2012\)](#)

Table 8. Bolometric Corrections for T7–T9 Dwarfs

Spectral Type	N _{obj}	BC _{J_{MKO}}				BC _{H_{MKO}}				BC _{K_{MKO}}			
		mean	error	σ_{add}	rms	mean	error	σ_{add}	rms	mean	error	σ_{add}	rms
		(mag)	(mag)	(mag)	(mag)	(mag)	(mag)	(mag)	(mag)	(mag)	(mag)	(mag)	(mag)
[T7, T7.5)	18	2.67	0.02	0.09	0.10	2.32	0.02	0.00	0.07	2.35	0.02	0.17	0.17
[T7.5, T8)	10	2.58	0.03	0.07	0.10	2.21	0.03	0.00	0.06	2.17	0.03	0.32	0.26
[T8, T8.5)	14	2.57	0.03	0.15	0.16	2.20	0.03	0.00	0.08	2.21	0.03	0.29	0.29
[T8.5, T9)	3	2.59	0.07	0.23	0.18	2.16	0.05	0.20	0.15	2.17	0.09	0.20	0.18
[T9, T9.5)	2	2.29	0.07	0.02	0.05	2.04	0.08	0.11	0.07	1.69	0.11	0.37	0.17

NOTE—For each spectral type bin and photometric band, we tabulate the weighted average, weighted error, and weighted root mean square (rms) of the bolometric corrections, by excluding resolved or candidate binaries and two objects with peculiar spectra (Appendix B). The σ_{add} column gives the additional uncertainty needed to make the reduced $\chi^2 \approx 1$ for the weighted average, as an estimate of the intrinsic (astrophysical) variations. When using these bolometric corrections, we recommend adopting the larger of the weighted error and σ_{add} for the uncertainty on the correction.

Table 9. Traditional Forward-Modeling Analysis: Fitted and Derived Properties of T7–T9 Dwarfs

Object	Slit ($''$)	Fitted Parameters ^a						Derived Parameters ^b		
		T_{eff} (K)	$\log g$ (dex)	Z (dex)	v_r (km s $^{-1}$)	$v \sin i$ (km s $^{-1}$)	$\log \Omega$ (dex)	R (R_{Jup})	M (M_{Jup})	Age (Myr)
HD 3651B	0.5 $''$	824 $^{+2}_{-3}$	4.00 $^{+0.01}_{-0.12}$	-0.14 $^{+0.02}_{-0.02}$	252 $^{+188}_{-197}$ (23)	28 $^{+17}_{-18}$	-19.572 $^{+0.021}_{-0.018}$ (0.006)	0.79 $^{+0.02}_{-0.02}$	2.47 $^{+0.16}_{-0.54}$	47 $^{+1}_{-17}$
WISE 0040 + 0900	0.5 $''$	926 $^{+1}_{-1}$	3.87 $^{+0.00}_{-0.00}$	-0.23 $^{+0.01}_{-0.01}$	291 $^{+188}_{-202}$ (20)	23 $^{+18}_{-14}$	-19.762 $^{+0.010}_{-0.009}$ (0.002)	0.80 $^{+0.04}_{-0.03}$	1.90 $^{+0.20}_{-0.15}$	20 $^{+0}_{-0}$
WISE 0049 + 2151	0.5 $''$	768 $^{+2}_{-2}$	3.67 $^{+0.02}_{-0.02}$	-0.13 $^{+0.01}_{-0.01}$	-345 $^{+193}_{-184}$ (19)	18 $^{+12}_{-12}$	-19.401 $^{+0.010}_{-0.009}$ (0.005)	0.62 $^{+0.01}_{-0.01}$	0.71 $^{+0.04}_{-0.04}$	16 $^{+1}_{-1}$
	0.8 $''$	760 $^{+2}_{-2}$	3.75 $^{+0.04}_{-0.03}$	-0.02 $^{+0.02}_{-0.02}$	-157 $^{+181}_{-181}$ (29)	19 $^{+13}_{-13}$	-19.402 $^{+0.011}_{-0.011}$ (0.007)	0.61 $^{+0.01}_{-0.01}$	0.86 $^{+0.09}_{-0.07}$	23 $^{+4}_{-2}$
2MASS 0050 – 3322	0.5 $''$	950 $^{+1}_{-1}$	4.23 $^{+0.01}_{-0.02}$	-0.02 $^{+0.01}_{-0.01}$	615 $^{+180}_{-180}$ (18)	35 $^{+25}_{-24}$	-19.600 $^{+0.040}_{-0.040}$ (0.002)	0.72 $^{+0.04}_{-0.04}$	3.56 $^{+0.42}_{-0.37}$	79 $^{+5}_{-6}$
WISE 0123 + 4142	0.8 $''$	1025 $^{+1}_{-1}$	3.93 $^{+0.01}_{-0.01}$	-0.35 $^{+0.01}_{-0.01}$	-97 $^{+182}_{-181}$ (27)	28 $^{+17}_{-19}$	-20.281 $^{+0.024}_{-0.024}$ (0.003)	0.79 $^{+0.06}_{-0.05}$	2.20 $^{+0.37}_{-0.28}$	19 $^{+1}_{-0}$
WISE 0223 – 2932	0.5 $''$	820 $^{+2}_{-3}$	4.12 $^{+0.02}_{-0.02}$	-0.28 $^{+0.02}_{-0.01}$	-476 $^{+200}_{-187}$ (35)	31 $^{+19}_{-21}$	-19.833 $^{+0.049}_{-0.045}$ (0.006)	0.65 $^{+0.04}_{-0.04}$	2.25 $^{+0.35}_{-0.27}$	73 $^{+7}_{-5}$
WISE 0241 – 3653	0.8 $''$	914 $^{+1}_{-1}$	3.94 $^{+0.00}_{-0.00}$	-0.37 $^{+0.01}_{-0.01}$	-204 $^{+181}_{-181}$ (25)	29 $^{+19}_{-20}$	-19.941 $^{+0.028}_{-0.028}$ (0.002)	0.88 $^{+0.06}_{-0.05}$	2.71 $^{+0.36}_{-0.31}$	27 $^{+1}_{-0}$
WISE 0245 – 3450	0.5 $''$	813 $^{+10}_{-8}$	3.78 $^{+0.04}_{-0.17}$	-0.17 $^{+0.03}_{-0.04}$	-129 $^{+190}_{-190}$ (64)	146 $^{+103}_{-100}$	-20.117 $^{+0.045}_{-0.045}$ (0.021)	–	–	21 $^{+4}_{-9}$
PSO J043 + 02	0.5 $''$	815 $^{+1}_{-2}$	4.34 $^{+0.02}_{-0.01}$	-0.02 $^{+0.01}_{-0.01}$	64 $^{+180}_{-180}$ (15)	32 $^{+27}_{-20}$	-19.438 $^{+0.011}_{-0.009}$ (0.004)	0.56 $^{+0.01}_{-0.01}$	2.81 $^{+0.14}_{-0.11}$	222 $^{+32}_{-18}$
WISE 0325 + 0831	0.5 $''$	932 $^{+2}_{-2}$	3.82 $^{+0.00}_{-0.00}$	-0.14 $^{+0.01}_{-0.01}$	-498 $^{+198}_{-185}$ (26)	24 $^{+17}_{-15}$	-19.624 $^{+0.036}_{-0.033}$ (0.004)	0.85 $^{+0.05}_{-0.04}$	1.93 $^{+0.24}_{-0.20}$	17 $^{+0}_{-0}$
2MASS 0415 – 0935	0.5 $''$	824 $^{+1}_{-1}$	4.26 $^{+0.00}_{-0.01}$	0.03 $^{+0.00}_{-0.00}$	66 $^{+179}_{-179}$ (8)	29 $^{+24}_{-20}$	-19.227 $^{+0.012}_{-0.012}$ (0.002)	0.60 $^{+0.01}_{-0.01}$	2.64 $^{+0.10}_{-0.11}$	133 $^{+2}_{-4}$
WISE 0458 + 6434	0.5 $''$	584 $^{+147}_{-17}$	5.46 $^{+0.03}_{-1.74}$	-0.11 $^{+0.03}_{-0.37}$	769 $^{+437}_{-309}$ (514)	55 $^{+243}_{-43}$	-19.047 $^{+0.109}_{-0.587}$ (0.088)	1.18 $^{+0.17}_{-0.58}$	165.86 $^{+58.38}_{-165.08}$	23 $^{+7}_{-5}$
WISE 0500 – 1223	0.5 $''$	640 $^{+110}_{-24}$	5.46 $^{+0.04}_{-1.47}$	-0.15 $^{+0.06}_{-0.35}$	-211 $^{+314}_{-303}$ (282)	46 $^{+201}_{-33}$	-19.604 $^{+0.136}_{-0.386}$ (0.097)	0.80 $^{+0.14}_{-0.29}$	78.00 $^{+32.51}_{-76.94}$	62 $^{+25}_{-17}$
WISE 0521 + 1025	0.8 $''$	873 $^{+7}_{-2}$	3.61 $^{+0.01}_{-0.11}$	-0.14 $^{+0.01}_{-0.04}$	124 $^{+182}_{-182}$ (20)	19 $^{+13}_{-13}$	-19.072 $^{+0.024}_{-0.024}$ (0.004)	0.89 $^{+0.04}_{-0.04}$	1.27 $^{+0.15}_{-0.25}$	9 $^{+0}_{-3}$
UGPS 0521 + 3640	0.8 $''$	777 $^{+3}_{-2}$	4.50 $^{+0.01}_{-0.00}$	0.24 $^{+0.01}_{-0.01}$	212 $^{+184}_{-187}$ (31)	38 $^{+28}_{-28}$	-19.777 $^{+0.019}_{-0.018}$ (0.006)	0.46 $^{+0.01}_{-0.01}$	2.69 $^{+0.15}_{-0.13}$	434 $^{+8}_{-6}$
WISE 0614 + 0951	0.8 $''$	966 $^{+1}_{-1}$	4.01 $^{+0.01}_{-0.01}$	-0.06 $^{+0.01}_{-0.01}$	647 $^{+180}_{-180}$ (15)	29 $^{+21}_{-20}$	-19.920 $^{+0.024}_{-0.024}$ (0.002)	0.83 $^{+0.04}_{-0.04}$	2.90 $^{+0.28}_{-0.25}$	32 $^{+1}_{-1}$
WISE 0623 – 0456	0.5 $''$	827 $^{+13}_{-13}$	4.10 $^{+0.12}_{-0.09}$	-0.31 $^{+0.06}_{-0.04}$	155 $^{+216}_{-220}$ (116)	28 $^{+18}_{-19}$	-19.850 $^{+0.051}_{-0.041}$ (0.033)	0.59 $^{+0.04}_{-0.03}$	1.80 $^{+0.66}_{-0.38}$	64 $^{+27}_{-17}$
UGPS 0722 – 0540	0.5 $''$	709 $^{+1}_{-1}$	3.43 $^{+0.02}_{-0.01}$	-0.04 $^{+0.01}_{-0.01}$	-194 $^{+180}_{-179}$ (15)	10 $^{+7}_{-7}$	-19.333 $^{+0.009}_{-0.009}$ (0.003)	0.38 $^{+0.01}_{-0.01}$	0.16 $^{+0.01}_{-0.01}$	9 $^{+1}_{-0}$
2MASS 0727 + 1710	0.5 $''$	911 $^{+1}_{-1}$	4.12 $^{+0.01}_{-0.01}$	-0.11 $^{+0.00}_{-0.00}$	5 $^{+179}_{-179}$ (9)	32 $^{+23}_{-22}$	-19.362 $^{+0.012}_{-0.012}$ (0.002)	0.80 $^{+0.01}_{-0.01}$	3.40 $^{+0.14}_{-0.13}$	57 $^{+2}_{-2}$
2MASS 0729 – 3954	0.5 $''$	837 $^{+5}_{-5}$	4.15 $^{+0.04}_{-0.04}$	-0.45 $^{+0.01}_{-0.01}$	320 $^{+182}_{-183}$ (32)	32 $^{+22}_{-22}$	-19.358 $^{+0.041}_{-0.041}$ (0.011)	0.72 $^{+0.06}_{-0.05}$	2.92 $^{+0.62}_{-0.51}$	76 $^{+13}_{-12}$
2MASS 0939 – 2448	0.5 $''$	667 $^{+0}_{-0}$	5.16 $^{+0.00}_{-0.00}$	-0.32 $^{+0.00}_{-0.00}$	-80 $^{+182}_{-182}$ (29)	82 $^{+92}_{-57}$	-18.799 $^{+0.039}_{-0.046}$ (0.002)	0.92 $^{+0.05}_{-0.05}$	49.15 $^{+5.44}_{-6.95}$	6551 $^{+43}_{-65}$
ULAS 1029 + 0935	0.5 $''$	818 $^{+3}_{-5}$	3.70 $^{+0.02}_{-0.02}$	0.08 $^{+0.02}_{-0.02}$	1 $^{+182}_{-182}$ (31)	21 $^{+10}_{-15}$	-19.923 $^{+0.014}_{-0.010}$ (0.012)	0.69 $^{+0.03}_{-0.02}$	0.96 $^{+0.09}_{-0.06}$	16 $^{+1}_{-1}$
WISE 1039 – 1600	0.5 $''$	860 $^{+6}_{-6}$	3.84 $^{+0.05}_{-0.14}$	-0.24 $^{+0.03}_{-0.04}$	381 $^{+190}_{-190}$ (64)	28 $^{+19}_{-19}$	-19.836 $^{+0.021}_{-0.021}$ (0.013)	1.15 $^{+0.06}_{-0.05}$	3.67 $^{+0.66}_{-1.05}$	22 $^{+5}_{-10}$
WISE 1052 – 1942	0.5 $''$	883 $^{+1}_{-2}$	3.83 $^{+0.01}_{-0.00}$	-0.15 $^{+0.01}_{-0.01}$	-303 $^{+205}_{-189}$ (28)	25 $^{+17}_{-17}$	-19.887 $^{+0.031}_{-0.025}$ (0.003)	0.73 $^{+0.04}_{-0.03}$	1.43 $^{+0.17}_{-0.12}$	20 $^{+0}_{-0}$
2MASS 1114 – 2618	0.5 $''$	809 $^{+2}_{-2}$	4.06 $^{+0.02}_{-0.02}$	-0.45 $^{+0.01}_{-0.01}$	-292 $^{+180}_{-180}$ (23)	27 $^{+18}_{-18}$	-19.218 $^{+0.021}_{-0.021}$ (0.005)	0.59 $^{+0.02}_{-0.01}$	1.62 $^{+0.10}_{-0.10}$	59 $^{+4}_{-4}$
WISE 1124 – 0421	0.5 $''$	921 $^{+1}_{-2}$	3.88 $^{+0.01}_{-0.00}$	-0.26 $^{+0.01}_{-0.01}$	545 $^{+185}_{-199}$ (22)	25 $^{+20}_{-16}$	-19.820 $^{+0.027}_{-0.025}$ (0.004)	0.93 $^{+0.07}_{-0.06}$	2.64 $^{+0.42}_{-0.32}$	22 $^{+0}_{-0}$
2MASS 1217 – 0311	0.5 $''$	908 $^{+2}_{-2}$	4.00 $^{+0.02}_{-0.01}$	0.02 $^{+0.01}_{-0.01}$	77 $^{+181}_{-181}$ (26)	30 $^{+21}_{-21}$	-19.483 $^{+0.013}_{-0.013}$ (0.004)	0.85 $^{+0.02}_{-0.02}$	2.95 $^{+0.24}_{-0.20}$	37 $^{+4}_{-1}$
WISE 1254 – 0728	0.5 $''$	938 $^{+9}_{-9}$	4.27 $^{+0.08}_{-0.25}$	-0.20 $^{+0.04}_{-0.06}$	219 $^{+199}_{-198}$ (85)	36 $^{+26}_{-25}$	-20.234 $^{+0.021}_{-0.020}$ (0.017)	0.80 $^{+0.06}_{-0.05}$	4.49 $^{+1.46}_{-1.81}$	93 $^{+105}_{-58}$
WISE 1257 + 4008	0.5 $''$	946 $^{+5}_{-6}$	4.67 $^{+0.07}_{-0.06}$	-0.04 $^{+0.02}_{-0.02}$	587 $^{+185}_{-185}$ (48)	58 $^{+40}_{-39}$	-20.104 $^{+0.026}_{-0.026}$ (0.010)	0.67 $^{+0.03}_{-0.03}$	8.56 $^{+1.65}_{-1.22}$	428 $^{+132}_{-78}$
Ross 458C	0.5 $''$	836 $^{+3}_{-3}$	4.09 $^{+0.02}_{-0.01}$	0.50 $^{+0.00}_{-0.00}$	168 $^{+182}_{-183}$ (24)	30 $^{+17}_{-21}$	-19.805 $^{+0.021}_{-0.018}$ (0.006)	0.62 $^{+0.02}_{-0.01}$	1.90 $^{+0.12}_{-0.10}$	72 $^{+4}_{-4}$

Table 9 continued

Table 9 (continued)

Object	Slit ($''$)	Fitted Parameters ^a						Derived Parameters ^b		
		T_{eff} (K)	$\log g$ (dex)	Z (dex)	v_r (km s $^{-1}$)	$v \sin i$ (km s $^{-1}$)	$\log \Omega$ (dex)	R (R_{Jup})	M (M_{Jup})	Age (Myr)
WISE 1322 – 2340	0.5 $''$	826 $^{+6}_{-6}$	4.02 $^{+0.09}_{-0.07}$	–0.40 $^{+0.02}_{-0.02}$	104 $^{+186}_{-187}$ (49)	33 $^{+22}_{-22}$	–19.567 $^{+0.064}_{-0.059}$ (0.016)	0.92 $^{+0.09}_{-0.08}$	3.61 $^{+1.14}_{-0.78}$	49 $^{+21}_{-12}$
ULAS 1416 + 1348	0.5 $''$	612 $^{+1}_{-1}$	5.50 $^{+0.00}_{-0.00}$	–0.39 $^{+0.00}_{-0.00}$	–598 $^{+183}_{-183}$ (38)	176 $^{+130}_{-123}$	–19.190 $^{+0.013}_{-0.013}$ (0.006)	1.02 $^{+0.02}_{-0.02}$	131.62 $^{+4.36}_{-4.36}$	–
WISE 1457 + 5815	0.5 $''$	908 $^{+4}_{-7}$	4.07 $^{+0.12}_{-0.04}$	–0.30 $^{+0.04}_{-0.02}$	–276 $^{+194}_{-188}$ (52)	36 $^{+21}_{-25}$	–19.978 $^{+0.029}_{-0.026}$ (0.013)	0.95 $^{+0.15}_{-0.11}$	4.39 $^{+2.11}_{-1.10}$	45 $^{+20}_{-7}$
GJ 570D	0.5 $''$	825 $^{+1}_{-1}$	4.15 $^{+0.02}_{-0.01}$	–0.27 $^{+0.01}_{-0.01}$	118 $^{+180}_{-180}$ (21)	35 $^{+23}_{-24}$	–19.010 $^{+0.020}_{-0.020}$ (0.004)	0.79 $^{+0.02}_{-0.02}$	3.62 $^{+0.21}_{-0.19}$	82 $^{+5}_{-4}$
PSO J224 + 47	0.8 $''$	921 $^{+4}_{-3}$	3.67 $^{+0.32}_{-0.01}$	0.18 $^{+0.05}_{-0.02}$	–360 $^{+219}_{-198}$ (99)	24 $^{+11}_{-16}$	–20.090 $^{+0.033}_{-0.029}$ (0.008)	0.79 $^{+0.07}_{-0.05}$	1.23 $^{+1.12}_{-0.19}$	10 $^{+23}_{-0}$
SDSS 1504 + 1027	0.8 $''$	934 $^{+3}_{-4}$	3.92 $^{+0.01}_{-0.01}$	–0.33 $^{+0.01}_{-0.01}$	874 $^{+193}_{-240}$ (29)	29 $^{+19}_{-19}$	–19.966 $^{+0.027}_{-0.022}$ (0.007)	0.98 $^{+0.05}_{-0.04}$	3.17 $^{+0.36}_{-0.26}$	23 $^{+1}_{-1}$
2MASS 1553 + 1532	0.5 $''$	909 $^{+2}_{-8}$	4.12 $^{+0.17}_{-0.03}$	–0.20 $^{+0.05}_{-0.01}$	129 $^{+181}_{-181}$ (30)	41 $^{+30}_{-28}$	–19.406 $^{+0.016}_{-0.015}$ (0.016)	1.14 $^{+0.02}_{-0.02}$	6.67 $^{+3.76}_{-0.46}$	52 $^{+65}_{-4}$
SDSS 1628 + 2308	0.8 $''$	914 $^{+2}_{-2}$	4.26 $^{+0.01}_{-0.01}$	0.11 $^{+0.01}_{-0.01}$	–272 $^{+181}_{-180}$ (26)	37 $^{+26}_{-25}$	–19.794 $^{+0.013}_{-0.013}$ (0.005)	0.73 $^{+0.01}_{-0.01}$	3.92 $^{+0.16}_{-0.16}$	108 $^{+9}_{-5}$
WISE 1653 + 4444	0.5 $''$	834 $^{+5}_{-5}$	4.24 $^{+0.03}_{-0.05}$	0.09 $^{+0.02}_{-0.03}$	193 $^{+184}_{-184}$ (44)	32 $^{+21}_{-21}$	–20.040 $^{+0.023}_{-0.023}$ (0.011)	0.54 $^{+0.02}_{-0.02}$	2.05 $^{+0.24}_{-0.24}$	118 $^{+20}_{-21}$
WISE 1711 + 3500	0.5 $''$	807 $^{+9}_{-9}$	3.90 $^{+0.12}_{-0.05}$	–0.30 $^{+0.02}_{-0.03}$	–358 $^{+223}_{-202}$ (88)	26 $^{+21}_{-16}$	–20.097 $^{+0.076}_{-0.063}$ (0.027)	0.96 $^{+0.12}_{-0.09}$	3.10 $^{+1.05}_{-0.66}$	34 $^{+18}_{-6}$
	0.8 $''$	812 $^{+5}_{-5}$	3.74 $^{+0.07}_{-0.09}$	–0.37 $^{+0.04}_{-0.03}$	573 $^{+195}_{-233}$ (46)	26 $^{+16}_{-18}$	–20.062 $^{+0.073}_{-0.060}$ (0.015)	1.00 $^{+0.12}_{-0.09}$	2.26 $^{+0.82}_{-0.52}$	18 $^{+7}_{-5}$
WISE 1741 + 2553	0.8 $''$	748 $^{+1}_{-1}$	4.00 $^{+0.00}_{-0.00}$	–0.00 $^{+0.00}_{-0.00}$	–267 $^{+179}_{-179}$ (10)	21 $^{+16}_{-14}$	–19.234 $^{+0.016}_{-0.016}$ (0.003)	0.49 $^{+0.01}_{-0.01}$	0.95 $^{+0.04}_{-0.04}$	62 $^{+1}_{-1}$
WISE 1809 + 3838	0.8 $''$	856 $^{+5}_{-5}$	3.71 $^{+0.10}_{-0.11}$	–0.10 $^{+0.03}_{-0.04}$	–336 $^{+190}_{-190}$ (61)	20 $^{+14}_{-14}$	–20.033 $^{+0.027}_{-0.027}$ (0.011)	0.79 $^{+0.04}_{-0.04}$	1.30 $^{+0.38}_{-0.31}$	14 $^{+7}_{-5}$
WISE 1813 + 2835	0.5 $''$	838 $^{+3}_{-3}$	3.95 $^{+0.03}_{-0.03}$	0.14 $^{+0.01}_{-0.01}$	–66 $^{+181}_{-181}$ (25)	26 $^{+18}_{-17}$	–19.826 $^{+0.025}_{-0.025}$ (0.006)	0.72 $^{+0.03}_{-0.03}$	1.85 $^{+0.19}_{-0.17}$	39 $^{+4}_{-4}$
WISE 1852 + 3537	0.5 $''$	923 $^{+2}_{-1}$	4.11 $^{+0.02}_{-0.02}$	–0.00 $^{+0.00}_{-0.00}$	–157 $^{+180}_{-180}$ (15)	34 $^{+23}_{-23}$	–19.804 $^{+0.024}_{-0.024}$ (0.003)	0.82 $^{+0.04}_{-0.04}$	3.47 $^{+0.41}_{-0.36}$	54 $^{+4}_{-3}$
WISE 1959 – 3338	0.5 $''$	832 $^{+3}_{-3}$	4.00 $^{+0.01}_{-0.00}$	–0.09 $^{+0.01}_{-0.01}$	99 $^{+183}_{-183}$ (32)	28 $^{+16}_{-19}$	–19.793 $^{+0.023}_{-0.021}$ (0.007)	0.64 $^{+0.03}_{-0.02}$	1.68 $^{+0.15}_{-0.14}$	47 $^{+2}_{-1}$
WISE 2000 + 3629	0.5 $''$	843 $^{+2}_{-2}$	3.83 $^{+0.00}_{-0.00}$	–0.17 $^{+0.00}_{-0.00}$	317 $^{+180}_{-180}$ (17)	23 $^{+16}_{-16}$	–19.283 $^{+0.006}_{-0.006}$ (0.004)	0.75 $^{+0.02}_{-0.02}$	1.55 $^{+0.07}_{-0.07}$	23 $^{+0}_{-0}$
WISE 2157 + 2659	0.8 $''$	867 $^{+2}_{-2}$	4.09 $^{+0.01}_{-0.01}$	–0.19 $^{+0.01}_{-0.01}$	–228 $^{+206}_{-191}$ (29)	34 $^{+14}_{-23}$	–20.017 $^{+0.026}_{-0.018}$ (0.006)	0.68 $^{+0.04}_{-0.03}$	2.27 $^{+0.31}_{-0.19}$	57 $^{+2}_{-2}$
WISE 2209 – 2734	0.8 $''$	763 $^{+4}_{-11}$	5.50 $^{+0.00}_{-0.00}$	–0.10 $^{+0.01}_{-0.01}$	359 $^{+185}_{-192}$ (22)	104 $^{+119}_{-69}$	–19.506 $^{+0.040}_{-0.032}$ (0.038)	1.06 $^{+0.08}_{-0.07}$	141.68 $^{+22.52}_{-17.26}$	–
WISE 2213 + 0911	0.5 $''$	934 $^{+3}_{-3}$	4.32 $^{+0.01}_{-0.01}$	–0.14 $^{+0.01}_{-0.01}$	–44 $^{+180}_{-180}$ (29)	40 $^{+29}_{-26}$	–20.016 $^{+0.031}_{-0.026}$ (0.005)	0.82 $^{+0.07}_{-0.05}$	5.58 $^{+1.07}_{-0.73}$	140 $^{+10}_{-12}$
WISE 2226 + 0440	0.5 $''$	848 $^{+2}_{-4}$	4.04 $^{+0.04}_{-0.03}$	–0.04 $^{+0.01}_{-0.02}$	36 $^{+181}_{-181}$ (25)	30 $^{+21}_{-19}$	–19.926 $^{+0.045}_{-0.031}$ (0.008)	0.88 $^{+0.19}_{-0.10}$	3.37 $^{+1.67}_{-0.73}$	50 $^{+5}_{-4}$
WISE 2255 – 3118	0.5 $''$	807 $^{+3}_{-3}$	3.73 $^{+0.03}_{-0.03}$	0.00 $^{+0.01}_{-0.01}$	865 $^{+183}_{-182}$ (37)	20 $^{+13}_{-13}$	–19.911 $^{+0.014}_{-0.014}$ (0.008)	0.68 $^{+0.04}_{-0.04}$	1.00 $^{+0.15}_{-0.13}$	19 $^{+2}_{-2}$
WISE 2319 – 1844	0.5 $''$	805 $^{+8}_{-8}$	4.16 $^{+0.07}_{-0.06}$	–0.49 $^{+0.02}_{-0.01}$	676 $^{+195}_{-211}$ (66)	28 $^{+16}_{-19}$	–20.038 $^{+0.033}_{-0.031}$ (0.023)	0.49 $^{+0.03}_{-0.02}$	1.36 $^{+0.32}_{-0.25}$	87 $^{+28}_{-20}$
ULAS 2321 + 1354	0.8 $''$	829 $^{+2}_{-3}$	4.11 $^{+0.02}_{-0.01}$	0.19 $^{+0.01}_{-0.01}$	462 $^{+186}_{-198}$ (29)	31 $^{+19}_{-21}$	–19.787 $^{+0.015}_{-0.013}$ (0.006)	0.66 $^{+0.02}_{-0.02}$	2.26 $^{+0.21}_{-0.17}$	74 $^{+6}_{-4}$
WISE 2340 – 0745	0.5 $''$	953 $^{+1}_{-1}$	4.41 $^{+0.02}_{-0.02}$	–0.19 $^{+0.01}_{-0.01}$	209 $^{+180}_{-180}$ (18)	54 $^{+39}_{-37}$	–19.783 $^{+0.012}_{-0.012}$ (0.003)	1.16 $^{+0.08}_{-0.07}$	13.97 $^{+2.13}_{-1.76}$	280 $^{+23}_{-23}$
WISE 2348 – 1028	0.5 $''$	907 $^{+2}_{-3}$	4.15 $^{+0.04}_{-0.03}$	–0.03 $^{+0.01}_{-0.01}$	–32 $^{+181}_{-181}$ (31)	36 $^{+19}_{-24}$	–19.895 $^{+0.031}_{-0.026}$ (0.006)	0.72 $^{+0.06}_{-0.05}$	2.96 $^{+0.59}_{-0.40}$	64 $^{+10}_{-7}$

^a We report the median and 1σ errors of each parameter with the systematic errors in v_r and $\log \Omega$ incorporated (Section 3.1). The formal 1σ errors of v_r and $\log \Omega$ directly from the spectral fitting process are shown in parentheses.

^b Parameters are derived in the same approach as those in Table 5. WISE 0245 – 3450 lacks a parallax and thus has no radii or mass results. Ages > 12 Gyr are shown as “–”.